Doctorate Dissertation
博士論文

Effect of the electronic entropy on structural change and ablation of metals by an ultrashort laser pulse
(超短パルスレーザが照射された金属の構造変化とアブレーションに対する電子エントロピーの効果)

A Dissertation Submitted for Degree of Doctor of Philosophy
December 2018
平成 30 年 12 月 博士（理学）申請

Department of Physics, Graduate School of Science,
The University of Tokyo
東京大学大学院理学系研究科物理学専攻

Yuta Tanaka
田中 悠太

ABSTRACT

Irradiation of a solid surface with an ultrashort laser pulse creates a highly excited state, where a high-energy electron system ($\sim$ eV) coexists with a low-energy lattice system. In this nonequilibrium state, some specific phenomena have been reported such as the emission of excessively high-energy atoms/ions and less than nm order ablation. These phenomena are called a non-thermal ablation and have been particularly focused on from not only fundamental physics but also applied physics since the understanding of it directly leads to the development of the higher precision processing technique. Despite intensive investigation inspired by its interest and importance, its physical mechanism is an open question, and there is discrepancy between experiments and previous theoretical simulations.

Purposes of our study are following two. The first one is bridging this discrepancy by elucidating the physical mechanism of the non-thermal ablation of metals. The other is extending calculation models and developing codes to simulate the irradiated metal with an ultrashort pulse laser.

Throughout our study, we use the well-known two-temperature model (TTM) to describe irradiated metals with an ultrashort laser pulse. Our finite-temperature density functional theory (FTDFT) calculations show that the electronic entropy effect leads to the instability of condensed copper (Cu) at high electronic temperature. Based on the result, we propose the electronic entropy-driven (EED) mechanism to describe the non-thermal ablation of metals. Subsequently, to investigate the physical mechanism of the non-thermal ablation and the validity of the EED mechanism, we extend simulation methods and develop calculation codes of the continuum model (CM) simulation and the TTM molecular dynamics (TTM-MD) simulation. Our simulations reproduce experimental results, such as the fluence dependence of the ablation depth and the emission of the high-energy atoms. These results strongly support that the origin of the driving force of the high-energy atom emission is attributed to the electronic entropy effect and the validity of the EED mechanism. In addition, we construct a simple calculation model for estimating the ablation threshold fluence based on our CM and TTM-MD simulation results to find reasonable agreement for several materials (Cr, W, Mo, Ni, Pt, Al, Ag, Cu, and Au).

We are sure that our findings include fundamentally important knowledge not only for the ablation issue but also for the warm dense matter physics and the ultrafast physics, and provide new and essential insight into these interdisciplinary fields. Moreover, our extended calculation models and developed codes will continue to promote the further understanding these fields.

ACKNOWLEDGEMENTS

First of all, I would like to thank my supervisor Prof. Shinji Tsuneyuki for his continuous and patient support to accomplish our study. I am also deeply grateful for his support for my attending conference. I express my great appreciation to Assistant Prof. Ryosuke Akashi for his guidance. From his conversations and discussions, I could learn what a scientific researcher should be. I also appreciate my assistant supervisor Prof. Hiroshi Okamoto, for fruitful discussions and useful advices.

A comfortably managed environment of laboratory was also essential for performing my researches for this five years. I owe it to secretaries of our laboratory, Ms. Emi Shimoshikiryo and Ms. Hiromi Okuzawa. I owe a thank to Mr. Naoto Tsujimoto for his useful discussions and stimulations. I also thank the members in Tsuneyuki Research Group for sharing precious time. I firmly believe that it would be hard to complete my research without their help.

Throughout my research life in the University of Tokyo, I was supported by the Innovative Center for Coherent Photon Technology (ICCPT), the Materials Education program for the future leaders in Research, Industry, and Technology (MERIT), and the Professional development Consortium for Computational Materials Scientists (PCoMS). I have been able to experience a wonderful research life owing to their supports.

I acknowledge Profs. Kenichi Ishikawa, Takeo Kato, Osamu Sugino, Atsushi Fujimori, and Junji Yumoto for their careful reading of the thesis and suggestive comments about the study.

Finally, I express my deep sense of gratitude and appreciation to my family, Toku Terada, Teruko Tanaka, Saori Nishihira, and Riko Tanaka, especially to my parents, Shin Tanaka and Katsue Tanaka.

CONTENTS

1. Introduction **5**
1.1 Physical phenomena caused by irradiation with an ultrashort pulse laser . 5
1.2 Laser ablation 7
1.2.1 Spallation and phase explosion 7
1.2.2 Non-thermal ablation 8
1.3 Purposes of this study 10
1.4 Outline of this thesis 10

2. Finite-Temperature Density Functional Theory (FTDFT) Calculation and Electronic-Entropy Driven (EED) Mechanism **11**
2.1 Density functional theory (DFT) 11
2.2 Finite-temperature DFT (FTDFT) 13
2.3 Methods and results 14
2.4 Summary 17

3. Continuum Model (CM) Simulation **19**
3.1 Basic idea 19
3.2 Parameters 21
3.3 Ablation criteria 24
3.4 Results 25
3.5 Summary 28

4. Two-Temperature Model Molecular Dynamics (TTM-MD) Simulation **29**
4.1 TTM-MD model 29
4.1.1 Simulation model 29
4.1.2 Law of conservation of energy 33
4.1.3 Computational detail 36
4.2 Electronic-temperature-dependent interatomic potential (T_e-dependent IAP) 41
4.2.1 Basic idea 42

4.2.2 Strategy to make the T_e-dependent IAP 48
4.2.3 Validity of the T_e-dependent IAP 52
4.3 Test calculation: energy conservation 59
4.4 Results 62
4.4.1 Ablation near the ablation threshold: emission of atoms 62
4.4.2 Ablation a little higher than the ablation threshold: spallation . . 66
4.4.3 Ablation a little higher than the ablation threshold: phase explosion 73
4.4.4 Ablation depth 75
4.4.5 Pulse-width dependence 77
4.5 Summary 77

5. Material Dependence of Ablation Threshold 79
5.1 Methods and assumptions 79
5.2 Results 82
5.2.1 Ablation threshold temperature: T_e^{thr} 82
5.2.2 Ablation threshold fluence: J_{thr} 84
5.3 Summary 84

6. Concluding Remarks 87
6.1 Summary of this thesis 87
6.2 Future issues 88

APPENDIX A Parameter Dependence of Calculation Results 91

APPENDIX B Pulse Number Dependence of the Reflectivity 93

1. Introduction

Irradiation of a solid surface with an ultrashort laser pulse creates a highly excited state, where a high-energy electron system ($\sim$ eV) coexists with a low-energy lattice system. In this nonequilibrium state, some specific phenomena have been reported such as the emission of excessively high-energy atoms/ions from a laser-irradiated surface. This phenomenon has been particularly focused on from not only fundamental physics but also applied physics since the understanding of it directly leads to the development of the higher-precision processing technique. Despite intensive investigation inspired by its interest and importance, the physical mechanism of high-energy atom emission of metal, which is deeply related with phenomena in the precision processing, is open question, and there is discrepancy between experiments and previous theoretical simulations.

At the beginning of this thesis, we would like to briefly review previous studies about laser ablation and related issues.

1.1 Physical phenomena caused by irradiation with an ultrashort pulse laser

The development of ultrashort pulse lasers opened up a new research field, where many intensive investigations have been carried out because of its peculiarity. In this thesis, "ultrashort pulse" is referred to as a pulse with shorter duration time than relaxation time for electron-to-lattice energy transfer ($>$ ps). Therefore, irradiation of a solid surface with an ultrashort laser pulse creates a peculiar excited state, where a high-energy electron system coexists with a low-energy lattice system. This nonequilibrium state can not be created by other methods. Since typical time scale of the electron-to-lattice energy transfer is longer than the period of the phonon, if a sufficiently high-energy ultrashort pulse laser irradiates a solid surface, structural phase transition begins in the nonequilibrium state.

Until now, in the nonequilibrium state, specific phenomena have been reported. For example, a new struturual phase of carbon, so called, diaphite [1, 2] has been observed, which can only be produced via the nonequilibrium state with ultrashort pulse laser irradiation. This discovery accentuates a peculiarity of the nonequiribrium state. In addition, by irradiating ultrashort pulse laser on a solid surface, ultrafast structural change [3, 4], coherent phonon [5], hot plasma confined inside a cold solid (warm dense matter: WDM), and the emission of excessively high-

energy atoms/ions [6–9] have been reported. These studies have created numerous applications in industry (micro machining), information technology (optical memory, waveguide, photonics crystal), and medicine (surgery).

This nonequilibrium state is very complicated so that its systematic description does not exist. One of the most employed methods for investigating ultrashort laser-irradiated metals is the well-known two-temperature model (TTM) [10]. Figure 1.1 represents a main concept of the TTM. Ultrashort pulse laser irradiation on a metal surface changes the electron subsystem from the ground state into excited states by absorption of single or higher order multi-photon. The electron subsystem is thermalized to the Fermi-Dirac distribution with the electron temperature T_e, via electron-electron (el.-el.) interaction, of which the scattering time τ_{ee} is approximately 10-100 fs in metals [11, 12]. In this time scale, the electron subsystem and the lattice subsystem have not reached the local equilibrium state so that T_e is higher than the lattice temperature T_l. Ordinarily, the maximum T_e reaches more than 10 times higher T_e than the final temperature ($T_e \approx T_l$) since the heat capacity of electron is excessively smaller than that of lattice. T_l begins to increase by energy transfer from the electron subsystem via electron-phonon (el.-ph.) scattering, of which the relaxation time τ_{el} is larger than several picoseconds [13–16]. Therefore, under the assumption of instantaneous and the local thermalization in the electron subsystem and the lattice subsystem, ultrashort laser-irradiated metals can be described as $T_e \gg T_l$ long before τ_{el}. This explanation is the main concept of the TTM.

Based on the TTM, many previous studies [4, 17–23] have been successful for description of the experimental data. From next section, we explain the previous investigations particularly about the process of ablation, which is a key phenomenon for the laser processing.

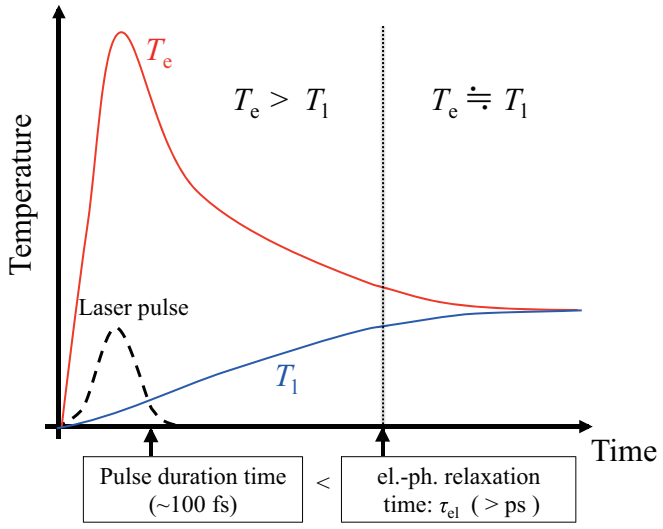

Figure 1.1: Schematic image of a main concept of the TTM and the time development of T_e and T_l.

1.2 Laser ablation

1.2.1 Spallation and phase explosion

Ablation is a process of removing materials from a solid surface by irradiating it with a laser. This phenomenon has been widely employed in industrial field as methods of the laser processing (cutting and drilling), the pulsed laser deposition [24, 25], and the nanoparticle production [26, 27]. It is important to investigate a physical mechanism of the ablation for higher-precision and more efficient processing. Until now, to elucidate the physical mechanism of ablation, molecular dynamics (MD) simulations have been performed in several materials (Al [28], Ag [29], Cu [30, 31], Au [32], Ni [32], and Pt [33]). These calculation results proposed the following explanation about the ablation process in a low-laser-fluence region.

Figure 1.2(a) represents an image of a process of spallation. By irradiating an ultrashort pulse laser on a surface, deposited laser energy creates an inertial stress confinement region since materials can not expand immediately. Subsequently, pressure begins to propagate inward from near the surface. After the propagation of the compressive pressure wave, a negative pressure region is generated by relaxation of the compressive pressure and tensile stress due to the surface expansion, so that creation and growth of voids proceed in this region. As a result, a molten surface layer is ejected. The previous MD simulations [29–32] showed that more than 10 nm molten layer is ejected at the ablation threshold fluence. This ablation process is called the spallation process, which is believed to be a phenomenon when an ultrashort pulse laser with the ablation threshold fluence is irradiated. By irradiating a low-fluence ultrashort pulse laser on a solid, an interface fringe pattern, which called a Newton ring, has been observed in time-resolved optical microscopy images [33–37]. This fringe is created by the interference between a laser pulse reflected at the surface of target and one reflected at the ejected layer. These observations certify ejection of a high dense material (solid or liquid) in ablation process by irradiation with a low-fluence laser. Therefore, from the point of view of the description of the Newton ring, the previous MD simulation results are qualitatively consistent with experiment.

Figure 1.2(b) represents an image of a process of phase explosion. As a laser fluence becomes higher, a thickness of the ejected layer becomes thiner, and eventually small clusters and atoms are emitted [28]. In this process, the main driving force of the ablation process is explained by the thermodynamic instability [38, 39] of the overheated surface. This ablation process is called the phase explosion process and a previous MD simulation qualitatively reproduce experimental results of cluster size distribution of emitted materials [40].

It means that, in the previous MD simulations, isolated atoms are not observed by irradiation with a laser whose fluence is near the ablation threshold fluence (in the spallation process), and the isolated atoms begin to be emitted by irradiation with higher-fluence laser (in the phase explosion process). This explanation has a fatal problem to describe ablation process near the ablation threshold fluence since atoms/ions are experimentally observed in the fluence [6–9]. In the next subsection, we explain the details of this problem.

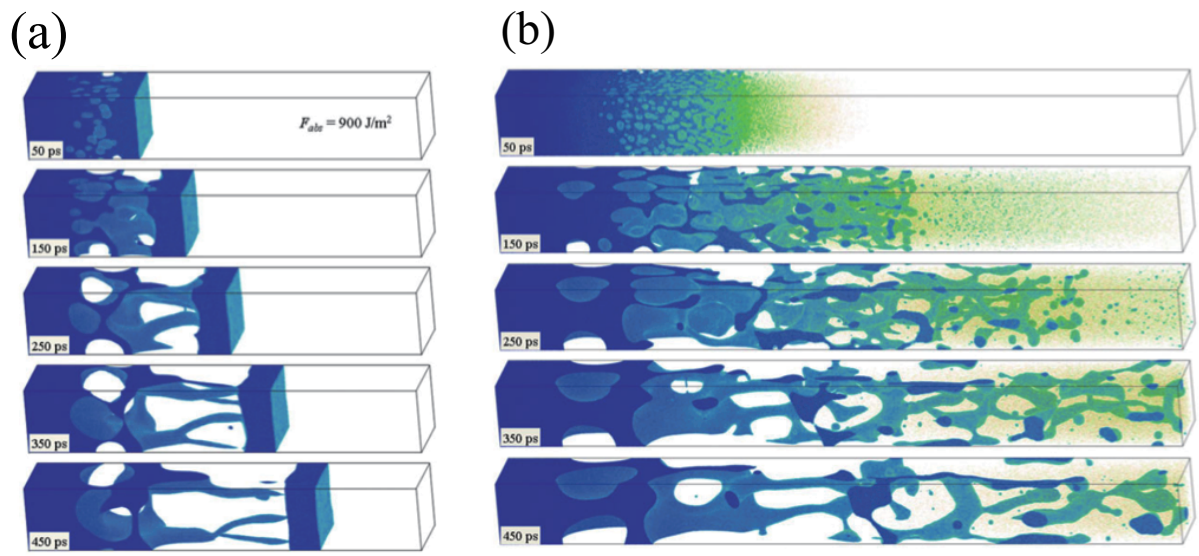

Figure 1.2: Images of the process of (a) spallation and (b) phase explosion [28]. These figures represent snapshots of MD simulations after irradiation of an aluminum surface with an ultrashort pulse laser with (a) $0.9\,\mathrm{J\,cm^{-2}}$ and (b) $2.0\,\mathrm{J\,cm^{-2}}$. The lateral dimensions of the computational cells are $94\,\mathrm{nm} \times 94\,\mathrm{nm}$.

1.2.2 Non-thermal ablation

Until now, specific phenomena have been observed by irradiation of metal surfaces with an ultrashort pulse laser, such as the emission of high-energy atoms/ions [6–9], which can not be observed by irradiation with long pulse laser. Also, it has been reported that energy distribution of emitted ions does not follow a shifted Maxwell-Boltzmann distribution [6]. These ablation processes, which can not be explained under the assumption of the local thermal equilibrium, is referred to as a non-thermal ablation. It is thought that ejection of non-molten materials [41–45] and less than nm order ablation [6, 7, 46] are also closely related with the non-thermal ablation. Some experimental results showed that the effect of the non-thermal ablation is dominant in the low-laser-fluence region [6, 7, 42, 44, 45]. One of the reasons for the specific attention to the non-thermal ablation by industry is that it can decrease the size of the thermal damage region and realize the precision processing [42, 44, 45]. To realize higher-precision processing and to optimize laser parameters, such as the wavelength and the laser fluence, the specific attention has been payed to the non-thermal ablation, though the physical mechanism of the non-thermal ablation is open question. These phenomena can not be explained the previous MD simulations since the atom emission is not observed near the ablation threshold fluence in these simulations, as mentioned in the above subsection. In other words, the origin of the high-energy atoms/ions emission [6–9], less than nm order ablation [6, 7, 46], and the non-molten

materials emission [41–45] have not been understood yet. Hence, there is a discrepancy between the experiment and the previous MD simulations about the explanation about the physical mechanism of the non-thermal ablation of metals.

Some previous studies proposed that this discrepancy coming from a lack of some physical mechanism of the previous MD simulations, where the force acting on atoms are assumed to be not changed even in the strongly excited electron subsystem ($T_e \sim 10^4\,\mathrm{K}$). Based on this consideration, some physical mechanisms have been proposed to explain the physical mechanism of the non-thermal ablation. One of the most famous one is a Coulomb explosion (CE) process, which is verified in the case of a semiconductor [47] and an insulator [48, 49], experimentally. By intense laser irradiation, electrons are emitted from an laser-irradiated surface due to the photoelectronic effect or the thermionic emission process, so that strong Coulomb interaction is created between positive charged atoms at the ionized surface. When the Coulomb interaction is strong enough to overcome the bonding force between these ions, these ions are emitted from the surface. The Coulomb repulsion force is proportional to the ionic valence so that the kinetic momentum is conserved between atoms. As a result, the peak of the emitted ions velocities is scaling to the valence of the emitted ions. These phenomena have been observed in the time-of-flight experiment with a semiconductor [47], an insulator [48], and a molecule system [50]. This observation has been regarded as the conclusive evidence of the CE process in these materials. On the other hands, the peak of the velocity of the Cu^{2+} is less than 1.5 times that of the Cu^{+} in the copper ablation [47]. Based on this observation, the experimental group [47] has insisted that the indication of the CE process does not be shown in copper. In addition, other experimental result [51] showed that the electric field is shielded within duration time of probe pulse (200 fs), and this fast electrostatic shielding is expected to be natural because the inverse of the plasma frequency is very fast (0.38 fs). It supports the consideration that the electric field due to the electron emission is shielded by high mobility electrons in metals before the Coulomb explosion process is caused. Moreover, a previous continuum model simulation [52] showed that electronic field near an laser-irradiated metal surface is excessively low because of the fast shield by free-electron like electrons in metals. Therefore, the validity of the Coulomb explosion process in metal is scarce.

Until now, other mechanisms have been proposed to describe the physical mechanism of the non-thermal ablation of metals. For examples,[1] some groups consider that the large repulsion force, which causes the non-thermal ablation, is attributed to the kinetic energy of free electron [19,20,53,54], and others insist that this force comes from the change of charge configuration. However, these mechanisms have not achieved to quantitatively describe the experimental results, and the validity of these explanations has not been discussed, sufficiently. Hence, the physical mechanism of the non-thermal ablation of metals is an open question.

[1] Since these mechanisms are closely related with our proposed mechanism to explain the non-thermal ablation of metals, their details will be explained in Chap. 3.

1.3 Purposes of this study

Purposes of our study are following two.

The first one is bridging the discrepancy between experiment and the previous theoretical studies about the explanation of the non-thermal ablation of metals. In particular, we attempt to elucidate the cause of the high-energy atom emission and the less than nm order ablation. The other is extending calculation models and developing codes to simulate the laser irradiated metal with an ultrashort pulse laser. Development of the calculation method will be useful for studies of various phenomena such as the WDM, ultrafast structural change [4, 55], and the formation of laser induced periodic surface structure (LIPSS) [56, 57].

1.4 Outline of this thesis

In Chap. 2, we discuss the effect of high electronic temperature on the ablation based on results of finite-temperature density functional theory (FTDFT) calculations. From these calculations, we propose a physical mechanism to describe the non-thermal ablation of metals, and show the significant contribution of the electronic entropy for this phenomenon. In Chap. 3, to show the validity of the proposed mechanism, we develop a calculation model in a continuum scheme to simulate the non-thermal ablation. We show that the ablation depth calculated with this continuum model (CM) agrees with the experimental results [58, 59] quantitatively in low-laser-fluence region. In Chap. 4, to analyze further details of the physical mechanism of the non-thermal ablation, we carry out TTM molecular dynamics (TTM-MD) simulation. In this simulation, we extend the calculation scheme of the TTM-MD and implement it in our developed code. In addition, we develop the function of interatomic potential (IAP) at high T_e and appropriate IAP is made. Using this IAP and the developed code, we carry out the TTM-MD simulations, and elucidate the physical mechanism of the non-thermal ablation near the ablation threshold. Moreover, we compare the TTM-MD calculation results of ablation depth with the CM calculation results and the experimental data [58, 59]. In Chap. 5, we develop a simple calculation model to estimate the threshold fluence for the non-thermal ablation. These simulation results show a possibility that the proposed mechanism can be applied to materials quite generally. Chapter 6 is devoted to summarize our results and show the future works.

2. Finite-Temperature Density Functional Theory (FTDFT) Calculation and Electronic-Entropy Driven (EED) Mechanism

In this chapter, we investigate the contribution of electronic state for the non-thermal ablation based on results of finite-temperature density functional theory (FTDFT) [60] calculations.

First, we explain basic idea of the density functional theory (DFT) [61, 62] and its extension to finite temperature. Subsequently, we show FTDFT calculation results, and based on it, we propose a physical mechanism to explain the non-thermal ablation of metals. A brief summary is given at the end of this chapter. The contents in this chapter have been published in Applied Physics Express, **11**, 046701 (2018).

2.1 Density functional theory (DFT)

DFT is one of the most standard and successful approaches to calculate electronic state of various materials, such as molecules and solids, from first principles. Here, we briefly describe its formalism and the main concept.

DFT is based on following two Hohenberg-Kohn (HK) theorems [61].

- In the ground state, the external potential $v(\boldsymbol{r})$ of the electronic system can be determined only by the electron density $\rho(\boldsymbol{r})$. Therefore, the total energy E can be expressed as the functional of $\rho(\boldsymbol{r})$:

$$E[\rho] = F[\rho] + \int v(\boldsymbol{r})\rho(\boldsymbol{r})d\boldsymbol{r}, \tag{2.1}$$

  where $F[\rho]$ is a universal functional in the sense that it is a functional independent from $v(\boldsymbol{r})$.

- The electron density of the ground state $\rho_0(\boldsymbol{r})$ minimizes E at the ground state:

$$E[\rho] \geq E[\rho_0]. \tag{2.2}$$

In Eq. (2.1), all the difficulties of the many-body problems are included in $F[\rho]$. If this universal functional is determined from a simple system, such as electron gas system, any electronic system would be solved exactly. However, the HK theorem do not provide a method to calculate electronic states because it does not provide $F[\rho]$.

Kohn and Sham [62] established a practical scheme, which is called KS method, for calculating electronic states of materials. They expressed $E[\rho]$ as

$$E[\rho] = K_s[\rho] + \frac{1}{2}\int \frac{\rho(\boldsymbol{r})\rho(\boldsymbol{r'})}{|\boldsymbol{r}-\boldsymbol{r'}|}d\boldsymbol{r}d\boldsymbol{r'} + \int \rho(\boldsymbol{r})v(\boldsymbol{r})d\boldsymbol{r} + E_{\rm xc}[\rho], \tag{2.3}$$

where $K_s[\rho]$ is the kinetic energy of hypothetical non-interacting electrons:

$$K_s[\rho] = \sum_i^N \int d\boldsymbol{r}\phi_i^*(\boldsymbol{r})\left(-\frac{1}{2}\nabla^2\right)\phi_i(\boldsymbol{r}). \tag{2.4}$$

Here, N is the number of electrons and $\rho(\boldsymbol{r})$ is determined from the non-interacting wave function $\phi_i(\boldsymbol{r})$

$$\rho(\boldsymbol{r}) = \sum_i^N |\phi_i(\boldsymbol{r})|^2, \tag{2.5}$$

where i denotes the i-th eigenstate. In the KS method, all the difficulties of the many-body problem are included in the exchange-correlation function $E_{\rm xc}[\rho]$. By using Eqs. (2.2), (2.3), and calculating variational of $E(\rho)$ with respect to $\phi_i(\boldsymbol{r})$ so that following equations can be derived:

$$\left[-\frac{1}{2}\nabla^2 + v_{\rm eff}(\boldsymbol{r})\right]\phi_i(\boldsymbol{r}) = \epsilon_i\phi_i(\boldsymbol{r}). \tag{2.6}$$

Here, ϵ_i is an orbital energy of ϕ_i and an effective potential $v_{\rm eff}$ is written as

$$v_{\rm eff}(\boldsymbol{r}) = v(\boldsymbol{r}) + \int \frac{\rho(\boldsymbol{r'})}{|\boldsymbol{r}-\boldsymbol{r'}|}d\boldsymbol{r'} + \frac{\delta E_{\rm xc}[\rho]}{\delta\rho(\boldsymbol{r})}. \tag{2.7}$$

Eqs. (2.5), (2.6), and (2.7) are called the Kohn-Sham (KS) equations. The ground state electron density ρ_0 and its energy $E[\rho_0]$ are obtained by solving these one-body self-consistent-field equations. However, form of the exchange-correlation energy functional $E_{\rm xc}[\rho]$ is non-trivial. Since the accuracy of this method depends on the exchange-correlation functional, the form of $E_{\rm xc}[\rho]$ has been investigated intensively and many kinds of $E_{\rm xc}[\rho]$ forms have been proposed. In a simple approximation, the form of $E_{\rm xc}[\rho]$ is assumed to depend only on the electron density at each point. In this approximation, which is called local density approximation (LDA), $E_{\rm xc}[\rho]$ is derived from that of the homogeneous electron gas (HED). Despite its simple form, this method has been widely applied and succeeded in calculating electronic structures. In generalized gradient approximation (GGA), the gradient of $\rho(\boldsymbol{r})$ is added to the form of the $E_{\rm xc}[\rho]$ of the LDA. In the GGA, various forms have been proposed, such as Becke (B88), Perdew-Wang (PW91), Perdew-Burke-Ernzerhof (PBE) [63,64], and PBEsol [65,66] functionals. It has been known that PBEsol functional gives structural properties closer to experimental values than the results of PBE functional. Thanks to these development of $E_{\rm xc}[\rho]$, DFT has been achieved successes.

2.2 Finite-temperature DFT (FTDFT)

In the previous section, DFT was briefly reviewed. This theory, combined with some approximations for $E_{\rm xc}[\rho]$, becomes a powerful and practical methods for calculation of many electrons in the ground state. However, the original DFT can be applied to only the ground state, since the HK theorem are verified only under the ground state.

A main purpose of our study is investigating the physical mechanism of the non-thermal ablation, which is not caused in the ground state, obviously. Therefore, we need an extended method in which electron structure at finite-temperature can be calculated. In this section, generalization of DFT to finite-temperature states is explained. This theory is called finite-temperature DFT (FTDFT), and throughout our study, we calculated electron structures at high T_e based on it.

Mermin proved the following theorem [60], which are analogous to the Hohenberg-Kohn theorems.

- In the equilibrium states, the external potential of the electronic system $v(\boldsymbol{r})$ can be determined only by the electron density $\rho(\boldsymbol{r})$. Therefore, physical quantities, such as the ground potential $\Omega[\rho]$, are unique functionals of $\rho(\boldsymbol{r})$:

$$\Omega[\rho] = F[\rho] + \int v(\boldsymbol{r})\rho(\boldsymbol{r})d\boldsymbol{r}. \tag{2.8}$$

- The electron density of the thermal equilibrium $\rho_0(\boldsymbol{r})$ minimizes $\Omega[\rho]$:

$$\Omega[\rho] \geq \Omega[\rho_0]. \tag{2.9}$$

As is the case of the KS methods at the ground state, Eq. (2.8) can be rewritten as

$$\Omega[\rho] = K_s[\rho] + \frac{1}{2}\int \frac{\rho(\boldsymbol{r})\rho(\boldsymbol{r'})}{|\boldsymbol{r}-\boldsymbol{r'}|}d\boldsymbol{r}d\boldsymbol{r'} + \int \rho(\boldsymbol{r})v(\boldsymbol{r})d\boldsymbol{r} - S[\rho]T_e + \Omega_{\rm xc}[\rho], \tag{2.10}$$

where $\Omega_{\rm xc}[\rho]$ is a exchange-correlation functional for the grand potential and $S[\rho]$ is the electronic entropy of the hypothetical non-interacting electrons. The many body effects of the electronic entropy are included in $\Omega_{\rm xc}$. The definition of S is

$$S = -2k_B \sum_i [f_i \ln f_i + (1-f_i)\ln(1-f_i))]. \tag{2.11}$$

Here, f_i is the occupation of the eigenenergy ϵ_i, the sum is over one-electronic eigenstates, and k_B is the Boltzmann constant. In the thermal equilibrium state of the electron subsystem, the occupation f_i can be expressed as the Fermi-Dirac distribution, $f_i = (1+e^{(\epsilon_i-\mu)/k_BT_e})^{-1}$, where

μ is the chemical potential. In the same way as the deviation of the ground state KS equations [Eqs. (2.5), (2.6), and (2.7)] in the previous section, following finite-temperature version KS equations can be derived:

$$\rho(\boldsymbol{r}) = \sum_i f_i |\phi_i(\boldsymbol{r})|^2, \tag{2.12}$$

$$\left[-\frac{1}{2}\nabla^2 + v_{\text{eff}}(\boldsymbol{r})\right]\phi_i(\boldsymbol{r}) = \epsilon_i \phi_i(\boldsymbol{r}), \tag{2.13}$$

$$v_{\text{eff}}(\boldsymbol{r}) = v(\boldsymbol{r}) + \int \frac{\rho(\boldsymbol{r'})}{|\boldsymbol{r} - \boldsymbol{r'}|} d\boldsymbol{r'} + \frac{\delta \Omega_{\text{xc}}[\rho, T_e]}{\delta \rho(\boldsymbol{r})}. \tag{2.14}$$

As well as the ground state KS equations, the finite-temperature KS equations [Eqs. (2.12), (2.13), and (2.14)] do not provide Ω_{xc}, which has to be obtained somehow.

Until now, some studies have investigated the form of Ω_{xc} and the finite-temperature effect on it [67–74]. A theoretical study [70] investigated contribution of the temperature dependence of Ω_{xc} in the HEG of various densities. This calculation result shows that, in the case of the electron density of condensed copper (Cu), difference between the calculated free energy using finite-temperature LDA [71] (Ω_{xc}) and that using ground-state LDA functional [75] (E_{xc}) is less than 1 % at $T_e < 50000\,\text{K}$. Since we focus on laser-irradiated metals with relatively low fluence laser, where T_e is almost always $T_e < 50000\,\text{K}$, the finite-temperature effect of Ω_{xc} is expected to be negligible. Therefore, we use zero-temperature exchange-correlation functionals (E_{xc}) throughout our study. This assumption is called the ground-state approximation, and has been widely employed to investigate phenomena caused by irradiation with an ultrashort pulse laser. Calculation results based on this assumption succeeded in reproducing experimental results, such as a dissapearence of the Jahn-Teller distortion [3], ultrafast melting [4], and bond hardening [17].

2.3 Methods and results

Here, we conducted first-principles calculations based on the FTDFT.

Before thermal equilibrium is achieved, a system irradiated with an intense ultrashort pulse laser can be represented as $T_e > T_l$ by employing the TTM. To examine T_e dependence of the stability of Cu, the electronic free energy F was calculated, which is defined as

$$F = E - T_e S. \tag{2.15}$$

In order to simplify the calculations, only the volume dependence at each T_e was considered. The face centered cubic (fcc) structure for primitive cells of Cu at different volumes were calculated in a range of T_e between 300 and 25000 K. To investigate the volume dependence of S at high T_e, we calculated the electronic band structure and the density of states (DOS) at V_0, which is the equilibrium volume at $T_e = 300\,\text{K}$, and at $2V_0$. Both calculations were conducted

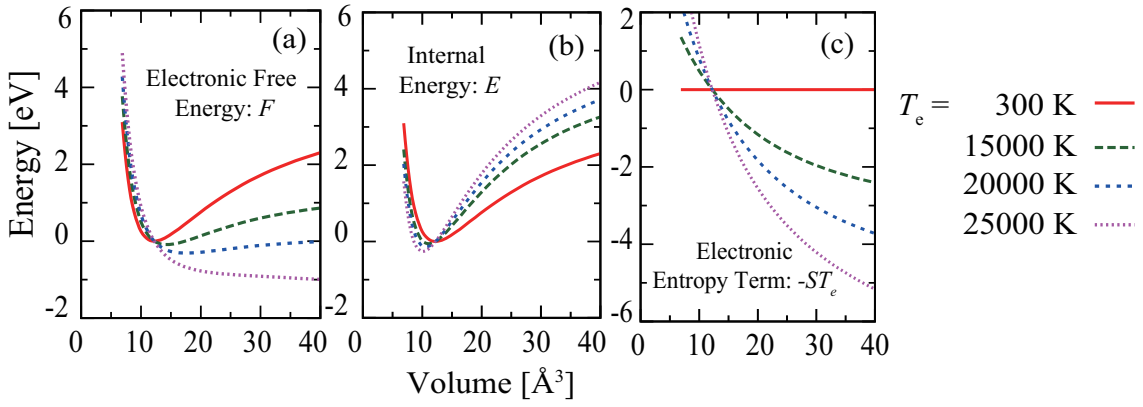

Figure 2.1: T_e dependence of (a) the electronic free energy F, (b) the internal energy E, and (c) the electronic entropy term $-ST_e$, as a function of the fcc primitive cell volume [77]. The bases of these vertical axes are set to each value at V_0.

at $T_e = 25000\,\mathrm{K}$. The relative error between our calculation value $V_0 = 12.23\,\text{Å}^3$ and the experimental value $V_{\mathrm{exp}} = 11.81\,\text{Å}^3$ [76] is 3.6 %.

These calculations were performed by using xTAPP code [78], in which we implemented the electronic entropy term calculation. The ultra-soft pseudopotential and the GGA-PBE exchange-correlation functional [63, 64] were used. In the ultra-soft pseudopotential, the $3d^{10}$ and $4s^1$ states are treated as valence states. The electronic structures were calculated with a cutoff energy of 1200 eV for the plane-wave basis and the Brillouin-zone k-point sampling of a Monkhorst-Pack mesh with $12 \times 12 \times 12$ k-points for the fcc primitive cell. The number of bands was set to 13. In the DOS calculation, only a number of the Brillouin-zone k-point sampling was changed to $16 \times 16 \times 16$ k-points.

The calculation results for F, E and $-ST_e$ as a function of V at $T_e = 300, 15000, 20000,$ and 25000 K are represented in Fig. 2.1. Figure 2.1(a) shows that the curvatures of electronic-free-energy curves become smaller as the values of T_e increase. Between 300 and 20000 K, the minimum points that corresponds to equilibrium volume at each T_e shift to larger values. Eventually, between 20000 and 25000 K, the minimum point vanishes. These results indicate that if atoms can freely change their interatomic distance, such as atoms near a surface, and T_e near the surface keeps above 25000 K, then they can not be condensed and are emitted from the surface.

The present results are qualitatively consistent with previous studies for W [79–82] and for gold [21, 83]. However, some physical origins have been proposed to explain the minimum point vanishment of F at high T_e, such as the kinetic energy of free electrons [19, 20, 53, 54] and the change of charge configuration [82]. The former one insisted that the kinetic energy of the free-electron like electrons becomes large at high T_e so that the minimum point vanishes.

The other one proposed the following explanation about the minimum point vanishment of W, which has half-filled d orbitals. At high T_e, electrons are transferred from localized d, f states to delocalized s, p states. As a result, the ion-ion interaction becomes more repulsive since a number of delocalized electrons, which screen a force between ions, is decreased.

To discuss the validity of these explanations and a main contribution for the disappearance of the minimum point in Fig. 2.1(a), E and $-ST_e$, which are components of F, are plotted in Figs. 2.1(b) and (c), respectively. Figure 2.1(b) represents that the values of E at high T_e are larger than these at low T_e in the region of $V > V_0$. On the contrary, Fig. 2.1(c) shows that the values of $-ST_e$ at high T_e are smaller than those at low T_e in the region of $V > V_0$. Therefore, we found that the main contribution for the disappearance of the electronic free energy minimum originates from $-ST_e$, not E. If the previous explanations were correct, lattice instability should appear in E, but Figs. 2.1(b) and (c) represents that the effect comes from $-ST_e$. Therefore, we considered that a different explanation is needed to explain the minimum point vanishment of F.

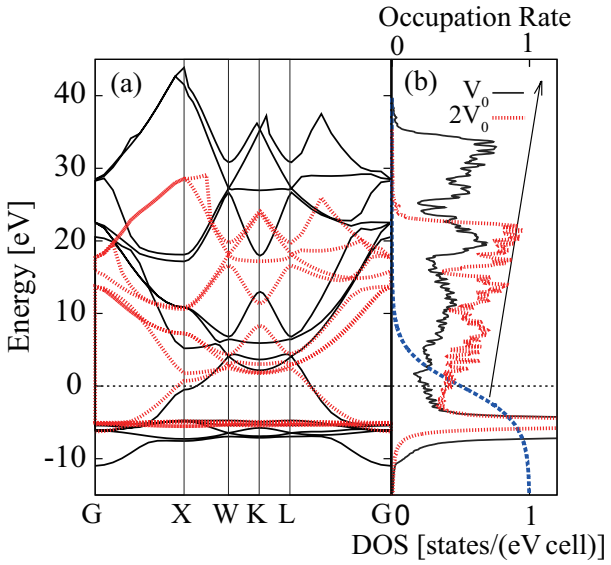

Figure 2.2: (a) Band structures and (b) DOS at $T_e = 25000\,\mathrm{K}$ [77]. Solid black and red dotted lines represent V_0 and $2V_0$, respectively. The blue dashed line is the Fermi-Dirac distribution at $T_e = 25000\,\mathrm{K}$.

Subsequently, to discuss the reason for this large benefit of S at large volume, the band structures and the DOS at different volumes of V_0 and $2V_0$ are plotted in Fig. 2.2. The local DOS near the chemical potential at a large volume of $2V_0$ is larger than that at V_0, and from the definition of S [Eq. (2.11)], this change increases the value of S. A physical origin of this change of the band structure can be easily understood by decrease of the overlap of atomic orbital due to the increased interatomic distance at the large volume. Although these consideration for the benefit of S were also mentioned briefly in a previous study [81], this study did not

relate this benefit of S with ablation process. Original point here is attributing the origin of the non-thermal ablation to the benefit of S at high T_e due to the change of the band width.

Based on these results and considerations, we propose the following explanation about the physical mechanism of the non-thermal ablation of metals. A schematic image of this explanation is shown in Fig. 2.3. By irradiating a metal surface with an ultrashort pulse laser, laser energy is absorbed in the electronic subsystem [Fig. 2.3(a)] so that T_e near surface increases [Fig. 2.3(b)]. At excessively high T_e ($\sim$ eV), condensed state becomes instable due to the effect of the electronic entropy term so that non-thermal ablation occurs [Fig. 2.3(c)]. We called this explanation an electronic entropy-driven (EED) mechanism. It is an important point that this explanation does not require the neutrality breakdown by electron emission, which is denied by both experimental [51] and the theoretical [84] results in the case of metal ablation. We expect that the EED mechanism can be applied not only to Cu, because the physical explanation given here is not specific and can be applied to all metals, and furthermore to some narrow gap semiconductors.

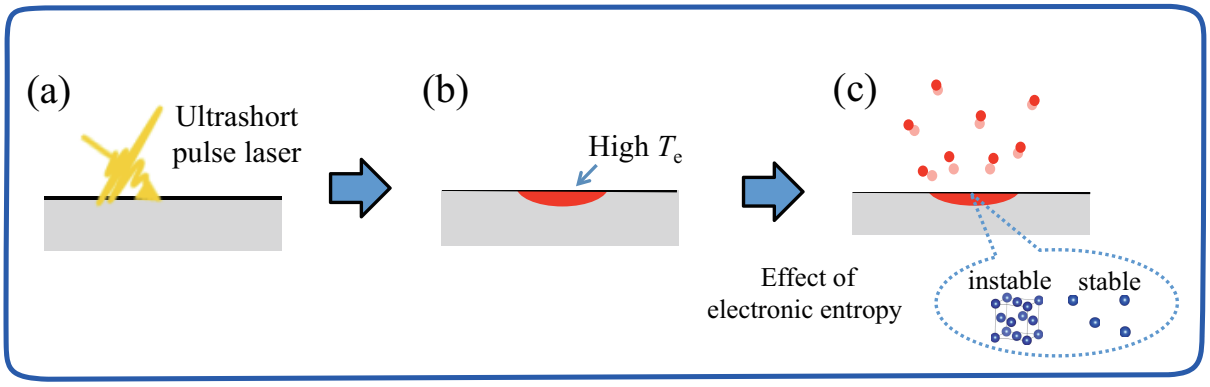

Figure 2.3: Schematic image of the proposed EED mechanism. (a) By irradiating an ultrashort pulse on a metal surface, laser energy is absorbed in the electronic subsystem. (b) T_e near surface increases. (c) At excessively high T_e ($\sim$ eV), condensed state becomes instable due to the effect of the electronic entropy term so that non-thermal ablation occurs.

2.4 Summary

In this section, we showed that the condensed state of Cu becomes instable around 25000 K due to an increase of the electronic entropy S. Moreover, based on the DOS and the band calculations, we considered that the increase of the electron DOS near the chemical potential at large volume brings about the large benefit of S and leads to the non-thermal ablation of Cu. We call this explanation the electronic-entropy driven (EED) mechanism and propose it to

explain the non-thermal ablation of metals. Original point here is attributing the origin of the non-thermal ablation to the benefit of S at high T_e due to the change of the band width.

3. Continuum Model (CM) Simulation

In this chapter, we develop a calculation model for a continuum model (CM) simulation, in which the EED mechanism is included. Using the developed model, we calculated the ablation depth to achieve following two purposes. One is discussing the validity of the developed calculation model and the EED mechanism. The other is examining how S contributes to the ablation depth.

In Sec. 3.1, basic idea of the CM model is described. After calculation details, such as parameters and ablation criteria, are explained in Secs. 3.2 and 3.3, we show calculation results in Sec. 3.4. At last, a brief summary is made in Sec. 3.5. The contents in this chapter have been published in Applied Physics Express, **11**, 046701 (2018).

3.1 Basic idea

To calculate the ablation depth, we simulated time and space development of T_e and T_l in a Cu film irradiated with an ultrashort pulse laser. Based on the TTM [10], these values were calculated by solving the following two-coupled differential equations for the electron [Eq. (3.1a)] and the lattice [Eq. (3.1b)] subsystems,

$$C_e(T_e)\frac{\partial T_e}{\partial t} = \kappa_e(T_e, T_l)\nabla^2 T_e - G(T_e - T_l) + I(T_e, T_l), \tag{3.1a}$$

$$C_l(T_l)\frac{\partial T_l}{\partial t} = G(T_e - T_l). \tag{3.1b}$$

Here, indices e and l indices denote the electron and lattice subsystems, respectively. C is the heat capacity, κ is the thermal conductivity, G is the electron-phonon heat transfer constant, and I is a source term, which represents the energy deposition by the laser pulse.

The lattice thermal diffusion is neglected because values of κ_l of pure metals are much smaller than that of κ_e. In addition, the electronic thermal diffusion along a surface can be neglected since the sum of the laser penetration depth $\delta = 13\,\mathrm{nm}$ [85] and the mean free path of electrons $\delta_{\mathrm{mfp}} = 42\,\mathrm{nm}$ [86] of Cu is much smaller than the typical radius of the laser spot. Therefore, one-dimension approximation is expected to be valid so that we consider only depth direction z. To solve Eqs. (3.1a) and (3.1b), the finite-difference methods are used, where the time step Δt and space step Δz are 10 as and 1 nm, respectively. These values satisfy the von Neumann stability criterion [87] $\Delta t < 0.5(\Delta z)^2 C_e(T_e)/\kappa(T_e, T_l)$ throughout our simulation. The Neumann

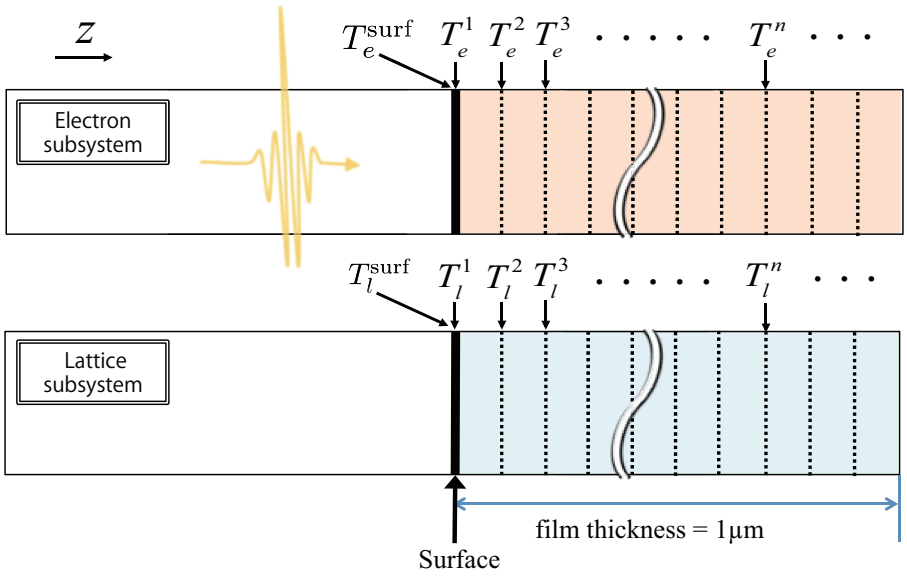

Figure 3.1: Schematic image of our CM simulation to calculate the ablation depth. Using one-dimension approximation, only depth direction z is considered. Thickness of the laser irradiated film is 1 μm. T_e^n and T_l^n represent T_e and T_l at the n-th space point, respectively. In addition, T_e^{surf} and T_l^{surf} represent T_e and T_l at a film surface point. In the initial condition, these were set to $T_e^{\mathrm{surf}} = T_e^1$ and $T_l^{\mathrm{surf}} = T_l^1$. T_e^n and T_l^n were calculated by solving Eqs. (3.1a) and (3.1b).

boundary condition ($\nabla T_e = 0$) is used at a film surface and a film bottom. The Cu film thickness is 1 μm.

Figure 3.1 represents a schematic image of our CM simulation. T_e^n and T_l^n represent T_e and T_l at the n-th space point, respectively. In addition, T_e^{surf} and T_l^{surf} represent T_e and T_l at a film surface point. In a initial condition, these were set to $T_e^{\mathrm{surf}} = T_e^1$ and $T_l^{\mathrm{surf}} = T_l^1$. It should be noted that the surface point moves inward if ablation occurs. Ablation criteria are explained in Sec. 3.3.

3.2 Parameters

To accurately calculate time and space development of T_e and T_l, close attention should be paid to determine parameters in Eqs. (3.1a) and (3.1b). In this section, we explain values of used parameters in Eqs. (3.1a) and (3.1b).

Electronic heat capacity: $C_e(T_e)$

Following equation is the definition of $C_e(T_e)$:

$$C_e(T_e) = \frac{\partial E(T_e)}{\partial T_e}. \tag{3.2}$$

T_e dependent heat capacity $C_e(T_e)$ is obtained by fitting previous FTDFT calculation results [88, 89]. Fitting functions are

$$C_e(T_e) = \begin{cases} \gamma T_e & \cdots 0 \leq T_e \leq T_e' \\ A(T_e - T_e')^{\frac{1}{b}} + C_e(T_e') & \cdots \quad T_e' < T_e. \end{cases} \tag{3.3}$$

The FTDFT calculations [88,89] show that the behavior of C_e is significantly changed around T_e'. Here, A, b, and γ are fitting parameters. As a results of fitting, we obtained $\gamma = 96.8\,\mathrm{J\,m^{-3}\,K^{-2}}$, $A = 1.115\,\mathrm{J\,m^{-3}\,K^{-(1+\frac{1}{b})}}$, $b = 1.714$.

Lattice heat capacity: $C_l(T_l)$

According to the Dulong-Petit law, $C_l = 3.51\,\mathrm{J\,cm^{-3}\,K^{-1}}$ is given by the observed equilibrium volume V_{exp} [90]. Since C_l can be assumed to be constant above the Debye temperature $T_D = 343\,\mathrm{K}$ [91], this value is a good approximation in our simulation, where $T_l > T_D$ is satisfied shortly after an ultrashort pulse laser reaches a surface of the Cu film.

Electronic thermal conductivity: $\kappa_e(T_e, T_l)$

Based on the kinetic theory of gases, $\kappa_e(T_e, T_l) = \frac{1}{3} v_F^2 C_e(T_e) \tau_e(T_e, T_l)$ can be derived. Here, $v_F = 1.57 \times 10^6\,\mathrm{m\,s^{-1}}$ [86] and $\tau_e(T_e, T_l)$ are the Fermi velocity and the electron relaxation time, respectively. τ_e is estimated using Matthiessen's rule $\tau_e^{-1}(T_e, T_l) = \tau_{ee}^{-1}(T_e) + \tau_{el}^{-1}(T_l)$, where τ_{ee}^{-1} and τ_{el}^{-1} is the electron-electron scattering time and the electron-lattice scattering time, respectively. $\tau_{el}^{-1}(T_l)$ is expressed as $\tau_{el}^{-1}(T_l) = B_l T_l$, and according to the Fermi liquid theory, $\tau_{ee}(T_e, T_l)$ for electrons with energy near the chemical potential is approximated as [11]: $\tau_{ee}^{-1}(T_e) = A_e T_e^2$, where A_e and B_l are typically assumed to be constant [11, 92, 93]. $B_l = 1.98 \times 10^{11}\,\mathrm{s^{-1}\ K^{-1}}$ is determined so as to reproduce experimental value $\kappa_e = 3.99\ \mathrm{W\ cm^{-1}\ K^{-1}}$ [94] at low temperature. $A_e = 2.22 \times 10^6\ \mathrm{s^{-1}\ K^{-2}}$ was obtained by a recent first-principles calculation [95]. This value is consistent with the experimental result [93], in which $6.68 \times 10^5 < A_e < 2.89 \times 10^6\ \mathrm{s^{-1}\ K^{-2}}$ was reported.

Electron-phonon heat transfer constant: G

According to Allen [96], by using the electron-phonon transfer constant G, the thermal relaxation due to the electron-phonon scattering can be written as $C_e(\partial T_e/\partial t) = G(T_e - T_l)$ in the case of $T_e \gg T_l$. Many calculations have been carried out to estimate the value of G, and various values have been reported. For example, the value of G at $T_e = 20000\,\mathrm{K}$ predicted by Lin *et al.* [89] is 6 times larger than the value predicted by Migdal *et al.* [97, 98]. It was reported that the T_e dependence of DOS, which causes lower shift of d-band at high T_e for Cu, reduces the value of G [97, 99], and the T_e dependence of DOS is considered in the latter calculation but is neglected in the former one. Therefore, in our calculation, we used the latter T_e independent $G = 1.0 \times 10^{17}\ \mathrm{W\ K^{-1} m^{-3}}$ [97], which is consistent with experimental value [14] at low T_e. According to Migdal *et al.* [99], T_e dependence of G is small at least below $T_e = 60000\,\mathrm{K}$. In our calculation in Sec. 3.4, this situation is satisfied when laser peak fluence J_0 is approximately below $1.5\,\mathrm{J\,cm^{-2}}$. To analyze the G dependence of the ablation depth, we performed the ablation depth calculation using the T_e dependent $G(T_e)$ of Lin *et al.* [89]. This result is shown in Appendix A.

Source term: $I(T_e, T_l)$

Here, time distribution of laser fluence is expressed by the Gaussian distribution. The source term $I(T_e, T_l)$ is assumed to be [16]

$$I = \sqrt{\frac{\beta}{\pi}} \frac{(1 - R_n^{\mathrm{L}}(J_0))J_0}{t_p(\delta + \delta_b)} \exp\left[-\frac{z}{\delta + \delta_b} - \beta\Big(\frac{t}{t_p}\Big)^2 \right], \tag{3.4}$$

where t is the elapsed time after the laser fluence peak reaches the film surface, t_p is the duration time of the laser, δ_b is the ballistic range of electrons, and $\beta = 4 \ln 2$. $R_n^{\mathrm{L}}(J)$ is a local reflectivity

of the region irradiated with a laser whose fluence is J. The reflectivity has been reported to depend on the number of pulses n and laser fluence J because of the laser-structured surface and the change of the dielectric constant of the irradiated material [100]. Hence, to compare the simulation results with the experimental results [58, 59], where more than a few tens [58] or one hundred [59] laser pulses irradiate on the sample, the change of reflectivity must be considered. However, it is too difficult to consider these effects without experimental results. Therefore, in our calculations, reflectivity of n-th laser irradiation $R_n^L(J)$ were determined by fitting to an experimental reflectivity [100]. Details of a method to derive $R_n^L(J)$ are explained in Appendix B.

The laser penetration depth $\delta(T_e, T_l)$ is determined using a critical-point model [101,102]. The critical-point model is based on the Drude model with three Lorentzian terms. In this model, the dielectric constant $\epsilon(T_e, T_l)$ is calculated by solving the following equation:

$$\begin{aligned}\epsilon(T_e, T_l) &= \epsilon_\infty - \frac{\omega_D^2}{\omega^2 + i\gamma(T_e, T_l)\omega} \\ &\quad + \sum_{p=1}^{3} B_p \Omega_p \left(\frac{e^{i\theta_p}}{\Omega_p - \omega - i\Gamma_p} + \frac{e^{i\theta_p}}{\Omega_p - \omega - i\Gamma_p} \right) \\ &= \epsilon_1 + i\epsilon_2. \end{aligned} \tag{3.5}$$

Here, ϵ_∞ is a high-frequency limit dielectric constant, ω_D is the plasma frequency, ω is the laser frequency, $\gamma(T_e, T_l) = 1/\tau_e(T_e, T_l)$ is the damping coefficient, p is a number of oscillators, B is a weight factor, and Ω, θ, and Γ are energy of the gap, phase, and broadening, respectively. To represent the interband transition effect, the Lorentzian terms is added to the Drude term, in which T_e and T_l dependence are included via $\gamma(T_e, T_l)$. To solve Eq. (3.5), we used estimated values of these parameters (ϵ_∞, ω_D, B_p, Ω_p, θ_p, and Γ_p) in the previous study [103]. $\delta(T_e, T_l)$ and $R^L(T_e, T_l)$ can be determined from the following Fresnel functions:

$$R^L = \frac{(f_1 - 1)^2 + f_2^2}{(f_1 + 1)^2 + f^2}, \qquad \delta = \frac{2\omega f_2}{c}. \tag{3.6}$$

Here, c is light speed, and definitions of the normal refractive index f_1 and extinction coeficient f_2 are

$$f_1 = \sqrt{\frac{\epsilon_1 + \sqrt{\epsilon_1^2 + \epsilon_2^2}}{2}}, \qquad f_2 = \sqrt{\frac{-\epsilon_1 + \sqrt{\epsilon_1^2 + \epsilon_2^2}}{2}}. \tag{3.7}$$

Although $R^L(T_e, T_l)$ also can be calculated in this model, the reflectivity change due to many pulse irradiation can not be included so that this $R^L(T_e, T_l)$ is expected to be insufficient for our study. Therefore, this model was used only to calculate the value of $\delta(T_e, T_l)$. The ballistic range was approximated as $\delta_b(T_e, T_l) = \tau_e(T_e, T_l)v_F$ [16].

It is noted that the melting of Cu is neglected in our calculations. In other words, all values of the used parameters are the value of the solid. This assumption is expected to be suitable

for simulation of non-thermal ablation because molten materials were not detected experimentally [41–45] in this ablation.

3.3 Ablation criteria

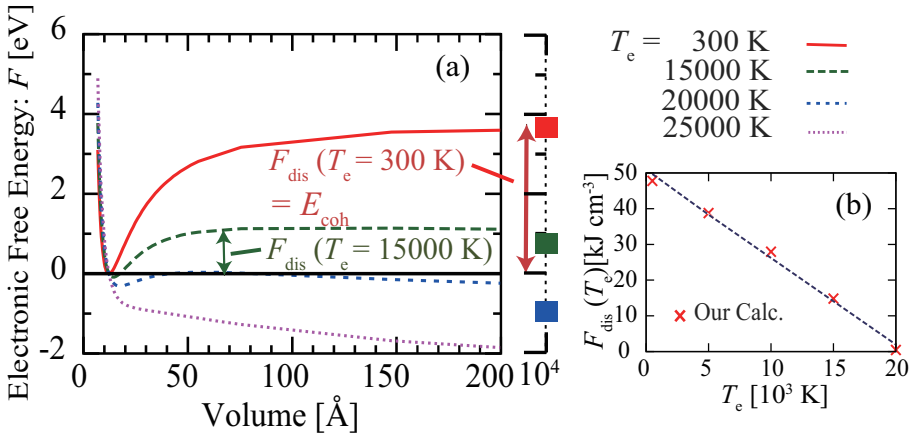

Figure 3.2: (a) T_e dependence of F as a function of the primitive fcc structure volume. (b) T_e dependence of $F_{\rm dis}(T_e)$. Cross marks represent the calculated data and the dotted line represent the fitting of these data as a linear function [77]. Calculation conditions are same as Sec. 2.3.

By solving Eqs. (3.1a) and (3.1b), we can calculate time development of T_e and T_l but can not calculate the ablation depth. In this section, we explain the assumptions and the developed mathematical model, to calculate the ablation depth based on the EED mechanism.

It is assumed that, to cause ablation, the lattice energy $E_l(T_l^n)$ at a n-th point, which is defined as $E_l(T_l^n) = C_l\, T_l^n$, must overcome the activation barrier for dissociation $F_{\rm dis}(T_e^n)$. $F_{\rm dis}(T_e^n)$ represents the difference between a value of F at V_0 and the maximum value of F in the region where $V > V_0$ (see: Fig. 3.2). Note that $F_{\rm dis}$ depends on $T_e^n(t)$, in which electronic entropy effect is included. At low T_e, $F_{\rm dis}(T_e^n)$ corresponds to the cohesive energy $E_{\rm coh} = 47.76\,{\rm kJ\,cm^{-3}}$, the value of which is our calculation result [Fig. 3.2(b)], and which agrees well with the experimental value $47.34\,{\rm kJ\,cm^{-3}}$ [90, 104]. In addition to this assumption, we assume that ablation occurs only at the surface point because the bulk can not expand freely. Taken together, the criterion for ablation can be expressed as the following inequality:

$$E_l(T_l^{\rm surf}) > F_{\rm dis}(T_e^{\rm surf}). \tag{3.8}$$

Figure 2.1(b) shows that the values of the internal energy E at large volume are larger than those of E at V_0, even at high T_e. Therefore, the absorption of the latent heat $E_{\rm late}$ is required for ablation from the electronic subsystem. In the present simulation, $E_{\rm late}$ is assumed as

$$E_{\rm late}(T_l^{\rm surf}) = E_{\rm coh} - E_l(T_l^{\rm surf}). \tag{3.9}$$

If the surface point satisfies Eq. (3.8), then $E_{\rm late}(T_l)$ begins to be absorbed as the latent heat from the electronic subsystem at the surface point. We consider that the delay time $t_{\rm abs} = \Delta z/v_{\rm s}$ is required to cause ablation after a point, becomes the surface point because ablation would not occur until a pressure wave, created by previous ablation, passes through the point. The velocity of the pressure wave is assumed to be the speed of sound, $v_{\rm s} = 4760\,{\rm m\,s^{-1}}$ [105]. In other words, we assume that the surface moves at the speed of sound due to the ablation. To represent ablation, the surface point is removed from the simulation, and the next point becomes the new surface point if the surface point satisfies Eq. (3.8) after the absorption of $E_{\rm late}(T_l)$ from the electronic subsystem.

3.4 Results

First, we show calculation results of the time development of T_e and T_l after irradiating ultrashort pulse laser with the laser pulse duration time t_p of 100 fs and a wavelength of 800 nm. The initial T_e and T_l were set to 300 K. In these calculations, $R^{\rm L}_{100}(J)$ was used.

Figure 3.3 represents space distribution of T_e and T_l after (a), (c), (e), (g) $J_0 = 0.4\,{\rm J\,cm^{-2}}$ and (b), (d), (f), (h) $J_0 = 1.5\,{\rm J\,cm^{-2}}$ laser pulse irradiation from the left. Each figures represent T_e and T_l at (a), (b) $t = 0.4$ ps, (c), (d) 1 ps, (e), (f) 10 ps, and (g), (h) 30 ps after the center of the laser pulse reaches the surface initially located at $z = 0$. Red, blue, and green lines represent T_e, T_l, and an ablation criteria lattice temperature $T^n_{l,{\rm thr}}$, respectively. $T^n_{l,{\rm thr}} = F_{\rm dis}(T^n_e)/C_l$ is the definition of $T^n_{l,{\rm thr}}$. According to the ablation criteria explained in Sec. 3.3, if $T^{\rm surf}_l \geq T^{\rm surf}_{l,{\rm thr}}$ is satisfied after the energy absorption $E_{\rm late}(T^{\rm surf}_l)$, the surface point is judged that ablation is caused here. In other words, when the blue lines overcome the green lines at the surface point during $t_{\rm abs}$, ablation is assumed to occur. In Figs. 3.3(a)-(f), T^n_e is larger than T^n_l near the surface. On the other hand, in Figs. 3.3(g), (h), $T^n_e \approx T^n_l$ is satisfied, which means that these systems reach the local equilibrium states. Figures 3.3(a), (c), (e), (g) show that the ablation criteria is not satisfied throughout all simulation time. This result represents that ablation is not caused by a laser irradiation of $J_0 = 0.4\,{\rm J\,cm^{-2}}$. On the contrary, Fig. 3.3(b) shows that the value of the $T^n_{l,{\rm thr}}$ becomes smaller than $T^{\rm surf}_l$. Therefore, ablation is caused and the surface moves to the right [see: Figs. 3.3(d), (f), (h)]. Around $t = 10$ ps, ablation was finished since $T^{\rm surf}_l \leq T^{\rm surf}_{l,{\rm thr}}$ is satisfied. Consequently, we obtained the ablation depth, a value of which is 48 nm, of the $J_0 = 1.5\,{\rm J\,cm^{-2}}$ laser pulse irradiation. These simulations were carried out from $J_0 = 0.5$ to $10\,{\rm J\,cm^{-2}}$, to calculate the laser fluence dependence of the ablation depth.

The calculation results of the ablation depth and experimental results [58, 59] are plotted in Fig. 3.4. It should be noted that there are no adjustment parameters to reproduce these experimental results [58, 59]. Simulations were conducted for each reflectivity $R^{\rm L}_{10}(J)$, $R^{\rm L}_{50}(J)$ and $R^{\rm L}_{100}(J)$. The thin lines indicate that the dependence on the number of pulses is not large between the 10 and 100th pulses. Moreover, these thin lines indicate that the calculation results with consideration of the electronic entropy effect are in good agreement with the experimental

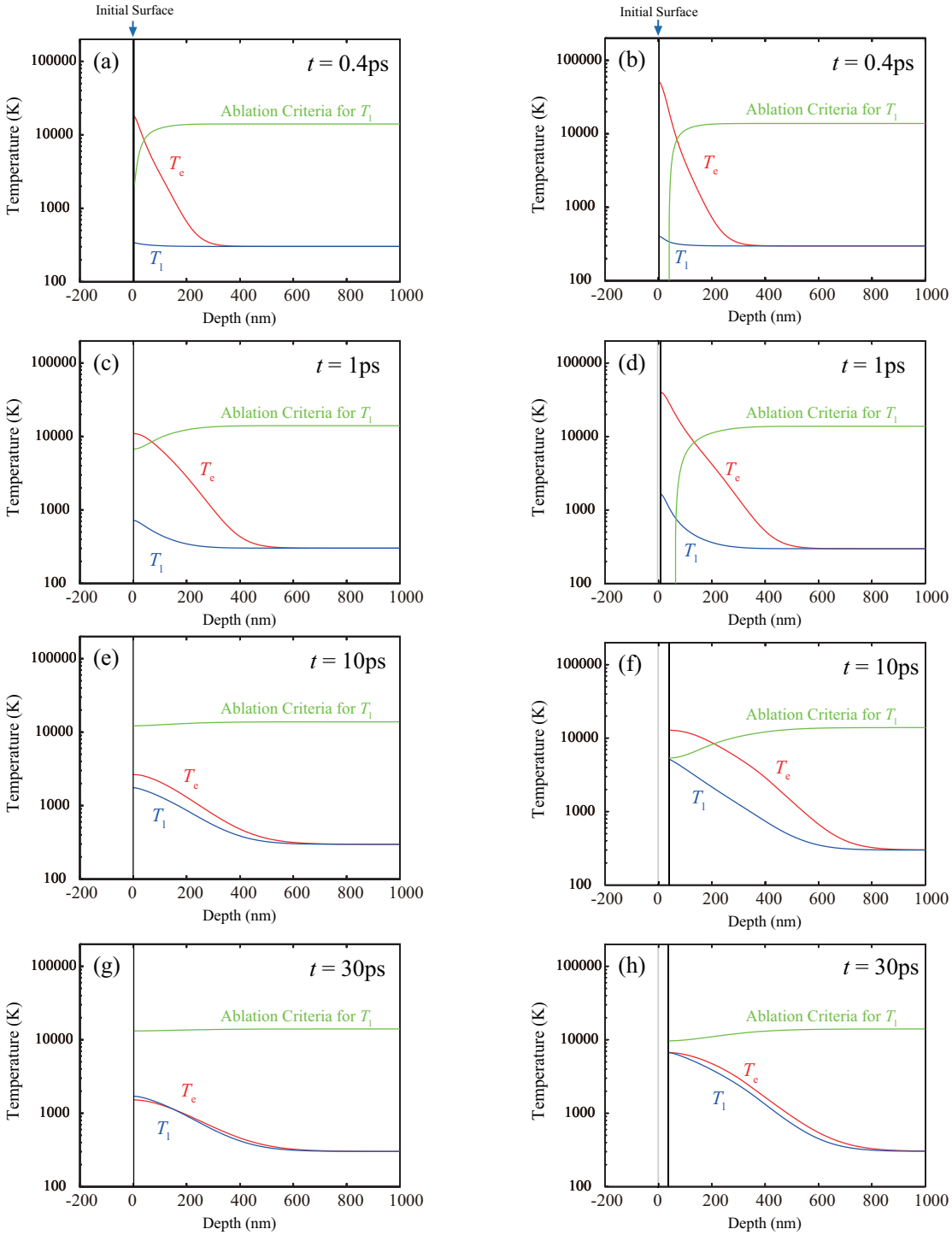

Figure 3.3: Space distribution of T_e and T_l after laser irradiation with (a), (c), (e), (g) $J_0 = 0.4\,\mathrm{J\,cm^{-2}}$ and (b), (d), (f), (h) $J_0 = 1.5\,\mathrm{J\,cm^{-2}}$. Elapsed times of the each figure are (a), (b) $t = 0.4\,\mathrm{ps}$, (c), (d) $1.0\,\mathrm{ps}$, (e), (f) $10\,\mathrm{ps}$, and (g), (h) $30\,\mathrm{ps}$. Red, blue, and green lines represent T_e, T_l, and the ablation criteria lattice temperature $T^n_{l,\mathrm{thr}}$, respectively.

results [58, 59] in the low-laser-fluence region ($\sim 5\,\mathrm{J\,cm^{-2}}$), where the effect of the non-thermal ablation is expected to be dominant [6, 7, 42, 44, 45]. We consider that the disagreement in the high-laser-fluence region is due to the lack of physical mechanics, such as the ejection of liquid droplets by the recoil pressure [44] created by ablation. On the contrary, in the low fluence region, this effect is expected to be little because molten material is not observed [42, 44, 45] in this region.

The dashed bold line in Fig. 3.4 represents calculation results when only thermal ablation is considered, in which the effect of electronic entropy is ignored. In other words, in these calculations, T_e independent $F_{\mathrm{dis}} = E_{\mathrm{coh}}$ was used instead of $F_{\mathrm{dis}}(T_e)$ for the ablation criterion in Eq. (3.8). This line has no tail near the ablation threshold, and this result implies that this simulations can not qualitatively reproduce experimental data. Based on these results, we suggest that non-thermal ablation in the low-laser-fluence region is caused by the electronic entropy effect.

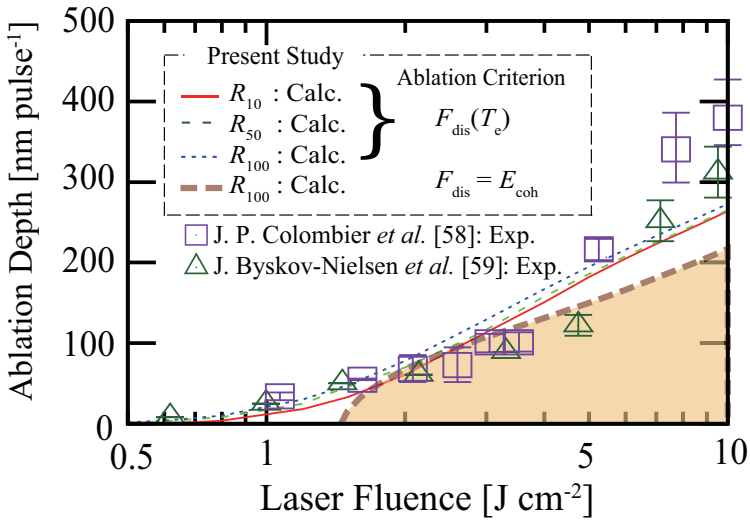

Figure 3.4: Comparison of the ablation depth from the simulation results [77] and the experimental results [58,59]. R_n^L denotes the reflectivity of the n-th laser irradiation pulse was used in these simulations. The thin lines and the bold line represent our calculation results, where $F_{\mathrm{dis}}(T_e)$ and a constant $F_{\mathrm{dis}} = E_{\mathrm{coh}}$ were used as the criteria for ablation [Eq. (3.8)], respectively. Square [58] and triangle [59] symbols represent the experimental data.

3.5 Summary

In this chapter, we developed the calculation model for the CM simulation, where the EED mechanism are included, to calculate the ablation depth. Our calculation results showed that this model can reproduce experimental results in the low-laser-fluence region. Moreover, we found that the effect of the electronic entropy has dominant effect in the low-laser-fluence region, where the non-thermal ablation effect has been known to be large. These results strongly support the validity of the developed model and the EED mechanism, and show that the electronic entropy effect is dominant for the non-thermal ablation of metals.

4. Two-Temperature Model Molecular Dynamics (TTM-MD) Simulation

In the previous chapter, we extended the CM, where the EED mechanism is included, and showed that this model can reproduce the experimental data [58, 59] in the low-laser-fluence region. However, it is difficult for the CM simulations to analyze the detail of the ablation process and to absolutely discuss the validity of the EED mechanism. To overcome these problems, under the TTM, we performed molecular dynamics (MD) simulation, which is called a TTM-MD simulation. Before we carried out the TTM-MD simulations, we extended the TTM-MD simulation model since the law of conservation of energy is not satisfied in the previous calculation model.

Outline of this chapter is following. In Sec. 4.1, we explain the extended TTM-MD calculation model, where the law of conservation of energy is satisfied. Subsequently, we explain a strategy of making T_e-dependent interatomic potential (IAP) and show the validity of the IAP in Sec. 4.2. In Sec. 4.3, we show results of test calculations to exhibit that our calculation model satisfies the law of conservation of energy. In Sec. 4.4, we show results of the TTM-MD simulations. Finally, we make a summary in Sec. 4.5.

4.1 TTM-MD model

In this section, we explain the extended TTM-MD simulation model and details of the flow of the simulation.

4.1.1 Simulation model

Here, we explain the calculation model to simulate atom dynamics in ablation caused by irradiating ultrashort pulse laser on a Cu film. We carry out large-scale atomistic simulations with the hybrid calculation model, in which the CM and the classical MD methods are combined. This calculation model is called the TTM-MD model, and Fig. 4.1 represents a schematic image of the TTM-MD model.

Owing to the TTM, we can include the electronic effects into the MD simulation, such as the electronic thermal diffusion, the energy deposited by laser irradiation to the electron subsystem, the electron-phonon scattering, and energy absorption due to the electronic entropy effect. In

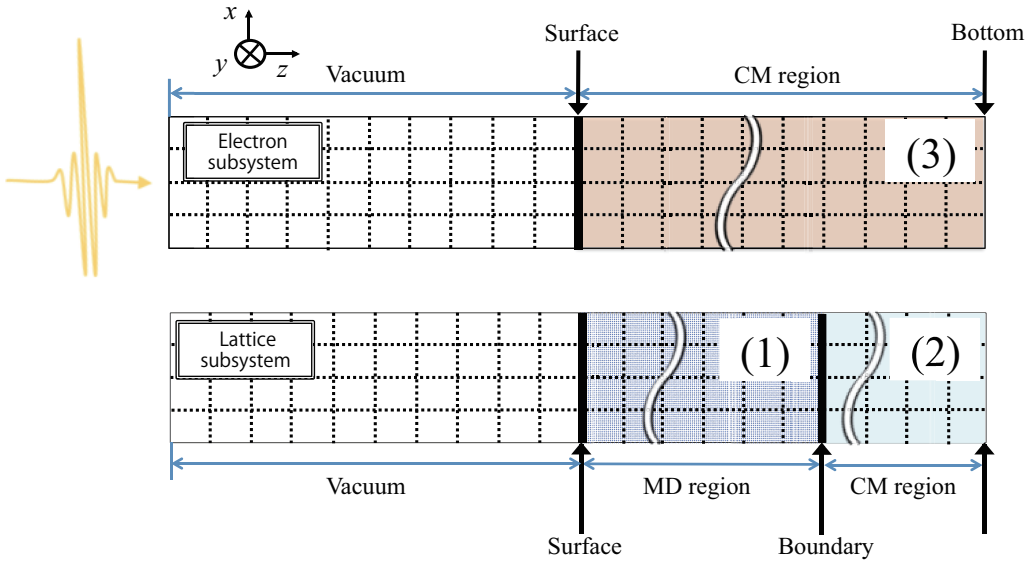

Figure 4.1: Schematic image of the TTM-MD calculation model. The laser comes from the left side of this figure. The local electronic temperature T_e^n and the local lattice temperature T_l^n are defined in n-th 3D cells (in dotted region). The periodic boundary conditions are used in x, y directions (parallel to the surface). A free boundary condition is used at the bottom of the MD region [region (1)]. In the MD region [(1) region], atomic dynamics is calculated using MD simulation. To reduce calculation cost, time development of T_l^n in a CM region [region (2)] is calculated using the CM. Time development of all T_e^n is calculated using the CM [region (3)].

other words, in the TTM-MD, atom dynamics are calculated based on the MD method, and at the same time, time development of the electronic subsystem is calculated by employing the TTM.

In our TTM-MD simulations, for reduction of calculation cost, the CM is also used to calculate time development of T_l in the deep inside of the Cu film [region (2) in Fig. 4.1]. Since we consider that atom dynamics in this region is not so important, we calculated only time development of T_e and T_l in this region. This region is called CM region and plays an important role for the thermal-dissipation of the energy deposited by laser irradiation. On the other hand, the region near the surface in which atoms exist is called MD region [region (1) in Fig. 4.1]. With the volume change due to the expansion or ablation, these regions change during simulation. In the lateral directions, which are parallel to the film surface, the periodic boundary is used. Boundary condition between the CM region and the MD region is the free boundary condition.

The local electronic temperature T_e^n and the local lattice temperature T_l^n are defined in three dimensional (3D) cells, where n is an index of the 3D cells. A region surrounded by the dotted lines in Fig. 4.1 represents the 3D cells. Although we refer to T_l^n as the local "lattice" temperature, we do not imply that the crystal structure is assumed. T_l^n represents not only the lattice temperature but also temperature of atoms. Besides, it is noted that T_l^n of the MD region represents the instantaneous temperature of atoms.

Time development of T_e^n is calculated by solving the following nonlinear differential equation:

$$C_e^n \frac{dT_e^n}{dt} = \nabla \cdot (\kappa_e^n \nabla T_e^n) - G^n (T_e^n - T_l^n) - \sum\nolimits_i^{N^n} \boldsymbol{v}_i \frac{\partial}{\partial \boldsymbol{r}_i} [S^n T_e^n] + I^n, \tag{4.1}$$

where $\boldsymbol{v}_i$ is the velocity of atom i. C_e^n is the electronic heat capacity, κ_e^n is the electronic thermal conductivity, G^n is the electron-phonon heat transfer constant, N^n is the number of atom in the n-th 3D cell, S^n is the electronic entropy, and I^n is the deposited energy by laser irradiation. These quantities are determined in each 3D cell by the following equations:

$$C_e^n = \frac{N^n}{N_0} C_e(T_e^n), \tag{4.2}$$

$$G^n = \frac{N^n}{N_0} G, \tag{4.3}$$

$$\kappa_e^n = \frac{N^n}{N_0} \kappa_e(T_e^n, T_l^n), \tag{4.4}$$

$$I^n = \frac{N^n}{N_0} I(T_e^n, T_l^n), \tag{4.5}$$

$$N_0 = \rho_0 V_c. \tag{4.6}$$

Here, ρ_0 is density of atoms in the equilibrium states and V_c is the volume of each 3D cell. Values of $C_e(T_e^n)$, G, $\kappa_e(T_e^n, T_l^n)$, and $I(T_e^n, T_l^n)$ are the same as those used in the CM simulation (Chap. 3). The third term on the right side of Eq. (4.1) represents an absorption energy by the electronic entropy. Derivation of the Eq. (4.1) and the absorption energy are explained in the next subsection.

T_l^n in the CM region and in the MD region are calculated by solving Eqs. (4.7a) and (4.7b), respectively:

$$C_l^n \frac{\partial T_l^n}{\partial t} = G^n(T_e^n - T_l^n), \tag{4.7a}$$

$$T_l^n = \frac{1}{3k_B N^n} \sum_i^{N^n} (\boldsymbol{v}_i - \boldsymbol{v}_c^n)^2 . \tag{4.7b}$$

Here, $\boldsymbol{v}_c^n$ is the average velocity of atoms (center-of-mass velocity) in the n-th 3D cell, while $C_l^n = \frac{N^n}{N_0} C_l$ is the lattice heat capacity of the cell. Eqs. (4.1) and (4.7a) were solved by a finite difference method (FDM).

Atom dynamics in the MD region are calculated by solving the following equations:

$$\frac{d\boldsymbol{r}_i}{dt} = \boldsymbol{v}_i, \tag{4.8a}$$

$$m\frac{d\boldsymbol{v}_i^n}{dt} = -\frac{\partial F^n}{\partial \boldsymbol{r}_i} - m\xi^n \boldsymbol{v}_i^n. \tag{4.8b}$$

Here, m is the mass of an atom, F^n is the free energy, and ξ^n is a coefficient that represents the force coming from the electron-phonon scattering. The first term in the right hand side of Eq. (4.8b) represents the force coming from the derivative of the T_e-dependent free energy with respect to space. F^n is calculated by T_e-dependent IAP. Details of the T_e-dependent IAP are explained in Sec. 4.2.

To satisfy the law of conservation of energy between the electron subsystem and the lattice subsystem, the value of ξ^n is determined by

$$\xi^n = -\frac{G^n(T_e^n - T_l^n)}{\sum_i^{N^n} m\boldsymbol{v}_i^2}. \tag{4.9}$$

Derivation of this equation is explained in the following subsection. Eqs. (4.8a) and (4.8b) are integrated by the velocity Verlet algorithm.

Here, we explain calculation conditions. The lateral dimensions of each 3D cell is 3.615 nm × 3.615 nm, which is ten times the lattice constant of the conventional unit cell of fcc Cu. The initial MD and CM regions are about 361.5 nm and 638.5 nm, respectively. Hence, the thickness of computational Cu film is 1 μm. The total number of atoms in the computational cell is about 4.0×10^5. The surface of the film is (001) free surface of the fcc structures. Laser pulse shape is assumed to be the Gaussian. Pulse duration times of an ultrashort pulse laser and a ps-pulse laser are 100 fs and 200 ps, respectively. The size of the 3D cells is approximately 1 nm × 1 nm × 1 nm. Therefore, the space step Δx_{CM} is approximately 1 nm.

A value of the time step Δt is 10 as, which is the same as that of the CM simulation in Chap. 3. This value is much shorter than the time step for ordinary MD simulations. To reduce the calculation cost, the time step for MD calculation Δt_{MD} is set to $\Delta t_{\mathrm{MD}} = n_{\mathrm{MD}} \Delta t$, where

n_{MD} is an integer number. In Sec 4.3, we determine the suitable time step Δt_{MD} so that the law of conservation of energy is satisfied.

In our simulations, before irradiating a laser on the Cu film, the computational cell was relaxed using the Nosé-Hoover thermostat [106] at 300 K for 800 ps, where $\Delta t_{\mathrm{MD}} = 5$ fs was used.

4.1.2 Law of conservation of energy

TTM-MD simulations have been performed to investigate ultrafast phenomena caused by irradiation with an ultrashort pulse laser. Although the T_e-dependent IAP is used in some previous simulations [4,79,80], the law of conservation of energy is not satisfied in these simulation. Here, we show that our extended calculation scheme, which satisfies the law of conservation of energy.

First, to simplify the situation, the laser deposited energy and the energy flow among the 3D cells were neglected. In other words, we considered only an energy exchange between the electron subsystem and the lattice subsystem in a 3D cell. In this situation, the conserved energy of the 3D cells are the internal energy: $E^n + \sum_i^{N^n} \frac{1}{2} m v_i^2$.

Time derivative of the conserve energy can be calculated easily as

$$\begin{aligned}
&\frac{d}{dt}\left(E + \sum_i^N \frac{1}{2} m \boldsymbol{v}_i^2\right) \\
&= \frac{dT_e}{dt}\frac{\partial E}{\partial T_e} + \sum_i^N \frac{d\boldsymbol{r}_i}{dt}\frac{\partial}{\partial \boldsymbol{r}_i} E + \sum_i^N \boldsymbol{v}_i \left(m \frac{d\boldsymbol{v}_i}{dt}\right) \\
&= \frac{dT_e}{dt}\frac{\partial E}{\partial T_e} + \sum_i^N \boldsymbol{v}_i \frac{\partial}{\partial \boldsymbol{r}_i} E + \sum_i^N \boldsymbol{v}_i \left[-\frac{\partial}{\partial \boldsymbol{r}_i}[E - ST_e] - m\xi \boldsymbol{v}_i\right] \\
&= C_e \frac{dT_e}{dt} + \sum_i^N \boldsymbol{v}_i \frac{\partial}{\partial \boldsymbol{r}_i}[ST_e] - \sum_i^N m\xi \boldsymbol{v}_i^2.
\end{aligned} \tag{4.10}$$

Here, to simplify notations, the 3D cell index n is omitted. In the second equality, Eqs. (4.8a) and (4.8b) are used. In the third equality, the definition of the electronic heat capacity [Eq. (3.2)] is used. Since the time derivative of the conserved quantity is 0, the following equation can be derived:

$$C_e \frac{dT_e}{dt} = -\sum_i^N \boldsymbol{v}_i \frac{\partial}{\partial \boldsymbol{r}_i}[ST_e] + \sum_i^N m\xi \boldsymbol{v}_i^2. \tag{4.11}$$

The first term of the right side in this equation represents the absorbed energy due to the electronic entropy and the second term is the exchange energy due to the electron-phonon scattering.

Subsequently, we added the effect of the electronic thermal diffusion D_{tot}^n and laser deposited energy I_{tot}^n to this situation. The former effect can be expressed as

$$D_{\mathrm{tot}}^n = \int \nabla \cdot (\kappa_e^n \nabla T_e^n) dt, \tag{4.12}$$

and the latter effect is

$$I^n_{\rm tot} = \int I^n dt. \tag{4.13}$$

In this situation, the conserve energy in each 3D cells is $E^n + \sum_i^{N_n} \frac{1}{2} m v_i^2 - D^n_{\rm tot} - I^n_{\rm tot}$. Therefore, the time derivative of the conserve energy can be written as

$$\begin{aligned}
&\frac{d}{dt}\left(E^n + \sum_i^{N^n} \frac{1}{2} m \boldsymbol{v}_i^2 - D^n_{\rm tot} - I^n_{\rm tot} \right) \\
&\quad = C^n_e \frac{dT^n_e}{dt} + \sum_i^{N^n} \boldsymbol{v}_i \frac{\partial}{\partial \boldsymbol{r}_i} \left[S^n T^n_e \right] - \sum_i^{N^n} m \xi^n \boldsymbol{v}_i^2 - \frac{dD^n_{\rm tot}}{dt} - \frac{dI^n_{\rm tot}}{dt} \\
&\quad = C^n_e \frac{dT^n_e}{dt} + \sum_i^{N^n} \boldsymbol{v}_i \frac{\partial}{\partial \boldsymbol{r}_i} \left[S^n T^n_e \right] + G^n (T^n_e - T^n_l) - \nabla \cdot (\kappa^n_e \nabla T^n_e) - I^n.
\end{aligned} \tag{4.14}$$

In the first equality, Eq. (4.10) is used. In the second equality, we used Eqs. (4.12), (4.13), and

$$- \sum_i^{N^n} m \xi^n \boldsymbol{v}_i^2 = G^n (T^n_e - T^n_l). \tag{4.15}$$

This equation, which is same as Eq. (4.9), means the energy conservation between the electronic subsystem and the lattice subsystem via the electron-phonon scattering. Since the time derivative of the conserve energy is 0, Eq. (4.1) can be derived from Eq. (4.14).

Eq. (4.1)

$$C^n_e \frac{dT^n_e}{dt} = \nabla \cdot (\kappa^n_e \nabla T^n_e) - G^n (T^n_e - T^n_l) - \sum\nolimits_i^{N^n} \boldsymbol{v}_i \frac{\partial}{\partial \boldsymbol{r}_i} \left[S^n T^n_e \right] + I^n$$

In many previous studies [4, 79, 80], when force acting on the atoms is calculated, the T_e-dependence of the free energy and the energy exchange due to the electron-phonon scattering are considered. However, the absorbed energy due to the electronic entropy effect is ignored. It means that, in the conventional simulations, time development of T_e is calculated the following equation:

$$C^n_e \frac{dT^n_e}{dt} = \nabla \cdot (\kappa^n_e \nabla T^n_e) - G^n (T^n_e - T^n_l) + I^n. \tag{4.16}$$

Hence, energy that is used to move up the internal-energy surface is supplied from virtual electron thermal bath, which is not intended in these studies (see: Fig. 4.2), because the third term in the right hand side of Eq. (4.1) is ignored in the conventional TTM-MD simulations [see: Eq. (4.16)]. We think that these misconceptions come from misunderstanding of the origin of

the large repulsion force, which is discussed in Chap. 2. Therefore, these previous studies assume the undesired electronic thermal bath so that the law of conservation of energy is not satisfied. In this study, we extended the TTM-MD simulation scheme by adding the $-\sum_i^{N^n} \boldsymbol{v}_i \frac{\partial}{\partial \boldsymbol{r}_i} [S^n T_e^n]$ term to Eq. (4.16) so that we can carry out simulation maintaining the law of conservation of energy.

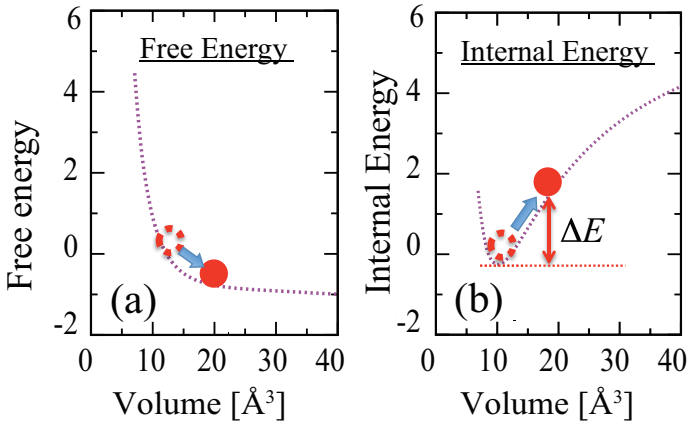

Figure 4.2: Schematic image of the energy absorbed by the electronic entropy. ΔE represents energy that should be absorbed from the electronic subsystem.

4.1.3 Computational detail

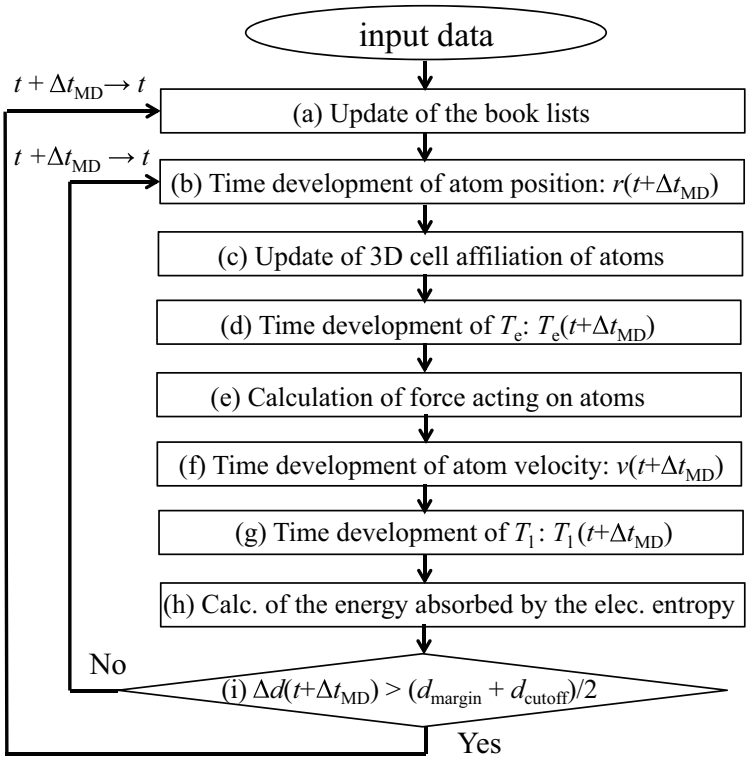

Figure 4.3: Flow chart of a main part of our developed code for TTM-MD calculations.

Here, we explain details of our calculation scheme and a flow of our developed code.

Figure 4.3 represents the main loop for calculation of $T_e^n(t)$, $T_l^n(t)$, and atom dynamics. To simplify this chart, lower important parts are omitted, such as the data input and output. To perform the parallelization calculation, the Message Passing Interface (MPI) and the Open Multi-Processing (OpenMP) are used as a communication library. As parallelization strategies, the domain decomposition and the bookkeeping methods are used.

(a) Update of the book lists

In the bookkeeping methods, atoms are assumed to be interact with registered atoms in each book list. When $\Delta d(t) > (d_{\mathrm{margin}}+d_{\mathrm{cutoff}})/2$ is satisfied, the book lists are updated at process (a) in Fig. 4.3. Here, the definition of $\Delta d(t)$ is the maximum value of $|\boldsymbol{r}_i(t)-\boldsymbol{r}_i(t_0)|$ among all atoms. $\boldsymbol{r}_i(t)$ is the position of the i-th atom at elapsed time t, and t_0 is a previous time at which book lists are updated. Margin distance d_{margin} is represented in Fig. 4.4. d_{margin} is set to the cutoff radius d_{cutoff} of the IAP.

When the book lists are updated, atoms only in a particular domain are considered. This method is called the domain decomposition method. In our simulation, atoms only in a gray domain in Fig. 4.5 are considered to update the book lists. z length of the buffer region is set to $d_{\mathrm{margin}} + d_{\mathrm{cutoff}}$.

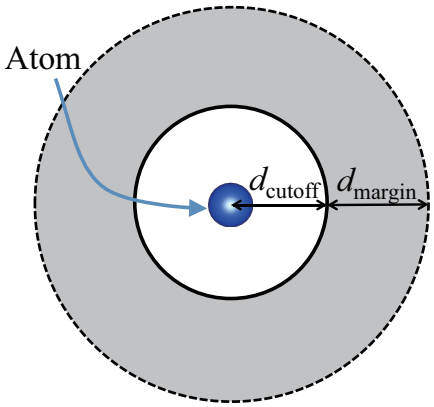

Figure 4.4: d_{cutoff} represents a cutoff radius of the inter atomic potential and d_{margin} represents margin distance of the focused atom (blue circle).

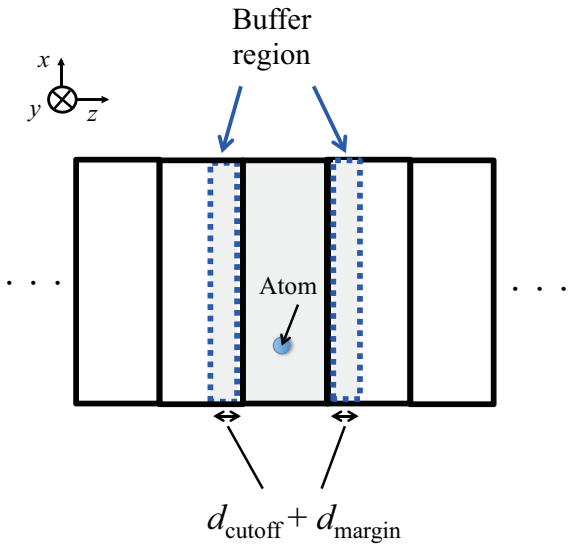

Figure 4.5: Schematic image of the domain decomposition method. When the book list for a blue atom is updated, atoms only in the grey domain are considered. The z length of the buffer region is set to $d_{\mathrm{cutoff}} + d_{\mathrm{margin}}$.

(b) Time development of $\boldsymbol{r}$

At process (b) in Fig. 4.3, time development of $\boldsymbol{r}_i$ is calculated. Using Eq. (4.8a), Eq. (4.8b), and the FDM, $\boldsymbol{r}_i^n(t + \Delta t_{\mathrm{MD}})$ are calcuated by solving the following equation:

$$\boldsymbol{r}_i^n(t + \Delta t_{\mathrm{MD}}) = \boldsymbol{r}_i^n(t) + \boldsymbol{v}_i^n(t)\Delta t_{\mathrm{MD}} + \frac{\Delta t_{\mathrm{MD}}}{2m}\left(-\frac{\partial F(t)}{\partial \boldsymbol{r}_i^n} - m\xi^n(t)\boldsymbol{r}_i^n(t)\right). \tag{4.17}$$

(c) Update of 3D cell affiliation of atoms

At process (c) in Fig. 4.3, 3D cell affiliation of atoms is updated. We assume that when the number of atoms in 3D cell is less than a threshold number N_{thr}, these cells are not contributed to the electronic thermal diffusion. We call a state of these cells inactive. On the other hands, a state of cells that contain more atoms than N_{thr} is called active. Figure 4.6 (a)-(d) represent some examples for classification of the active cells or the inactive cells.

To calculate the force acting on the atoms, which depends on T_e, we defined T_e at each atom. T_e of atoms filled by the same color are assumed to be the same, and they are assumed to belong to the same 3D cells. Atoms in the inactive cell are assumed to belong to the nearest active cell [1] among its six attached cells if these cells are active [Figs. 4.6(b) and (d)]. When the number of atoms in the inactive cell becomes larger than $N_{\rm thr}$, this cell becomes the the active cell and its T_e is averaged by T_e at each atom in this 3D cell [Fig. 4.6 (c)]. If a 3D cell is inactive and around its six attached cells are also inactive, atoms in the cell are independent from the electronic thermal diffusion, and T_e of atoms are not changed [Fig. 4.6 (e)]. Besides, if there is no atom within $d_{\rm cutoff}$ of the atom, this atom is considered to be independent from the thermal diffusion. In our simulation in Sec. 4.4, $N_{\rm thr}$ is set to $0.2 \times N_0$.

(d) Time development of T_e

At process (d) in Fig. 4.3, time development of T_e is calculated based on Eq. (4.1). Using the FDM and some assumptions, which are explained below, Eq. (4.1) can be written as

$$T_e^n(t+\Delta t) = T_e^n(t) + \frac{\Delta t}{C_e^n(t)} \left[\nabla \cdot (\kappa^n(t) \nabla T_e^n(t)) - G^n \left(T_e^n(t) - T_l^n(t') \right) - \sum_i^{N^n} \boldsymbol{v}_i(t') \cdot \frac{\partial}{\partial \boldsymbol{r}_i} \left[S^n(t') T_e^n(t') \right] + I^n(t) \right]. \tag{4.18}$$

To calculate $T_e^n(t+\Delta t_{\rm MD})$, we solve this equation $n_{\rm MD}$ times. During $n_{\rm MD}$ times calculation of $T_e^n(t+\Delta t)$, t' is assumed to be constant. It means that the values of T_e^n, I^n, and κ^n are changed at each time step, but the values of T_l^n, $\boldsymbol{v}_i$, and S^n does not change. As a boundary condition with respect to the vacuum region and the inactive cell, the Neumann boundary condition ($\nabla T_e = 0$) is used.

(e) Calculation of force acting on atoms

At process (e) in Fig. 4.3, force acting on atoms are calculated by using T_e^n, $\boldsymbol{r}_i$, and the T_e-dependent interatomic potential, whose details are explained in Sec 4.2.

[1] If there are two or more nearest active cells to an atom, the 3D cell to which the atom belongs is determined according to the following priority order:

$$\mathrm{C}_{-z} > \mathrm{C}_{+z} > \mathrm{C}_{-y} > \mathrm{C}_{+y} > \mathrm{C}_{-x} > \mathrm{C}_{+x},$$

where C_α represents each 3D cell attached to the focused inactive cell [see: Fig. 4.6(f)]. Here, α represents directions $(\pm x, \pm y, \pm z)$. Although this order has no physical meaning, we do not expect that this order qualitatively changes our simulation results since difference of T_e among these 3D cells is small ($< 10^2$ K), generally.

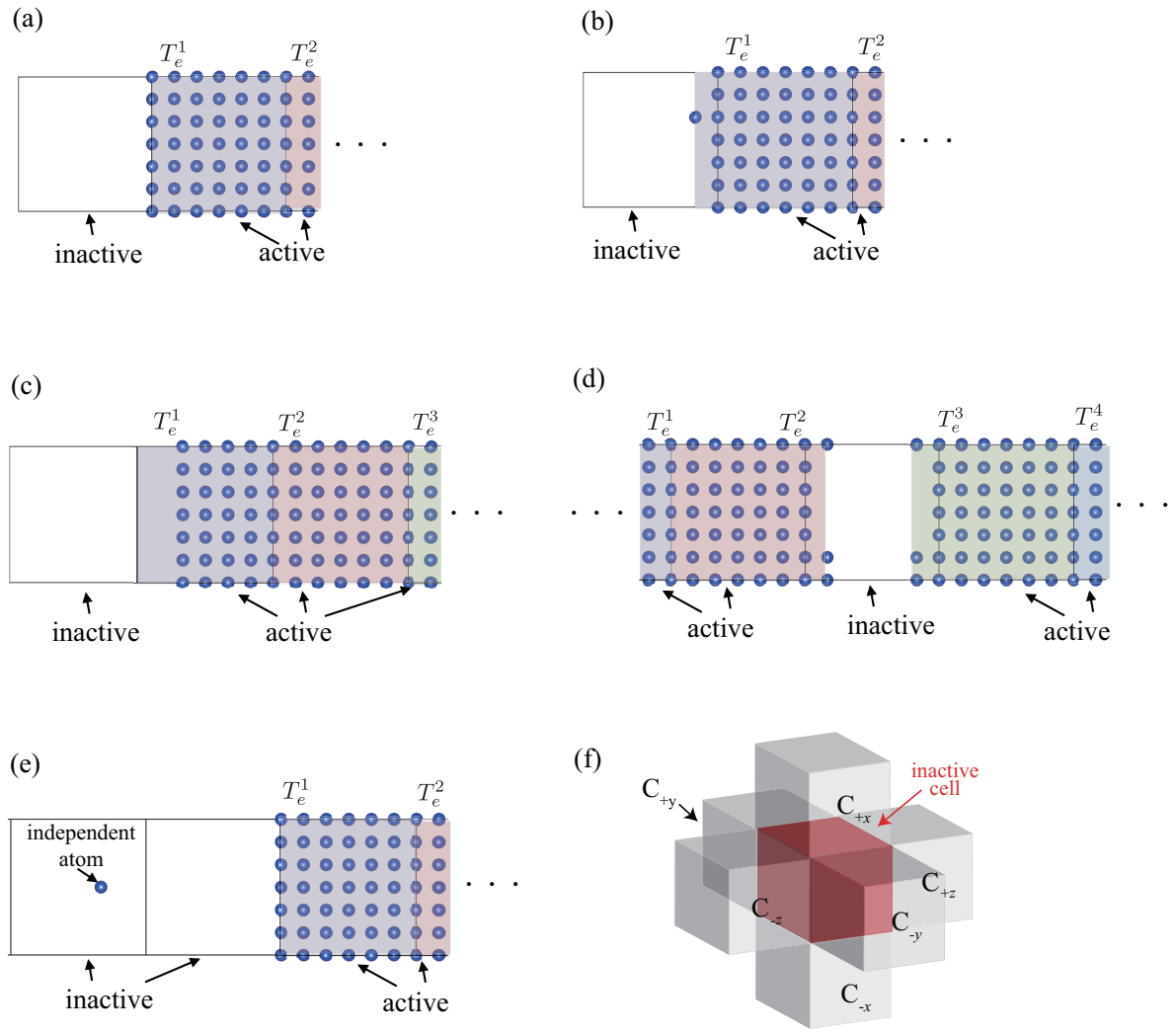

Figure 4.6: (a)-(e) represent some examples of 3D cell affiliation. T_e of atoms filled by same color is assumed to be same, and these atoms are assumed to belong to the same 3D cells. (f) represents a schematic image of C_α, which is the index of 3D cells attached to the focused inactive cell. Here, α represents directions $(\pm x, \pm y, \pm z)$.

(f) Time development of $\boldsymbol{v}$

At process (f) in Fig. 4.3, time development of $\boldsymbol{v}_i$ is calculated using Eq. (4.8b) and the FDM. According to the velocity Verlet algorithm, Eq. (4.8b) can be approximated as

$$\begin{aligned}
\boldsymbol{v}_i^n(t+\Delta t_{\mathrm{MD}}) &= \boldsymbol{v}_i^n(t) + \frac{d}{dt}\boldsymbol{v}_i^n(t)\Delta t_{\mathrm{MD}} + \frac{1}{2}\frac{d^2}{dt^2}\boldsymbol{v}_i^n(t)(\Delta t_{\mathrm{MD}})^2 \\
&= \boldsymbol{v}_i^n(t) + \frac{d}{dt}\boldsymbol{v}_i^n(t)\Delta t_{\mathrm{MD}} + \frac{1}{2}\frac{d}{dt}\left[\boldsymbol{v}_i^n(t+\Delta t_{\mathrm{MD}}) - \boldsymbol{v}_i^n(t)\right]\Delta t_{\mathrm{MD}} \\
&= \boldsymbol{v}_i^n(t) + \frac{1}{2}\frac{d}{dt}\left[\boldsymbol{v}_i^n(t+\Delta t_{\mathrm{MD}}) + \boldsymbol{v}_i^n(t)\right]\Delta t_{\mathrm{MD}} \\
&= \boldsymbol{v}_i^n(t) + \frac{1}{2m}\Big[-\frac{\partial F^n(t+\Delta t_{\mathrm{MD}})}{\partial \boldsymbol{r}_{\boldsymbol{i}}^{\boldsymbol{n}}} - m\xi^n(t+\Delta t_{\mathrm{MD}})\boldsymbol{v}_i^n(t+\Delta t_{\mathrm{MD}}) \\
&\qquad - \frac{\partial F^n(t)}{\partial \boldsymbol{r}_{\boldsymbol{i}}^{\boldsymbol{n}}} - m\xi^n(t)\boldsymbol{v}_i^n(t)\Big]\Delta t_{\mathrm{MD}}.
\end{aligned} \tag{4.19}$$

Since the length of time steps is different between Δt and Δt_{MD}, Eq. (4.15) should be changed to conserve energy between the electron subsystem and the lattice subsystem. According to Eq. (4.18), the exchange energy $E^n_{\text{el-ph}}$ due to the electron-phonon scattering during Δt_{MD} can be written as

$$\Delta E^n_{\text{el-ph}}(t+\Delta t_{\mathrm{MD}}) = \Delta t \sum_{s=0}^{n_{\mathrm{MD}}-1} G^n\{T_e^n(t+s\times\Delta t) - T_l^n(t)\}. \tag{4.20}$$

To satisfy the law of conserve of energy,

$$-\sum_i^{N^n} m\xi^n(t+\Delta t_{\mathrm{MD}})\left(\boldsymbol{v}_i^n(t+\Delta t_{\mathrm{MD}})\right)^2 \times \Delta t_{\mathrm{MD}} = \Delta E^n_{\text{el-ph}}(t+\Delta t_{\mathrm{MD}}) \tag{4.21}$$

should be satisfied. Therefore, values of the ξ^n are determined by the following equation:

$$\xi^n(t) = -\frac{\Delta E^n_{\text{el-ph}}(t)}{m\sum_i^{N^n}\{\boldsymbol{v}_i^n(t)\}^2\Delta t_{\mathrm{MD}}}. \tag{4.22}$$

By using this equation and Eq. (4.19), we can obtain

$$\begin{aligned}
\boldsymbol{v}_i^n(t+\Delta t_{\mathrm{MD}}) = \boldsymbol{v}_i^n(t) &- \frac{\Delta t_{\mathrm{MD}}}{2m}\left[\frac{\partial F^n(t+\Delta t_{\mathrm{MD}})}{\partial \boldsymbol{r}_{\boldsymbol{i}}^{\boldsymbol{n}}} + \frac{\partial F^n(t)}{\partial \boldsymbol{r}_{\boldsymbol{i}}^{\boldsymbol{n}}}\right] \\
&+ \frac{1}{2m}\left[\frac{\Delta E^n_{\text{el-ph}}(t+\Delta t_{\mathrm{MD}})\boldsymbol{v}_i^n(t+\Delta t_{\mathrm{MD}})}{\sum_i^{N^n}\{\boldsymbol{v}_i^n(t+\Delta t_{\mathrm{MD}})\}^2} + \frac{\Delta E^n_{\text{el-ph}}(t)\boldsymbol{v}_i^n(t)}{\sum_i^{N^n}\{\boldsymbol{v}_i^n(t)\}^2}\right].
\end{aligned} \tag{4.23}$$

The forth term of right hand can not be calculated, directly, because $\sum_i^{N^n}\{v_i^n(t+\Delta t_{\mathrm{MD}})\}^2$ is not obtained, . On the basis of the law of conservation of energy in each 3D cell, $\sum_i^{N^n}\{\boldsymbol{v}_i^n(t+\Delta t_{\mathrm{MD}})\}^2$

is calculated by the following equation:

$$\sum_i^{N^n}\{\boldsymbol{v}_i^n(t+\Delta t_{\mathrm{MD}})\}^2 = \frac{2}{m}\left[E^n(t)+\frac{m}{2}\sum_i^{N^n}\{\boldsymbol{v}_i^n(t)\}^2-\{E^n(t+\Delta t_{\mathrm{MD}})-D_{\mathrm{out}}^n(t+\Delta t_{\mathrm{MD}})\}\right], \quad (4.24)$$

where D_{out}^n represents energy coming from other cells. Hence, replacing the forth term Eq. (4.23) by Eq. (4.24), a following equation can be derived:

$$\boldsymbol{v}_i^n(t+\Delta t_{\mathrm{MD}}) = \frac{\boldsymbol{v}_i^n(t)-\frac{1}{2m}\left[\frac{\partial F^n(t+\Delta t_{\mathrm{MD}})}{\partial \boldsymbol{r}_i^n}+\frac{\partial F^n(t)}{\partial \boldsymbol{r}_i^n}-\frac{\Delta E_{\text{el-ph}}^n(t)\boldsymbol{v}_i^n(t)}{\sum_i^{N^n}\{\boldsymbol{v}_i^n(t)\}^2\Delta t_{\mathrm{MD}}}\right]\Delta t_{\mathrm{MD}}}{1-\frac{\Delta E_{\text{el-ph}}^n(t+\Delta t_{\mathrm{MD}})}{4\left[E^n(t)+\frac{m}{2}\sum_i^{N^n}\{\boldsymbol{v}_i^n(t)\}^2-\{E^n(t+\Delta t_{\mathrm{MD}})-D_{\mathrm{out}}^n(t+\Delta t_{\mathrm{MD}})\}\right]}}. \quad (4.25)$$

In our simulation, Eq. (4.25) is used to calculate $\boldsymbol{v}_i^n(t+\Delta t_{\mathrm{MD}})$.

(g) Time development of T_l

At process (g) in Fig. 4.3, time development of T_l is calculated based on Eqs. (4.7b) and (4.7a). T_l in the MD region is calculated by solving Eq. (4.7b). On the other hand, based on Eqs. (4.7a) and (4.20), the T_l in the CM region is calculated by solving the following equation:

$$T_l^n(t+\Delta t_{\mathrm{MD}}) = T_l^n(t)+\frac{\Delta E_{\text{el-ph}}^n(t+\Delta t_{\mathrm{MD}})}{C_l^n}. \quad (4.26)$$

(h) Calculation of the energy absorbed by the electronic entropy

At process (h) in Fig. 4.3, the energy absorbed by the electronic entropic term $-\sum_i^{N^n}\boldsymbol{v}_i(t+\Delta t_{\mathrm{MD}})\left[S^n(t+\Delta t_{\mathrm{MD}})T_e^n(t+\Delta t_{\mathrm{MD}})\right]$ is calculated.

4.2 Electronic-temperature-dependent interatomic potential (T_e-dependent IAP)

Since at least more than 100 nm depth and time of over 50 ps are necessary to perform simulations of the ablation [28], this simulation is too large and too long for first-principles calculations. Therefore, we use the classic MD method to calculate the force acting on atoms.

In this section, firstly, the conventional interatomic potential (IAP) and our developed T_e-dependent IAP are explained. Subsequently, we show a strategy to make the T_e-dependent IAP and the flow of it. Finally, the validity of the IAP is discussed by comparing IAP calculation results with calculation results based on the FTDFT.

4.2.1 Basic idea

Embedded atom method (EAM) potential

We start from briefly reviewing the conventional EAM potential at $T_e = 0\,\mathrm{K}$.

EAM potential [107] is a simple empirical many-body potential for metals. In this potential, the total energy of a system E_{tot} is expressed as

$$E_{\mathrm{tot}} = E_{\mathrm{two}} + E_{\mathrm{emb}}. \tag{4.27}$$

Here, E_{two} is the two-body potential, and E_{emb} is the many-body potential, so-called the embedded potential. E_{two} is the repulsive part of potential energy, and E_{emb} is the attractive part since it represents the cohesive energy. Generally, E_{two} is written as

$$E_{\mathrm{two}} = \frac{1}{2}\sum_{i}^{N}\sum_{j\neq i}^{N} V(r_{ij}), \tag{4.28}$$

where i and j are atom indices, r_{ij} represents distance between the i-th and the j-th atoms, V is the pair function, and N is the total number of atoms. Finnis and Sinnclair [108] proposed the following form as the function from of E_{emb}:

$$E_{\mathrm{emb}} = -A\sum_{i}^{N}\sqrt{\rho_i}. \tag{4.29}$$

Here, A is a fitting parameter and

$$\rho_i = \sum_{j\neq i}^{N}\phi(r_{ij}), \tag{4.30}$$

where the function $\phi(r_{ij})$ is the pair potential and depends on only r_{ij}. ρ_i represents the host electron density at the i-th atom created by its surrounding atoms.

From here, we derive Eqs. (4.29) and (4.30) under the rectangular model. The electronic states at the i-th atom are expected to be described by the local density of states $d_i(E)$. The band energy E_i^{band} of the i-th atom can be expressed as [109]

$$E_i^{\mathrm{band}} = 2\int_{-\infty}^{\infty} f(E)(E - E_i^c)d_i(E)dE. \tag{4.31}$$

Here, E_i^c is the center energy of $d_i(E)$ and $f(E)$ is the Fermi-Dirac distribution. In the case of $T_e = 0$, this equation can be written as

$$E_i^{\mathrm{band}} = 2\int_{-\infty}^{E_F} (E - E_i^c)d_i(E)dE, \tag{4.32}$$

where E_F is the Fermi energy. Under the rectangular model, $d_i(E)$ can be written as

$$d_i(E) = \begin{cases} \frac{2N^a}{W_i} & \cdots E_i^c - \frac{W_i}{2} < E < E_i^c + \frac{W_i}{2} \\ 0 & \cdots \quad \text{the others,} \end{cases} \tag{4.33}$$

where N^a is the number of the electron states and W_i represents the band width. In this model, Eq. (4.32) is calculated as

$$\begin{aligned} E_i^{\text{band}} &= \frac{2N^a}{W_i} \int_{E_i^c - W_i/2}^{E_F} (E - E_i^c) dE \\ &= \frac{N^a}{W_i} \left[(E_F - E_i^c)^2 - \left(\frac{W_i}{2} \right)^2 \right]. \end{aligned} \tag{4.34}$$

Using the number of the electrons N_i^e at the i-th atom, the following equation can be derived:

$$E_F - E_i^c = \frac{W_i}{2} \left(\frac{N_i^e}{N^a} - 1 \right). \tag{4.35}$$

By using this equation, Eq. (4.34) can be expressed as

$$E_i^{\text{band}} = \frac{N_i^e}{2} \left(\frac{N_i^e}{2N^a} - 1 \right) W_i. \tag{4.36}$$

If we assume that the number of electrons at the i-th atom is conserved, which is a physically reasonable in metals, N_i^e is a constant value. N^a is also a constant value so that the following relation can be derived:

$$E_i^{\text{band}} \propto W_i. \tag{4.37}$$

The second moment $\mu_i^{(2)}$ can be calculated as following

$$\begin{aligned} \mu_i^{(2)} &= \frac{2N^a}{W_i} \int_{E_i^c - \frac{W_i}{2}}^{E_F} (E - E_i^c)^2 dE \\ &= \frac{1}{12} W_i^2 \left(\left(\frac{N_i^e}{N^a} - 1 \right)^3 + 1 \right) \\ &\propto W_i^2. \end{aligned} \tag{4.38}$$

In the second equality, Eq. (4.35) is used. $\mu_i^{(2)}$ is a summation of the square of the transfer energy $t(r_{ij})$ between atomic orbital of the i-th and the j-th atoms, so that $\mu_i^{(2)}$ can be expressed as the function of r_{ij}. Combined with Eq. (4.30), $\mu_i^{(2)}$ can be written as

$$\mu_i^{(2)} \propto \rho_i \propto \sum_{j \neq i}^{N} \phi(r_{ij}). \tag{4.39}$$

By using Eqs. (4.37), (4.38), and (4.39), we obtain the following relation:

$$E_i^{\text{band}} \propto W_i \propto \sqrt{\mu_i^{(2)}} \propto \sqrt{\rho_i} \propto \sqrt{\left(\sum_{j\neq i}^{N} \phi(r_{ij})\right)}. \tag{4.40}$$

Based on this consideration, Eqs. (4.29) and (4.30) are certified in the case of the rectangular model.

Extension to finite T_e

Although a rigid formalism has not been established yet, some function forms of T_e-dependent IAP have been proposed [19,20,81]. For example, a complex function form [81] for solid tungsten (W) was proposed by Khakshouri *et al*. They assumed that the DOS of *s*-*p* band above *d* band is the same as that of *d* band, and the DOS of the *s*-*p* band continue to the infinity. Owing to this simplification, they obtained an exact solution of the T_e-dependent IAP form. In our study, we do not use their T_e-dependent potential because this potential is expected to be applied only to the structures near equilibrium volume. To make the T_e-dependent IAP that can be applied to the condensed state and the atomic state, we carried out the following simple consideration.

As a function form of the T_e-dependent IAP, we use the following function

$$F_{\text{tot}}(T_e) = E_{\text{tot}}(T_e) - S_{\text{tot}}(T_e)T_e, \tag{4.41}$$

where $F_{\text{tot}}(T_e)$ and $S_{\text{tot}}(T_e)$ are the total free energy of the system and the total electronic entropy of the system, respectively. We express $E_{\text{tot}}(T_e)$ and $S_{\text{tot}}(T_e)$ as the following equations:

$$E_{\text{tot}}(T_e) = E_{\text{two}}(T_e) + E_{\text{emb}}(T_e), \tag{4.42}$$

$$S_{\text{tot}}(T_e) = S_{\text{emb}}(T_e). \tag{4.43}$$

Here, $E_{\text{two}}(T_e)$ is the two-body potential and $E_{\text{emb}}(T_e)$ and $S_{\text{emb}}(T_e)$ are the embedded potential. We assume that $S(T_e)$ can be expressed by the embedded potential form because $S(T_e)$ is a function of the electronic states [see: Eq. (2.11)].

Figure 4.7 represents a schematic image of our consideration to determine the function form of $E_{\text{emb}}(T_e)$. In this consideration, the rectangular model is used. In addition, we assume the high T_e limit ($k_B T_e \gg W_i$). Using the first-order Taylor expansion, $f(E)$ can be approximated as

$$f(E) \cong \frac{1}{2} - \frac{1}{4k_B T_e}(E-\mu). \tag{4.44}$$

Using Eq. (4.31), the following relation can be derived:

$$\begin{aligned} E_i^{\text{band}} &\cong \frac{2N^a}{W_i}\int_{E_i^c-\frac{1}{2}W_i}^{E_i^c+\frac{1}{2}W_i}\left[\frac{1}{2}-\frac{1}{4k_BT_e}(E-\mu)\right](E-E_i^c)dE \\ &\quad -\frac{2N^a}{W_i}\int_{E_i^c-\frac{1}{2}W_i}^{E_i^c+\frac{1}{2}W_i}\left[\frac{1}{2}-\frac{1}{4k_BT_e}(E-\mu)\right](E-E_i^c)\delta(E-\mu)dE \\ &\propto W_i^2. \end{aligned} \tag{4.45}$$

This relation indicates that if Eq. (4.38) is satisfied at high T_e, $E_{\text{emb}}(T_e)$ can be written as a function of W_i^2. By using Eqs. (4.38), (4.39), and (4.45), we can express $E_{\text{emb}}(T_e)$ as

$$\begin{aligned} E_{\text{emb}}(T_e) &= \alpha_1(T_e)\sum_i^N W_i(T_e) + \alpha_2(T_e)\sum_i^N W_i^2(T_e) \\ &= a_1(T_e)\sum_i^N \rho_i(T_e) + a_2(T_e)\sum_i^N \rho_i^2(T_e). \end{aligned} \tag{4.46}$$

Here, $\alpha_1(T_e), \alpha_2(T_e), a_1(T_e)$ and $a_2(T_e)$ are the fitting parameters.

Subsequently, we determine the function form of $S_{\text{emb}}(T_e)$. The electronic entropy of the i-th atom S_i can be written as

$$S_i = -2k_B\int_{-\infty}^{\infty}[f(E)\ln f(E) + (1-f(E))\ln(1-f(E))]d_i(E)dE. \tag{4.47}$$

Under the rectangular model and the high T_e limit, this equation can be expressed as

$$S_i = -2k_B\frac{N^a}{W_i}\int_{E_i^c-\frac{1}{2}W_i}^{E_i^c+\frac{1}{2}W_i}[f(E)\ln f(E) + (1-f(E))\ln(1-f(E))]dE. \tag{4.48}$$

Furthermore, by using the 2nd-order tailor expansion of the Fermi-Dirac distribution, this equation is rewritten as

$$S_i \cong -2k_B\frac{N^a}{W_i}\int_{E_i^c-\frac{1}{2}W_i}^{E_i^c+\frac{1}{2}W_i}\left[\ln 2 + \frac{1}{8(k_BT_e)^2}(E-\mu)^2\right]dE. \tag{4.49}$$

Using this equation, the electronic entropy of the atomic state S^{atom}, where the local DOS is expressed as the delta function, can be expressed as

$$S_i^{\text{atom}} \cong -2k_BN^a\left[\ln 2 + \frac{1}{8(k_BT_e)^2}(E_i^c-\mu)^2\right]. \tag{4.50}$$

Similarly, from Eq. (4.49), the electronic entropy of the condensed state S^{cond} is calculated as

$$S_i^{\text{cond}} \cong -2k_BN^a\left[\ln 2 + \frac{1}{8(k_BT_e)^2}(E_i^c-\mu)^2\right] + \frac{W_i^2}{48(k_BT_e)^2}. \tag{4.51}$$

Therefore, the following relation can be derived:

$$\begin{aligned} S_i^{\mathrm{cond}} - S_i^{\mathrm{atom}} &= \frac{W_i^2}{48(k_B T_e)^2} \\ &\propto W_i^2. \end{aligned} \tag{4.52}$$

Moreover, we assume $S_i^{\mathrm{band}} - S_i^{\mathrm{atom}} \propto W_i$ to increase the freedom of S_{emb}. As a result, we can express $S_{\mathrm{emb}}(T_e)$ as

$$\begin{aligned} S_{\mathrm{emb}}(T_e) &= \beta_1(T_e) \sum_i^N W_i(T_e) + \beta_2(T_e) \sum_i^N W_i(T_e)^2 \\ &= b_1(T_e) \sum_i^N \rho_i(T_e) + b_2(T_e) \sum_i^N \rho_i(T_e)^2, \end{aligned} \tag{4.53}$$

where Eqs. (4.38) and (4.39) are used in the second equality. $\beta_1(T_e), \beta_2(T_e), b_1(T_e)$ and $b_2(T_e)$ are the fitting parameters.

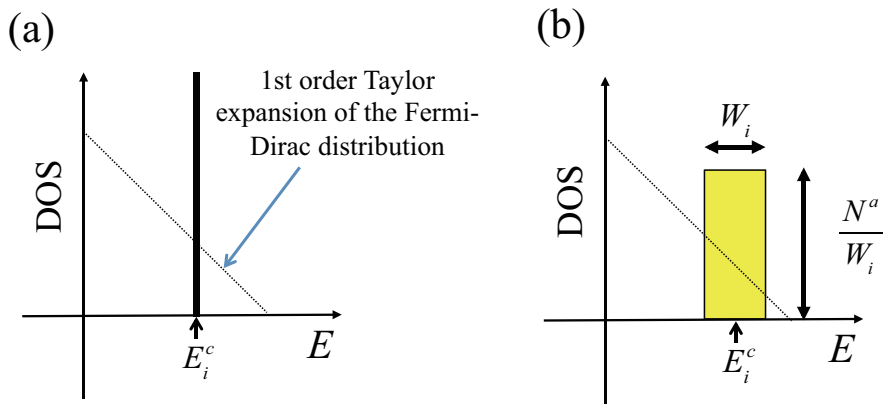

Figure 4.7: Schematic image of our consideration. Here, the rectangular model is used. (a) represents the local DOS of the atomic state, and (b) represents the local DOS of the condensed states.

Besides, we use a Dai potential [110] to describe the function form of $V(r)$ and $\phi(r)$. Consequently, we obtain the following T_e-dependent IAP.

$$F_{\mathrm{tot}}(T_e) = E_{\mathrm{tot}}(T_e) - S_{\mathrm{tot}}(T_e)T_e. \tag{4.54}$$

These value are represented as

$$E_{\mathrm{tot}}(T_e) = \frac{1}{2}\sum_{i}^{N}\sum_{j\neq i}^{N} V(r_{ij}) + a_0(T_e) + a_1(T_e)\sum_{i}^{N}\rho_i + a_2(T_e)\sum_{i}^{N}\rho_i^2, \tag{4.55}$$

$$S_{\mathrm{tot}}(T_e) = b_0(T_e) + b_1(T_e)\sum_{i}^{N}\rho_i + b_2(T_e)\sum_{i}^{N}\rho_i^2. \tag{4.56}$$

Here,

$$\rho_i = \sqrt{\sum_{j\neq i}^{N}\phi(r_{ij})}, \tag{4.57}$$

$$V(r) = \begin{cases} (r - c(T_e))^2 \left(c_0(T_e) + c_1(T_e)r + c_2(T_e)r^2 + c_3(T_e)r^3 + c_4(T_e)r^4\right) & \cdots r \leq c(T_e) \\ 0 & \cdots r > c(T_e), \end{cases} \tag{4.58}$$

$$\phi(r) = \begin{cases} (r - d(T_e))^2 + d_0^2(T_e)\,(r - d(T_e))^4 & \cdots r \leq d(T_e) \\ 0 & \cdots r > d(T_e). \end{cases} \tag{4.59}$$

Fitting parameters:

$$c(T_e), d(T_e), a_0(T_e), a_1(T_e), a_2(T_e), b_0(T_e), b_1(T_e), b_2(T_e),$$
$$c_0(T_e), c_1(T_e), c_2(T_e), c_3(T_e), c_4(T_e), d_0(T_e).$$

Here, $c(T_e)$ and $d(T_e)$ are the cutoff radius. $a_0(T_e)$ and $b_0(T_e)$ represent $E_{\mathrm{tot}}(T_e)$ and $S_{\mathrm{tot}}(T_e)$ of isolated atoms. Ideally, these values are differences between the values of $E_{\mathrm{tot}}(T_e)$ (or $S_{\mathrm{tot}}(T_e)$) of isolated atoms at high T_e and those of cold independent atoms. It means we assume that the excited atoms are emitted when non-thermal ablation occurs. This assumption is verified since the emission spectrum has been experimentally detected during ablation process [111].

4.2.2 Strategy to make the T_e-dependent IAP

Flow

Here, we explain the flow of making appropriate T_e-dependent IAP for our simulation. Figure 4.8 represents its flow chart. To obtain appropriate T_e-dependent IAP, we completed the following two processes: first one is a fitting process and the other is a selection process.

In the fitting process, parameter fitting of $E_{\rm tot}(T_e)$ and $F_{\rm tot}(T_e)$ are performed. In the selection process, we select the best IAP from candidate IAP, which are obtained through the fitting process.

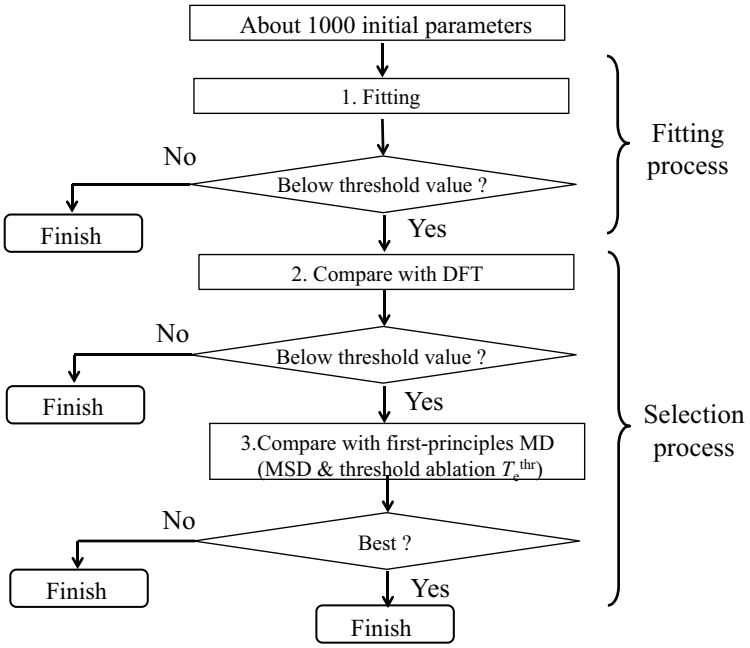

Figure 4.8: Flow chart of making the T_e-dependent IAP.

Fitting process

Here, we explain the fitting process. We performed parameter fitting of $E_{\rm tot}(T_e)$ and $F_{\rm tot}(T_e)$ at 300 K, and from $T_e = 5000$ to 50000 K with increment of 5000 K. Parameter values of the other T_e are estimated by a linear interpolation. A simple example of the interpolation is represented in Fig. 4.9. To obtain appropriate $E_{\rm tot}(T_e)$ and $F_{\rm tot}(T_e)$ for the interpolation, values of the fitting parameters should not be largely different from those near T_e. Accordingly, we follow the process in Fig. 4.10 to fit the parameters. This process is corresponding to "1. Fitting" in Fig. 4.8.

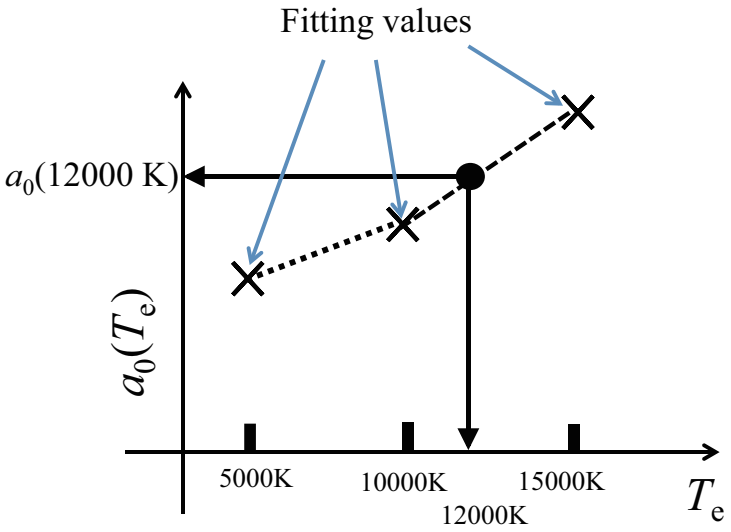

Figure 4.9: Example of the interpolated value of $a_0(12000\,\mathrm{K})$.

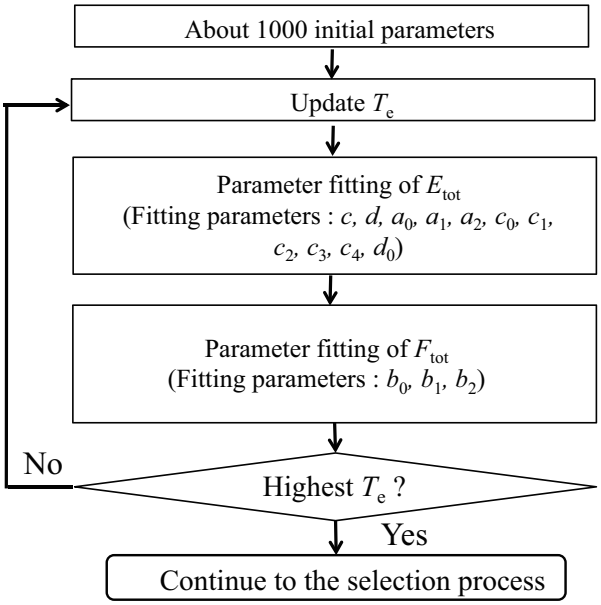

Figure 4.10: Flow chart for parameter fitting.

First, parameter fitting was started from $T_e = 300\,\mathrm{K}$. Since we want appropriate $F_{\mathrm{tot}}(T_e)$ and $E_{\mathrm{tot}}(T_e)$, parameter fitting of these values are carried out separately. At each T_e, parameter fitting of $E_{\mathrm{tot}}(T_e)$ are carried out before the fitting of $F_{\mathrm{tot}}(T_e)$. In other words, first, values of $c(T_e)$, $d(T_e)$, $a_0(T_e)$, $a_1(T_e)$, $a_2(T_e)$, $c_0(T_e)$, $c_1(T_e)$, $c_2(T_e)$, $c_3(T_e)$, $c_4(T_e)$, and $d_0(T_e)$ are determined. Next, parameter fitting of the other parameters $[b_0(T_e), b_1(T_e), b_2(T_e)]$ were carried out. In the fitting process of $F_{\mathrm{tot}}(T_e)$, the other parameters, such as $c(T_e)$ and $d(T_e)$, are fixed. Subsequently, we move on to parameter fitting of the next higher T_e. Then, the initial values of parameters were set to the values obtained through the previous parameter fitting. In this way, parameter fitting were performed until highest electronic temperature $T_e = 50000\,\mathrm{K}$. These parameter fittings are carried out about 1000 times from the different initial values.

Fitting data $[E_{\mathrm{tot}}(T_e)$ and $F_{\mathrm{tot}}(T_e)]$ are calculated using the VASP code [112–114] based on the FTDFT. The number of fitting data N_{fit} is 50 at each T_e, and these data consist of calculation results of the fcc structures, small displacement structure from the fcc structures, and structures created by first-principles MD simulation. The projector augmented wave (PAW) [115, 116] method and the generalized gradient approximation (GGA) with the Perdew-Burke-Ernzerhof (PBE) exchange-correlation functional were used in the calculations. The cohesive energy of PBE calculation is 3.68 eV, which is a little larger than the experimental value (3.49 eV [104,117]). The value of PBE is better than calculated values by PBEsol (4.26 eV) and by LDA (4.67 eV). The conserved energy is set to $1.0 \times 10^{-4}\,\mathrm{eV}$, and the occupation number of the highest energy band is less than 0.001. To adjust the value of the energy of an isolated atom limit E_{atom} at low T_e to 0, all values of $E(T_e)$ and $F(T_e)$ are subtracted by E_{atom}. The electronic structure calculations were performed with a cutoff energy of 480 eV for the plane-wave basis and the Brillouin-zone k-points sampling of a Monkhorst-Pack mesh with $8 \times 8 \times 8$ for the fcc structures and the small displacement structures. In addition, we performed the atom dynamics simulation at high T_e in a small system, where 108 atoms are contained. To represent the thin film ($\sim 10\,\mathrm{nm}$), the slab model is employed, and the lattice constants of the computational cell are fixed to $x = 10.845\,\text{Å}$, $y = 10.845\,\text{Å}$, and $z = 36.15\,\text{Å}$. The computational cell are represented in Fig. 4.11. The periodic boundary conditions are applied to all directions. Time step is 3 fs and k-points sampling is $4 \times 4 \times 1$. Before simulations were carried out at high T_e, atoms were thermalized using the Nosé-Hoover thermostat [106] at 300 K for more than 3 ps.

We used the root mean square error (RMSE) as the evaluation function of the parameter fitting. The definition of the RMSE is

$$\mathrm{RMSE} = \frac{1}{N_{\mathrm{fit}}} \sum_{q}^{N_{\mathrm{fit}}} \sqrt{\left(\frac{E_q^{\mathrm{FTDFT}}}{N_q^{\mathrm{atom}}}\right)^2 - \left(\frac{E_q^{\mathrm{IAP}}}{N_q^{\mathrm{atom}}}\right)^2}, \tag{4.60}$$

where E^{FTDFT} are the internal energy or the free energy of FTDFT calculations and E^{IAP} are these of IAP calculations. q is the index of the structures and N_q^{atom} is the number of atoms in the q-th structure. The non-linear mean square methods are used for parameter fitting. For solving the non-linear equations, the Gauss-Seidel method is used.

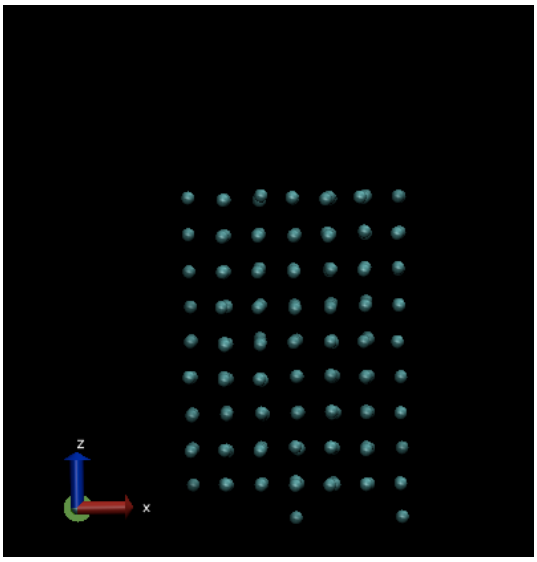

Figure 4.11: Computational cell used for MD calculation. This figure is visualized using Visual Molecular Dynamics (VMD) [118].

Selction process

In the fitting process, many IAP [$E_{\rm tot}(T_e)$ and $F_{\rm tot}(T_e)$] are obtained. In this process, we select the best IAP from these IAP for the simulation of ablation.

We considered the best IAP as the potential which can reproduces FTDFT results of the cohesive energy, the lattice constant, the bulk modulus, the phonon dispersion, the means square displacement (MSD), and the ablation threshold electronic temperature $T_e^{\rm thr}$, since these values are expected to be important for trustworthy simulation of the ablation. The definition of the MSD is

$$\mathrm{MSD} = \frac{1}{N^{\rm atom}} \sum_{i}^{N^{\rm atom}} (\boldsymbol{r}_i(t) - \boldsymbol{r}_i(0))^2, \tag{4.61}$$

where t is an elapsed time after T_e is increased.

The cohesive energy, the lattice, and the bulk modus are standard physical properties which should be reproduced by any IAP. The phonon dispersion represents the stability of structure and is related with the melting temperature, which are important to describe the spallation process. The MSD represents diffusion and expansion, and the phase, such as solid, liquid, and gas. The importance of $T_e^{\rm thr}$ is obvious since one of the purposes of our simulation is investigating the ablation threshold laser fluence.

The cohesive energy, the lattice constant, and the bulk modulus B are calculated by fitting

the EV curve to the following Murnaghan equation of state [119],

$$E(V) = E(V_0)\frac{BV}{B'(B'-1)}\left[B'\left(1-\frac{V_0}{V}\right)+\left(\frac{V_0}{V}\right)^{B'}-1\right]. \tag{4.62}$$

Here, V, V_0, and B' are volume, equilibrium volume, and a derivative of B with respect to pressure, respectively. If all the errors of these values are below 20 %, these IAP are considered as appropriate potential.

Calculation conditions for the phonon dispersion are following. Force calculations were performed using VASP code [112–114] and phonon calculations were conducted using ALAMODE package [120, 121]. The force constants is calculated using the frozen phonon method. The calculated cell is a $3 \times 3 \times 3$ supercell of the conventional unit cell of the fcc structure and k-points sampling are $3 \times 3 \times 3$. We consider that if the imaginary phonon does not exist and the error of the maximum frequency is less than $150\,\mathrm{cm}^{-1}$, these IAP are regarded as good potential. It is noted that this criterion is only applied to the phonon dispersion below T_e^{thr} since the importance of the phonon dispersion above T_e^{thr} is expected to be low.

To calculate the MSD and T_e^{thr}, we carried out MD simulations. Details of the MD simulation are the same as those explained in the fitting process. MD simulations were carried out three times from different initial configurations. If bottom atoms and surface atoms approach within the cutoff radius of the IAP, we consider that ablation is caused at this T_e. We consider that if error of T_e^{thr} is less than 2500 K, this IAP is appropriate. The MSD calculation results are used to determine the best IAP from all IAP that satisfies all criteria explained above.

4.2.3 Validity of the T_e-dependent IAP

Here, we analyze the validity of the obtained IAP by comparing IAP calculation results with FTDFT calculation results.

Fitting results

The RMS errors of the fitting results of the best IAP is shown in Fig. 4.12. Figure 4.12 represents that, at low T_e, this IAP can reproduce the FTDFT results with several 10 meV errors.

Volume dependence of E and F

Figure 4.13 shows the volume dependence of E and F. Horizontal axis indicates the rate of the lattice constant scaling the equilibrium lattice constant at $T_e = 300$ K. Plus and cross marks represent FTDFT results of E and F, respectively. Solid and dotted lines represent IAP results

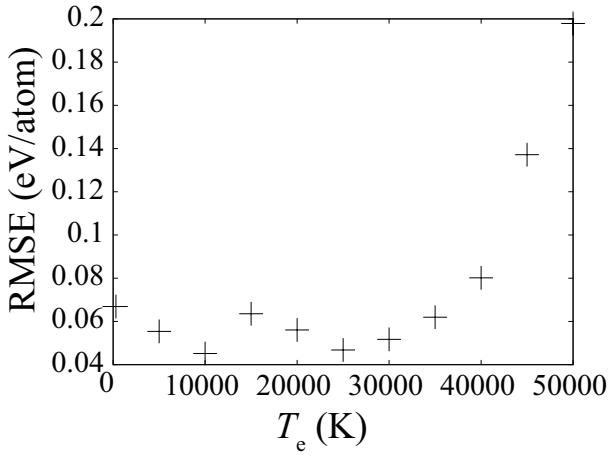

Figure 4.12: The RMS errors of the fitting results of the best IAP. Values of RMSE are per atom.

of E and F, respectively. Figure 4.13 shows that IAP calculation results agree with FTDFT calculation results.

Results of the cohesive energy, the lattice constant, and the bulk modulus at $T_e = 300\,\mathrm{K}$ are summarized in Table 4.1. The result of IAP calculations overestimates the value of the bulk modulus, but the values of the lattice constant and the cohesive energy are very close to the value of the experiment, though accidentally.

Table 4.1: Values of the lattice constant, the cohesive energy, and the bulk modulus at $T_e = 300\,\mathrm{K}$.

	IAP	FTDFT	Exp.
Lattice constant (Å)	3.613	3.634	3.615 [76]
Cohesive energy (eV)	3.52	3.68	3.49 [104]
Bulk modulus (GPa)	164.6	137.6	142 [122]

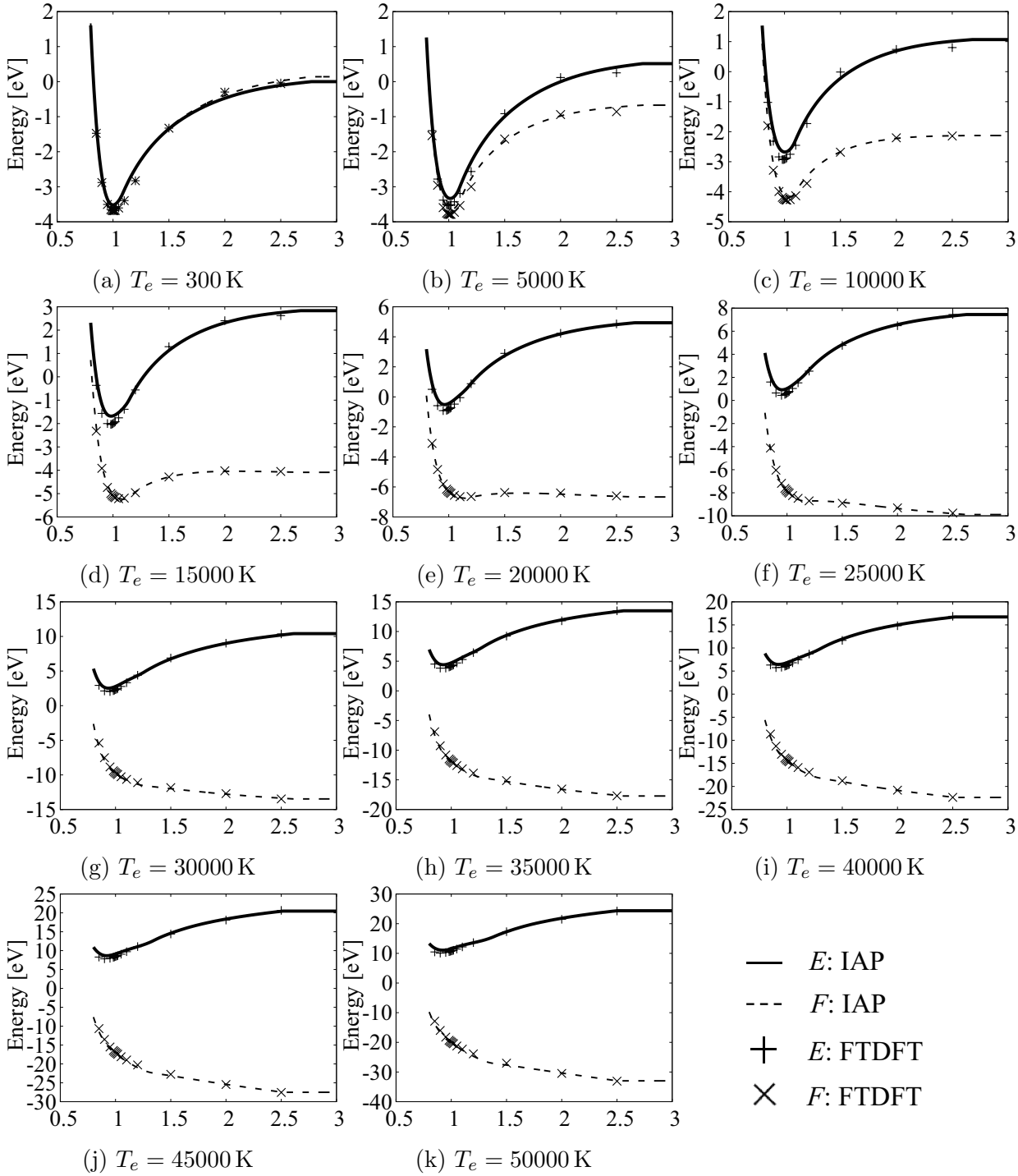

Figure 4.13: Volume dependence of E and F. Each horizontal axis indicates the rate of the lattice constant scaling the equilibrium lattice constant at $T_e = 300\,\mathrm{K}$. Plus and cross marks represent the FTDFT results of E and F, respectively. Solid and dashed lines represent IAP calculation results of E and F, respectively.

Phonon dispersion

Figure 4.14 shows the T_e-dependent phonon dispersion by (a) FTDFT calculations and (b) IAP calculations. The IAP calculation results overestimate phonon frequency by $\sim 30\,\%$, but the imaginary phonon does not exist. Therefore, in our IAP simulations, structure change would not be caused at low T_l.

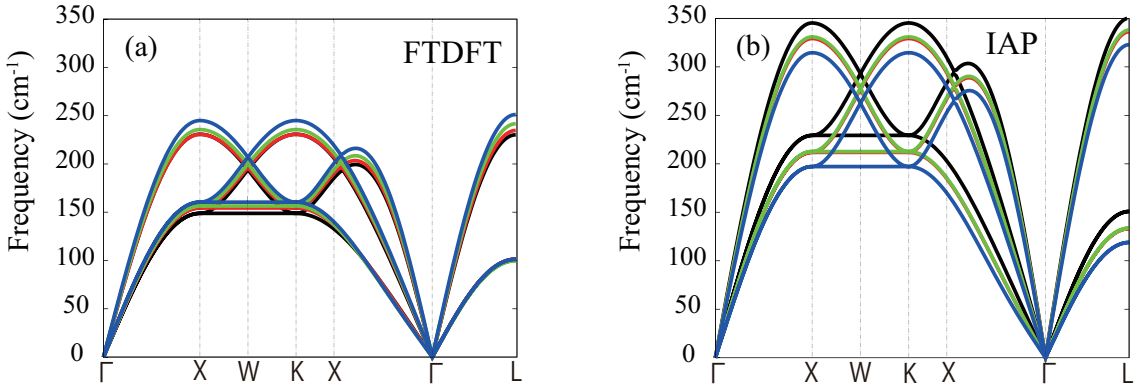

Figure 4.14: Calculation results of phonon dispersion of (a) FTDFT calculations and (b) IAP calculations. Black, red, green, and blue lines represent calculation results at T_e = 300, 5000, 10000, and 15000 K, respectively. Each high symmetry point represents Γ = [0, 0, 0], X = [1/2, 0, 1/2], W = [1/2, 1/4, 3/4], K = [1/2, 1/2, 1], and L = [1/2, 1/2, 1/2].

Mean square displacement (MSD)

Figure 4.15 shows calculation results of the MSD. Figure 4.15(a) represents FTDFT calculation results, and Fig. 4.15 (b) represents IAP calculation results. Solid, dashed, dotted, chain, and bold lines represent results at T_e = 300, 10000, 15000, 17500, and 20000 K, respectively. At low T_e, the vibration period of IAP is shorter than that of FTDFT. This difference is consistent with the large phonon frequency (Fig. 4.14) and with the large value of the bulk modulus (Table 4.1). At $T_e \geq 17500$ K, vibration is not observed. It represents that ablation occurs above $T_e = 17500$ K. Although there are some differences between FTDFT and IAP results, the T_e-dependence of these MSD is consistent, qualitatively. It should be noted that we do not carry out parameter fitting at $T_e = 17500$ K, and these values were obtained by the linear interpolation. This result exhibits the accuracy of the interpolated IAP.

Ablation threshold electronic temperature: T_e^{thr}

Table 4.2 represents the comparison of T_e^{thr} between FTDFT and IAP calculations. These numbers represent the number of times that ablation occurs at each T_e. Total trial number is

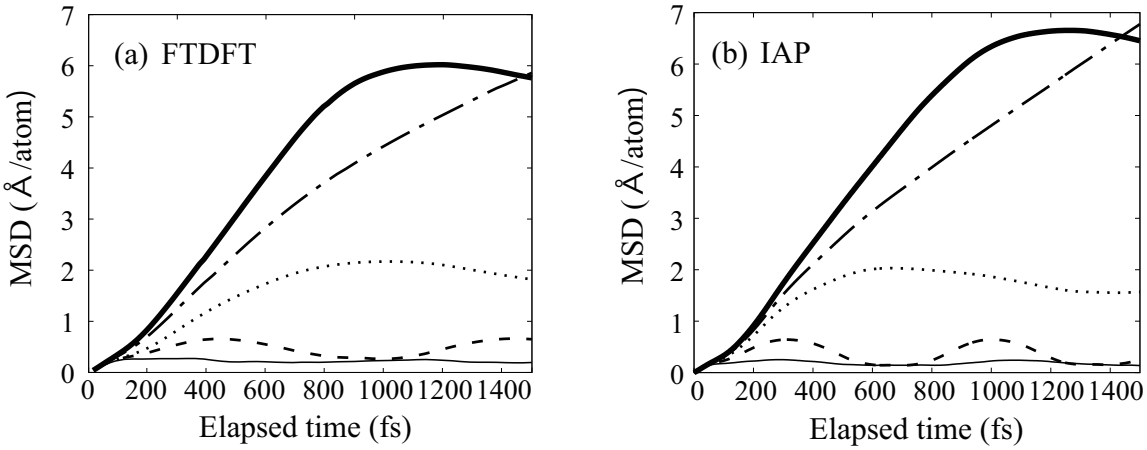

Figure 4.15: MSD calculation results of (a) FTDFT calculations and (b) IAP calculations. Solid, dashed, dotted, chain, and bold lines represent $T_e = 300$, 10000, 15000, 17500, and 20000 K, respectively.

three. From Table 4.2, we find that the discrepancy of $T_e^{\rm thr}$ between IAP results and FTDFT results is less than 500 K.

Figure 4.16 shows snapshots of MD simulations of the small film system at 900 fs after T_e changed to each high T_e. Each figure represents the snapshots at (a), (b) $T_e = 15000$ K, (c), (d) $T_e = 17500$ K, and (e), (f) $T_e = 20000$ K. The left figures [(a), (c), (e)] are results of first-principles MD calculations based on FTDFT, and the right figures [(b), (d), (f)] are results of classical MD calculations using the IAP. These figures are visualized by using Visual Molecular Dynamics (VMD) [118].

Figure 4.16(d) shows that, cluster-like material, which is indicated by the red arrow, is emitted in the IAP calculation at $T_e = 15000$ K. On the other hand, Fig. 4.16 (c) shows that atomic-like materials are emitted material in the FTDFT calculation at $T_e = 15000$ K.

Table 4.2: Calculation results for $T_e^{\rm thr}$. The number represents the number of times that ablation occurs at each T_e. Total trial number is three.

	15000 K	15500 K	16000 K	16500 K	17000 K	17500 K
IAP	0	0	0	0	2	3
FTDFT	0	0	0	0	3	3

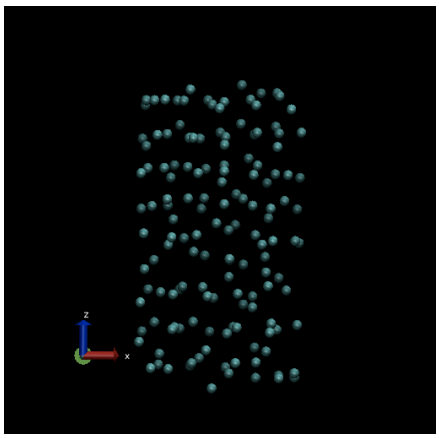

(a) FTDFT, $T_e = 15000\,\mathrm{K}$

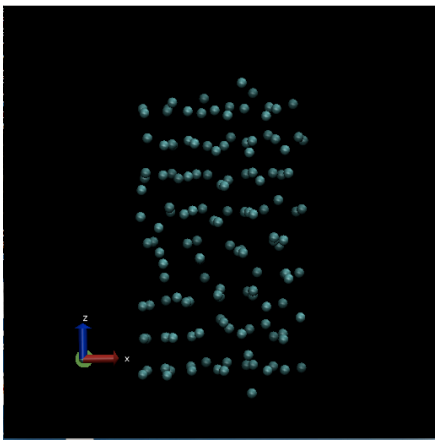

(b) IAP, $T_e = 15000\,\mathrm{K}$

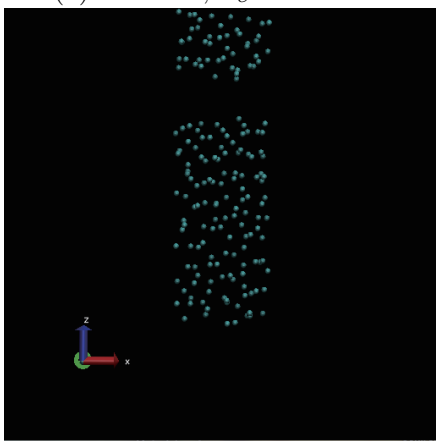

(c) FTDFT, $T_e = 17500\,\mathrm{K}$

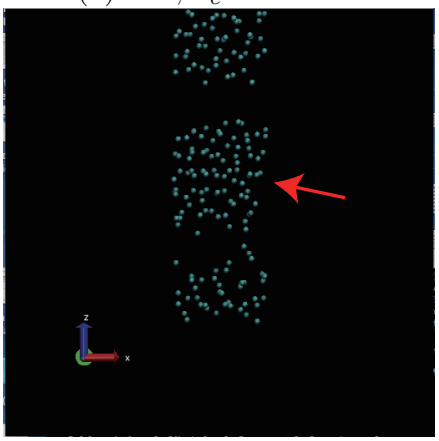

(d) IAP, $T_e = 17500\,\mathrm{K}$

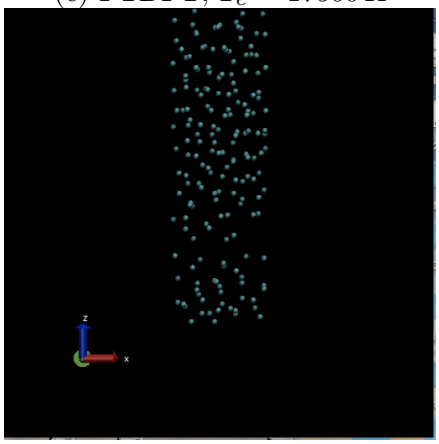

(e) FTDFT, $T_e = 20000\,\mathrm{K}$

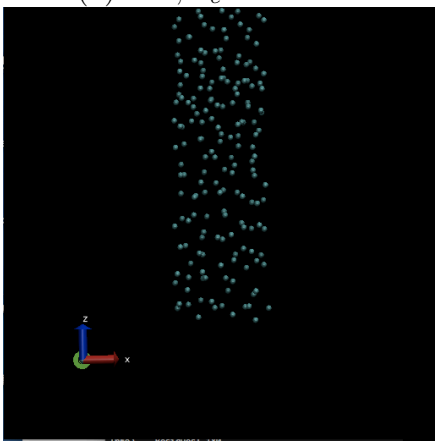

(f) IAP, $T_e = 20000\,\mathrm{K}$

Figure 4.16: Snapshots of MD simulations at small film system of $t = 900\,\mathrm{fs}$ after T_e is changed to high T_e. Each figures represent the simulations at (a), (b) $T_e = 15000\,\mathrm{K}$, (c), (d) $T_e = 17500\,\mathrm{K}$, and (e), (f) $T_e = 20000\,\mathrm{K}$. The left figures [(a), (c), (e)] are results of first-principles MD calculations based on FTDFT, and the right figures [(b), (d), (f)] are results of classical MD simulations using the IAP. These figures are visualized using using Visual Molecular Dynamics (VMD) [118].

Interpolation of E, F, and $-ST_e$

In this study, the linear interpolation method is used to determine the parameter values for E, F, and $-ST_e$. Here, we verify the adequacy of the interpolation. Figure 4.17 shows T_e-dependence of these values. Solid, bold, and dashed lines represent E, F, and $-ST_e$, calculated by IAP, while the symbols represent the results by DFT, respectively. Calculated structure is the equilibrium fcc structure. From Fig. 4.17, we find that the error coming from the linear interpolation method is expected to be small especially at low T_e.

Electronic heat capacity: $C_e(T_e)$

Figure 4.18 represents T_e-dependence of $C_e(T_e)$. Dashed line represents estimated values [Eq. (3.3)] from the FTDFT calculations [88,89]. Bold line represents the IAP results. Calculated structure is the fcc structure at $T_e = 300\,\mathrm{K}$. Figure 4.18 shows that there is a large discrepancy between IAP and FTDFT calculations. This reason can be attributed to the linear interpolation. Effect of these discrepancy is discussed in Sec. 4.3. Important values for the ablation simulation is integrated value of $C_e(T_e)$, that is, the internal energy E. Since Fig. 4.17 shows the accuracy of E, difference of the $C_e(T_e)$ is expected to be not crucial.

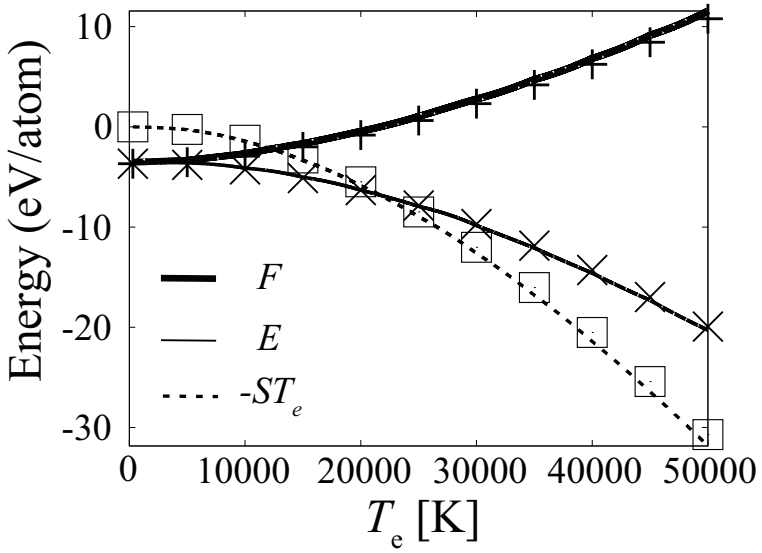

Figure 4.17: T_e-dependence of E, F, and $-ST_e$. Solid, bold, and dashed represent E, F, and $-ST_e$ of the ISP calculations, respectively. Plus, cross, and square marks represent E, F, $-ST_e$ of FTDFT calculations, respectively. Calculated structure is the equilibrium fcc structure at $T_e = 300\,\mathrm{K}$.

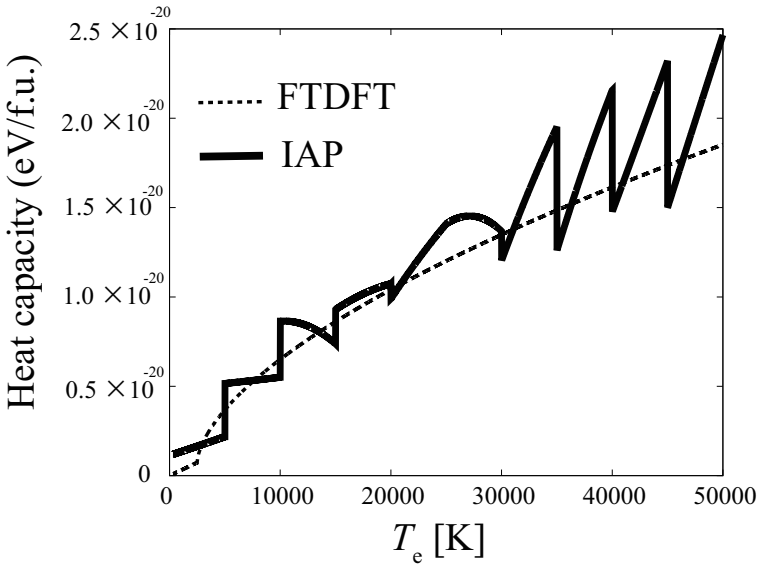

Figure 4.18: Calculation results of $C_e(T_e)$. Dashed line represents estimated values from FTDFT calculations [88, 89]. Bold line represents the IAP results. Calculated structure is the fcc structure at $T_e = 300\,\mathrm{K}$.

4.3 Test calculation: energy conservation

Here, we show that our TTM-MD simulation scheme satisfies the law of conservation of energy with a little error. In addition, Δt_{MD} dependence of the conserved energy is investigated to find appropriate t_{MD} for the following simulations.

Figure 4.19 represents a schematic image of the total energy deposited by a laser irradiation I_{tot}, the internal energy of the MD region E_{MD}, and the dissipated-energy to the CM region D_{CM}. By using these quantities, the conserved energy of the MD region can be written as $E_{\mathrm{cons}} = E_{\mathrm{MD}} - I_{\mathrm{tot}} + D_{\mathrm{CM}}$. Besides, for comparison, we calculate $F_{\mathrm{uncons}} = E_{\mathrm{cons}} - ST_e$, which is regarded as the conserved energy in the previous studies.

Figure 4.20 represents the results of the Δt_{MD} dependence of E_{cons} and F_{uncons}. Figure 4.20(a) represents simulation results where a laser is not applied. On the other hands, Figs. 4.20(b) and (c) represent simulation results of the Cu film irradiated by a laser with (b) $J_0 = 0.4\,\mathrm{J\,cm^{-2}}$, where ablation is not caused, and with (c) $J_0 = 0.6\,\mathrm{J\,cm^{-2}}$, where ablation is caused, respectively. In the latter two simulations, T_e near the surface increases to approximately 20000 K. Black, green, and blue lines indicate calculation results of $\Delta t_{\mathrm{MD}} = 0.5, 1$, and 5 fs, respectively. The total number of atoms in the computational cell is approximately 4.0×10^5.

These figures show that, if sufficiently small Δt_{MD} is used, our simulations satisfy the law of conservation of energy with several $10\,\mathrm{meV\,atom^{-1}}$ errors, and that F_{uncons} is not conserved. Since Figs. 4.20(b) and (c) show that E_{cons} returns back to the initial value at $t > 10\,\mathrm{ps}$, where

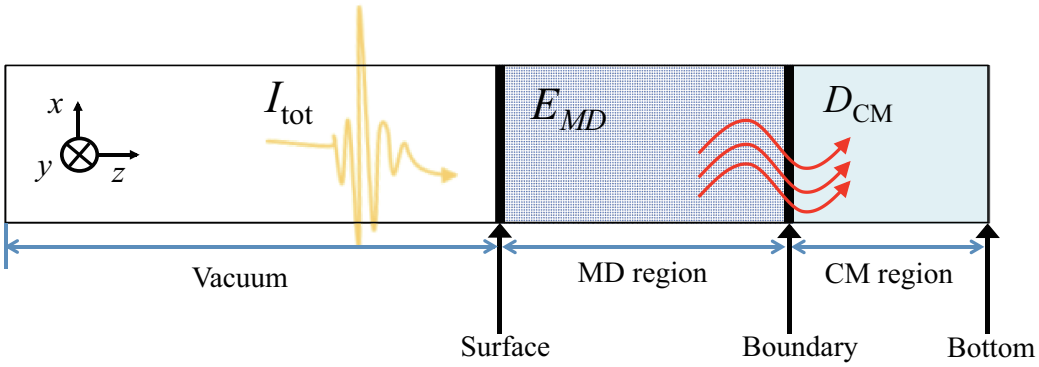

Figure 4.19: Schematic image of the conserved energy $E_{\mathrm{cons}} = E_{\mathrm{MD}} - I_{\mathrm{tot}} + D_{\mathrm{CM}}$. I_{tot} is the total energy deposited by laser irradiation, E_{MD} is the internal energy of the MD region, and D_{CM} is the dissipated-energy to the CM region.

low electronic temperature ($T_e \simeq 1000\,\mathrm{K}$) are realized, these errors of E_{cons} are caused only at high T_e. Therefore, we consider that these errors are coming from the discrepancy between the heat capacities of the T_e-dependent IAP and that used in the calculation of the CM region [see: Fig. 4.18 and Eq. (4.1)].

Figure 4.20(a) shows that E_{cons} is conserved with little or no error at all Δt_{MD}. On the other hands, Figs. 4.20(b) and (c) represent that, when a laser is applied, the short time step Δt_{MD} is needed to conserve E_{cons}. We considered that this is attributed to the high energy atoms emission by laser irradiation.

At all time, we check the energy conservation of the simulation in the following subsection, and suitable t_{MD} is used in each simulation. We carry out simulations with $\Delta t_{\mathrm{MD}} = 1\,\mathrm{fs}$ in the case of $J_0 < 0.9\,\mathrm{J\,cm^{-2}}$ and with $\Delta t_{\mathrm{MD}} = 0.5\,\mathrm{fs}$ in the case of the $J_0 \geq 0.9\,\mathrm{J\,cm^{-2}}$.

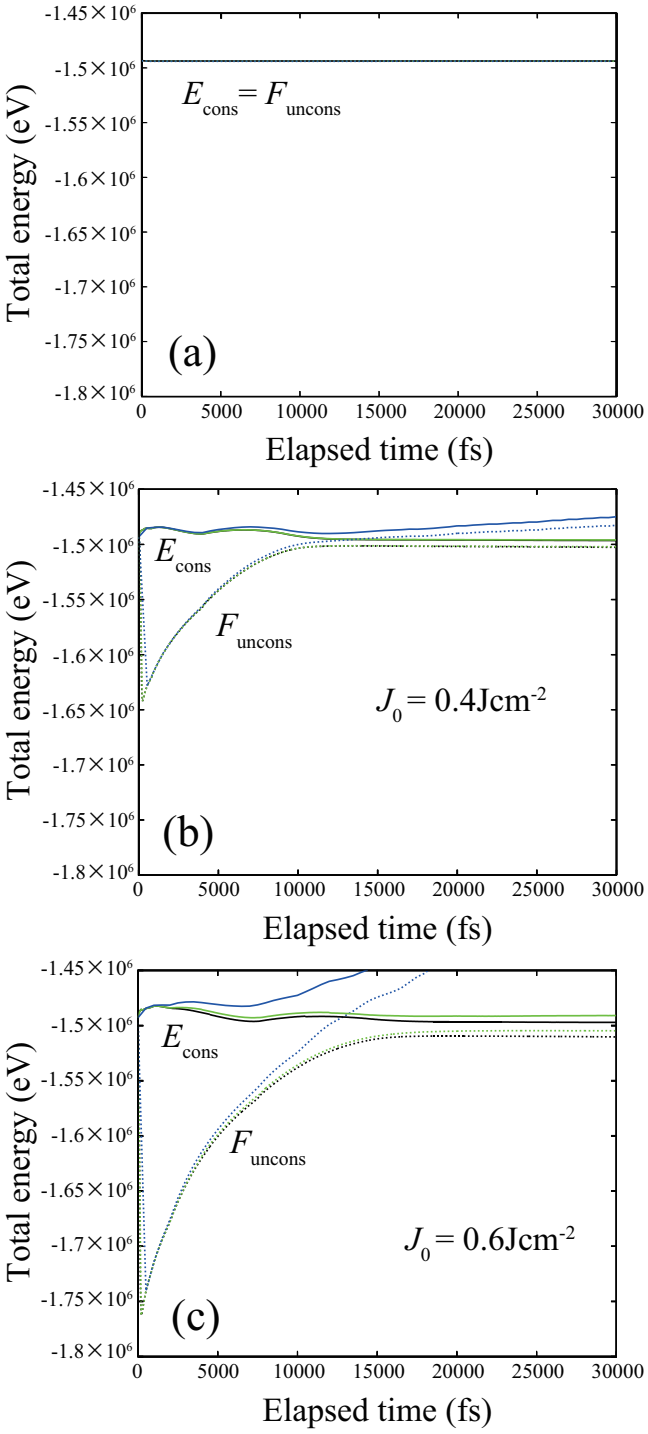

Figure 4.20: Time development of E_{cons} and F_{uncons}. (a) represents simulations where a laser is not applied. (b) and (c) represent simulation results of the Cu film irradiated by a laser with (b) $J_0 = 0.4\,\mathrm{J\,cm^{-2}}$, where ablation is not caused, and with (c) $J_0 = 0.6\,\mathrm{J\,cm^{-2}}$, where ablation is caused, respectively. Black, green, and blue lines indicate calculation results of $t_{\mathrm{MD}} = 0.5, 1.0$, and $5.0\,\mathrm{fs}$, respectively. The total number of atoms in the computational cell is approximately 4.0×10^5.

4.4 Results

Here, we show the TTM-MD simulation results of the ablation process and analyze them.

First, we show the simulation results of the ablation near the ablation threshold. Subsequently, we investigate the ablation processes that are caused by laser irradiation whose fluence is a little above the ablation threshold. In addition to these simulations using the T_e-dependent IAP, for comparison, we performed simulations using T_e-independent IAP. Based on these simulation results, we analyze the physical mechanism of the ablation process. Moreover, we compare the TTM calculation results of ablation depth with the CM calculation results and the experimental results. Consequently, we find that the TTM-MD simulations agree with these results. In addition, we describe that our simulation can qualitatively explain experimental results, such as the pulse duration dependence of the ablation threshold.

4.4.1 Ablation near the ablation threshold: emission of atoms

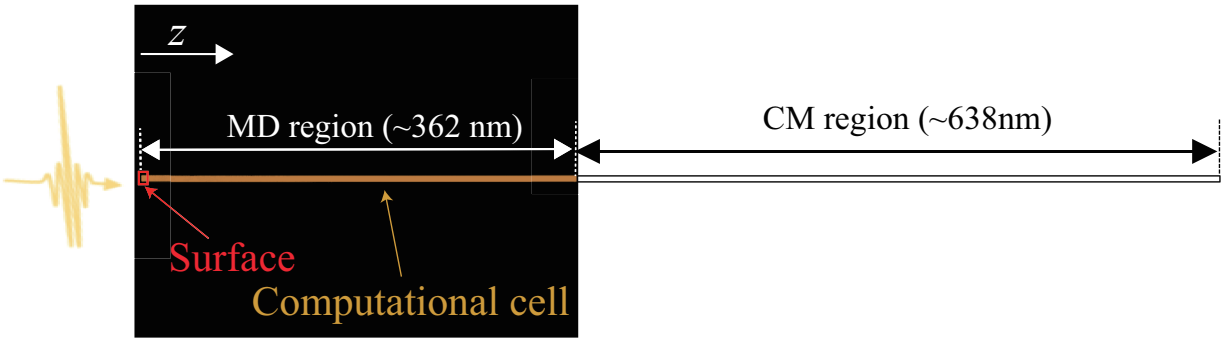

Figure 4.21: Schematic image of the computational cell of the TTM-MD simulations. The laser comes from the left side of this figure. z direction represents the depth direction of the film. The periodic boundary condition is used in the parallel to the surface directions. Under the bottom of the MD region, the CM region is connected (see: Fig. 4.1). In the following figures, such as Figs. 4.22 and 4.26, the region only near surface is shown. These figures are visualized using Open Visualization Tool (OVITO) [123].

Here, we exhibit the simulation results of the ablation process in the low-laser-fluence region. The simulated computational cell is described in Fig. 4.21.

In our simulation, an atom emission is observed when the Cu surface is irradiated with the laser with a fluence of $J_0 = 0.55\,\mathrm{J\,cm^{-2}}$. Therefore, the ablation threshold fluence is estimated to $J_0 = 0.55\,\mathrm{J\,cm^{-2}}$, which is well consistent with the result of our CM simulations in Chap. 3 ($J_0 = 0.47\,\mathrm{J\,cm^{-2}}$). This results show the potential to explain the previous experimental results [46], in which less than 0.01 nm ablation was observed. Moreover, we found that the average energy of the emitted atoms is 46.5 eV. This simulation result is consistent with the experimental value

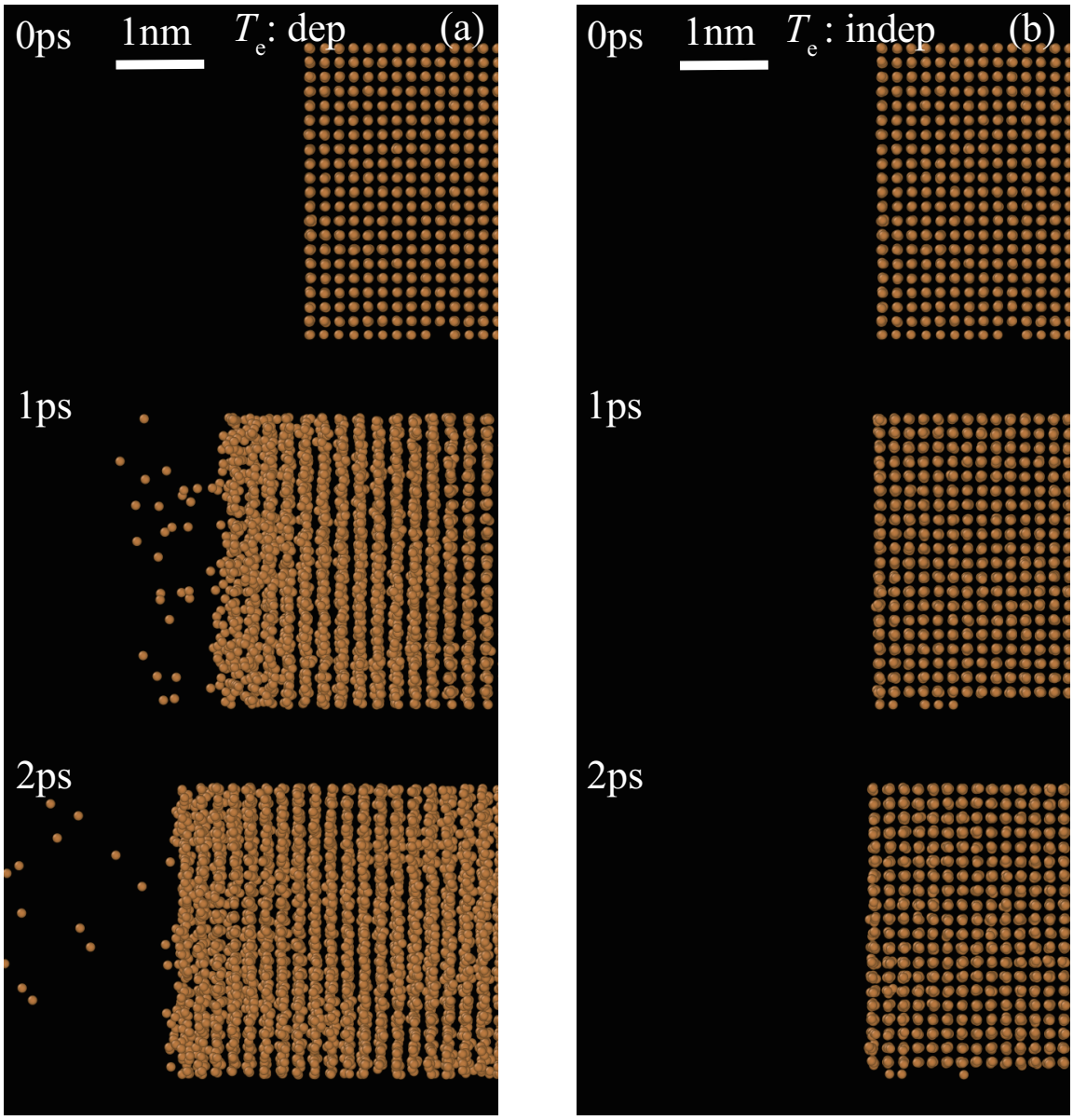

Figure 4.22: Snapshots of MD simulations after irradiation with the laser of $J_0 = 0.57\,\mathrm{J\,cm^{-2}}$. These simulations are carried out using (a) the T_e-dependent IAP and (b) the T_e-independent IAP.

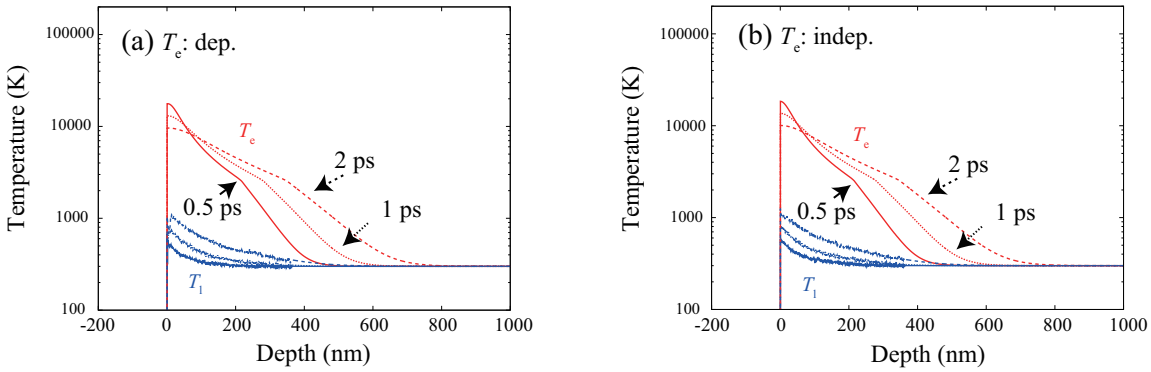

Figure 4.23: T_e and T_l space distribution. These figures represent the simulation results using (a) the T_e-dependent IAP and (b) the T_e-independent IAP. Solids, dashed and dotted lines represent the results at $t = 0.5$, 1.0, and 2.0 ps, respectively.

(about 30 eV [7]), which is the most probable energy of the emitted Cu^+ by the irradiation with the laser of the ablation threshold fluence.

Besides, by irradiation with a laser of $J_0 = 0.57\,\mathrm{J\,cm^{-2}}$, several atoms are emitted. Figure 4.22(a) shows this simulation result. In this simulation, the laser is applied from the left side of these figures, and the fluence peak of the laser reaches the surface at $t = 0.2$ ps. These figures are visualized using Open Visualization Tool (OVITO) [123]. In addition to the T_e-dependent IAP simulation, we carried out the simulation using the T_e-independent IAP for comparison. This result is shown in the Fig. 4.22(b).

Figure 4.22(a) shows that, using the T_e-dependent potential, where the electronic entropy effect is included, atoms are emitted from the surface. This figure also exhibits that the displacement of the atoms at the depth of ~ 2 nm is small, even though the surface atoms are emitted. On the other hands, Fig. 4.22(b) shows that, using the T_e-independent potential, the atom emission is not caused and the displacement of these atoms are little.

Figure 4.23 represents that the space distributions of T_e and T_l. There are little difference between the T_e-dependent IAP calculation and the T_e-independent IAP calculation. Therefore, it is obvious that the atoms emission in the T_e-dependent IAP simulation can not be explained by the thermalized kinetic energy of atoms. Of course, the T_e-dependence of E is also included in the T_e-dependent effect, but the effect of E leads to the attractive force [see: Fig. 2.1]. Therefore, we consider that the origin of the large repulsion force, which causes the atom emission, comes from the electronic entropy effect. The contribution of the electronic entropy effect can be investigated more directly by energy analysis. Figure 4.24 represents the energy absorbed by the electronic entropy term in F, at each depth. Solid, dashed, and dotted lines represent results at $t = 0.5, 1.0$, and 1.5 ps, respectively. This figure shows that the electronic entropy effect plays important role near the surface, and the value of the absorbed energy is of the same order as the cohesive energy (3.49 eV [104]).

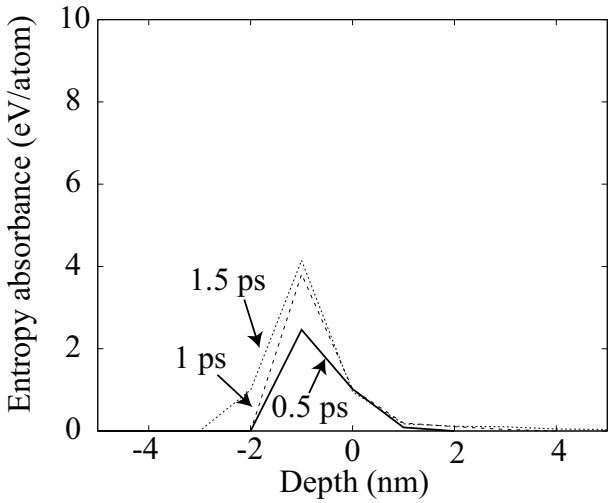

Figure 4.24: The energy absorbed by the electronic entropy effect, at each depth. A laser fluence is $J_0 = 0.57\,\mathrm{J\,cm^{-2}}$. Solid, dashed, and dotted lines represent results at $t = 0.5$, 1.0, and 1.5 ps, respectively.

Figure 4.25 represents that the space distributions of the local pressure along the z-direction p_z. According to the simple deviation by Basinski *et al.* [124] based on the virial theorem, the local pressure p^n in the n-th 3D cell also can be calculated from the below equations:

$$p^n = \frac{1}{3V^n}\left[< \sum_i^{N^n} m(v_i^n)^2 > + < \frac{1}{2}\sum_{i\neq j}^{N^n}\sum_j^{N^{\mathrm{tot}}} r_{ij}\cdot f_{ij} > \right]. \tag{4.63}$$

Here, V^n is the volume of the n-th 3D cell, N^{tot} is the total number of atoms, and f_{ij} is the force between the i-th and the j-th atoms. The bracket means the time average. In our calculation, the value of p^n is averaged within 100 fs. Here, we focus on the only the local pressure along the z-direction, which is the most important for the ablation dynamics.

Figure 4.25(a) shows that, in the T_e-dependent IAP simulation, the pressure is created in the wide region because of the electronic entropy effect at high T_e. In addition, this figure shows that the particularly high pressure is created near the surface, of which the origin is considered to be the recoil pressure of the atom emission. We also find that larger negative pressure is created near the surface compared with the T_e-independent IAP simulation.

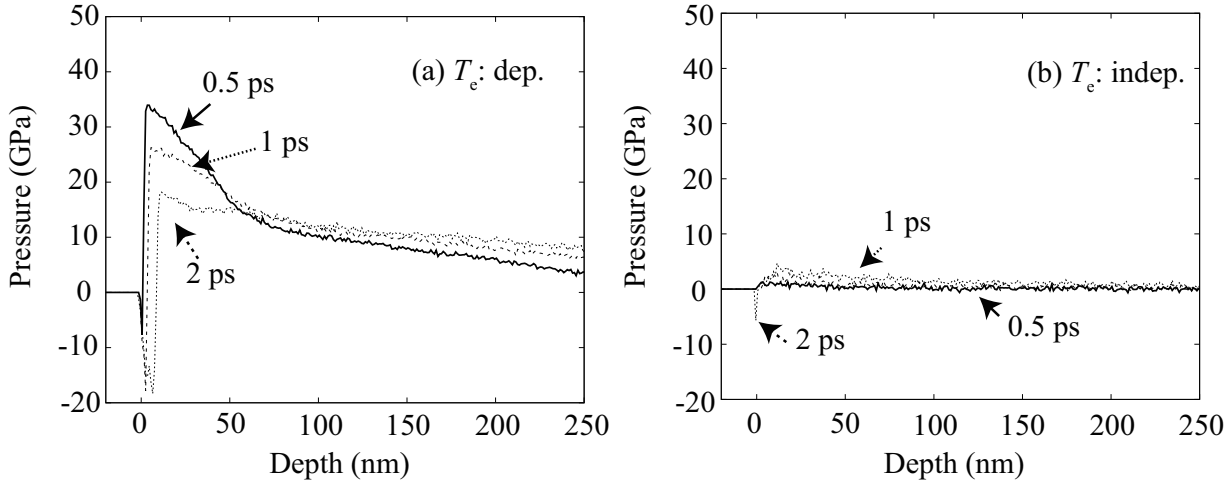

Figure 4.25: The space distribution of the local pressure along the z-direction of simulations using (a) the T_e-dependent IAP and (b) the T_e-independent IAP. Bold, dashed, and dotted lines represent the results at $t = 0.5$, 1.0, and 2.0 ps, respectively.

4.4.2 Ablation a little higher than the ablation threshold: spallation

Here, we exhibit results of simulations, in which a fluence of the applied laser ($J_0 = 0.70\,\mathrm{J\,cm^{-2}}$) is a little above the ablation threshold ($J_0 = 0.55\,\mathrm{J\,cm^{-2}}$).

Figure 4.26 shows the snapshots of the simulation. As shown in Fig. 4.26(b), when the T_e-independent IAP is used in the simulation, ablation does not occur by laser irradiation with $J_0 = 0.70\,\mathrm{J\,cm^{-2}}$. On the other hands, Fig. 4.26(a) shows that ablation occurs by the T_e-dependent IAP. As shown in Fig. 4.27, the absorption of the electronic entropy becomes larger than that of the simulation of lower laser irradiation because a lot of atoms are emitted and kinetic energy of emitted atoms becomes larger.

A wide view of this simulation is shown in Fig. 4.28. As shown in these figures, the spallation process is also observed. Figure 4.29 shows a part of the computational cell (depth: ~ 10 nm) of Fig. 4.28. The space distribution of the local pressure along the z-direction is shown in Fig. 4.30(a). At least within $t = 5$ ps, the pressure wave passes through the point, where the spallation occurs, and the negative pressure is generated. Owing to the negative pressure, the void begins to be formed around $t = 9$ ps, and as a results, the spallation is caused. In the simulation of the T_e-independent IAP, spallation does not occur at least within 100 ps. Figure 4.30 shows that the negative pressure of the T_e-independent IAP simulation is smaller than that of the T_e-dependent IAP simulation by one order of magnitude. It has been widely accepted that large negative pressure is the origin of the spallation [28]. Hence, we consider that the spallation is not caused in the T_e-independent IAP simulation because of the small negative pressure. From these results, we conclude that the electronic entropy effect is attributed to not only the atom emission but also greatly the spallation process. The spallation is observed

between $J_0 = 0.7$ and $0.9\,\mathrm{J\,cm^{-2}}$.

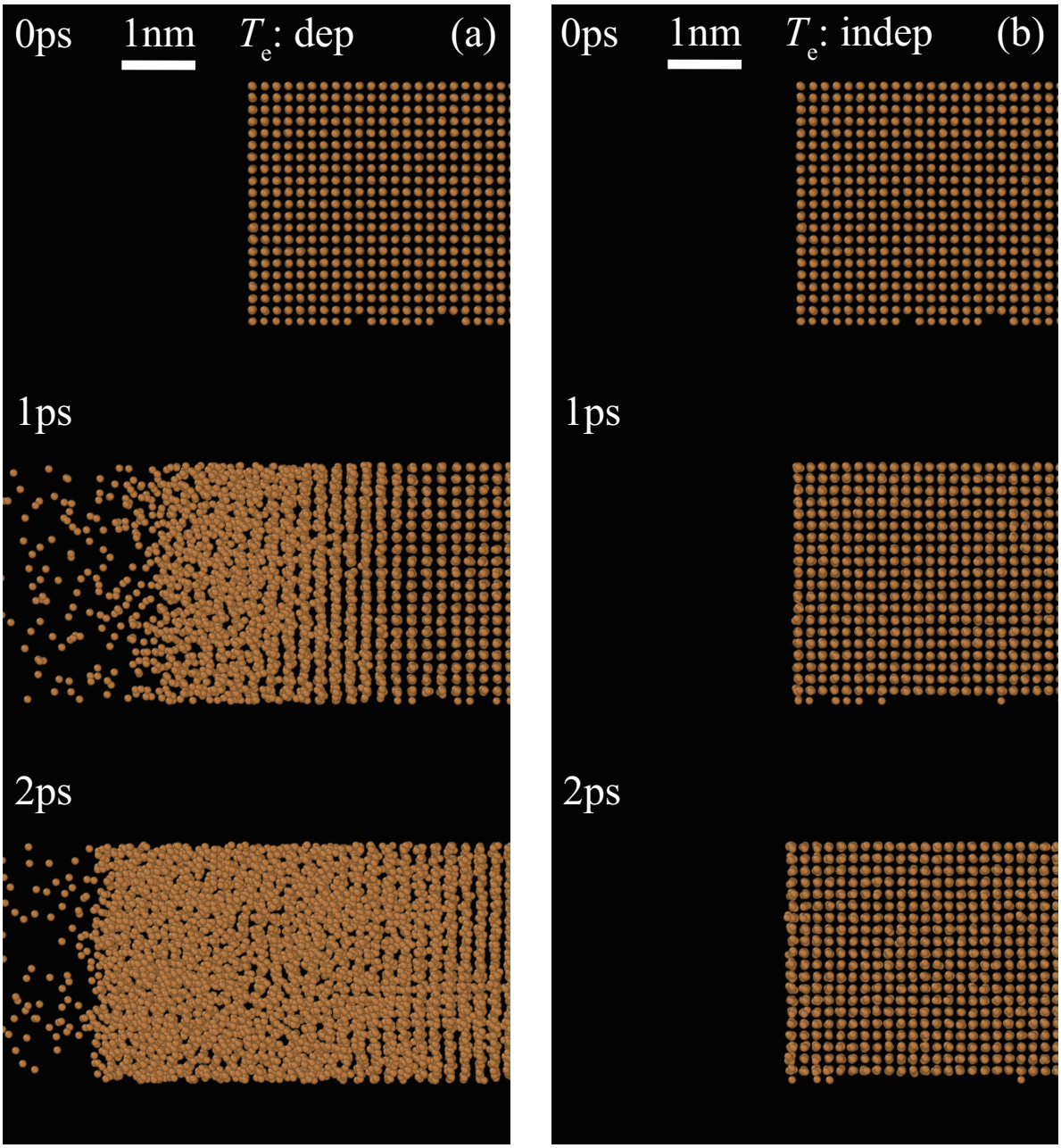

Figure 4.26: Snapshots of the TTM-MD simulations after irradiation of the laser with $J_0 = 0.7\,\mathrm{J\,cm^{-2}}$. These simulation was carried out using (a) the T_e-dependent IAP and (b) the T_e-independent IAP.

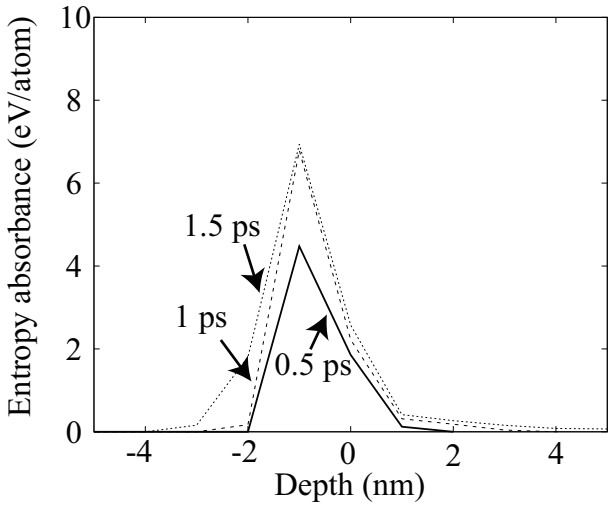

Figure 4.27: Energy absorbed by the electronic entropy effect, at each depth. A laser fluence is $J_0 = 0.70\,\mathrm{J\,cm^{-2}}$. Solid, dashed, and dotted lines represent each elapsed time $t = 0.5$, 1.0, and 1.5 ps, respectively.

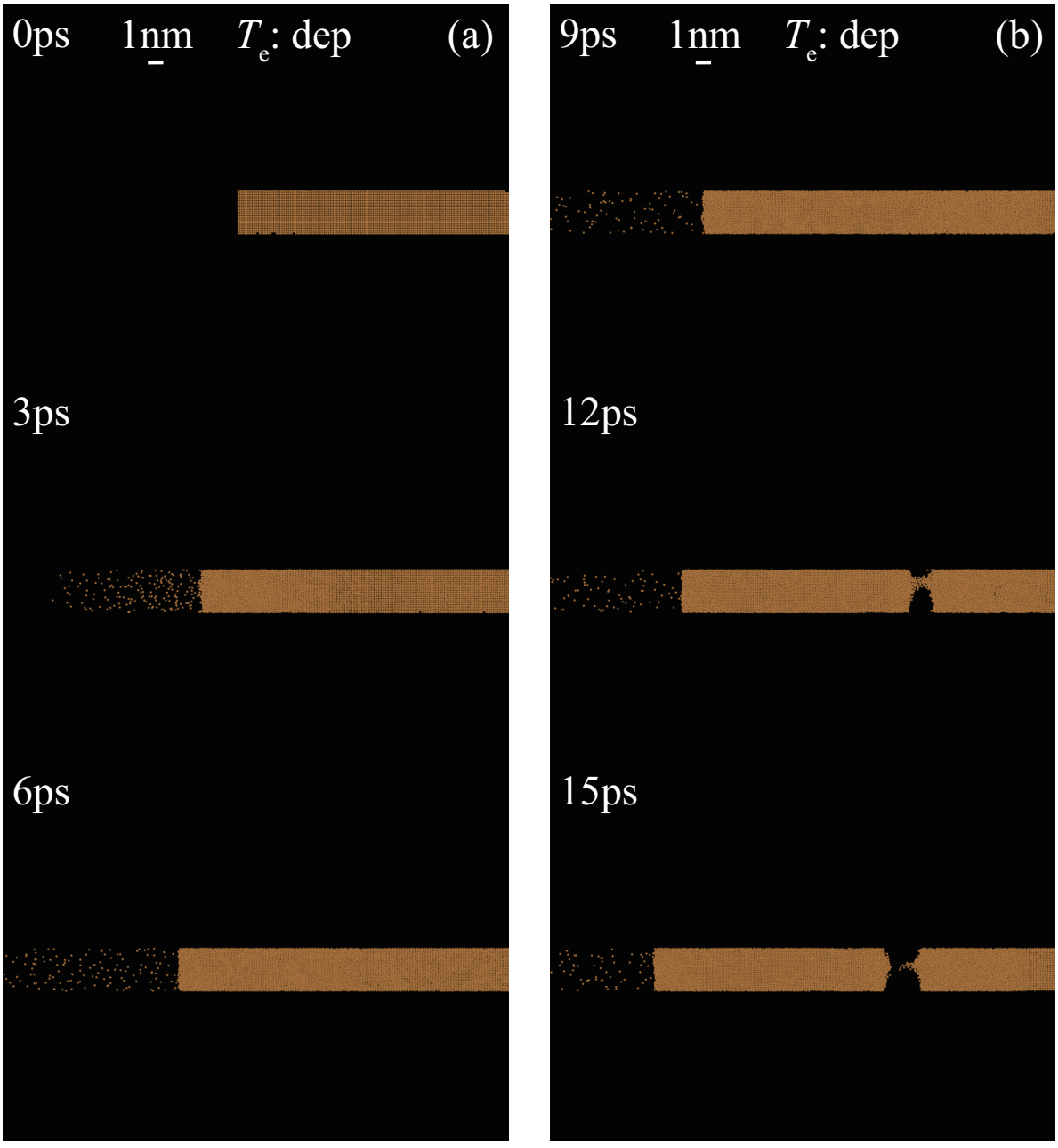

Figure 4.28: Wide view of Fig. 4.26(a). These simulation was carried out using the T_e-dependent IAP.

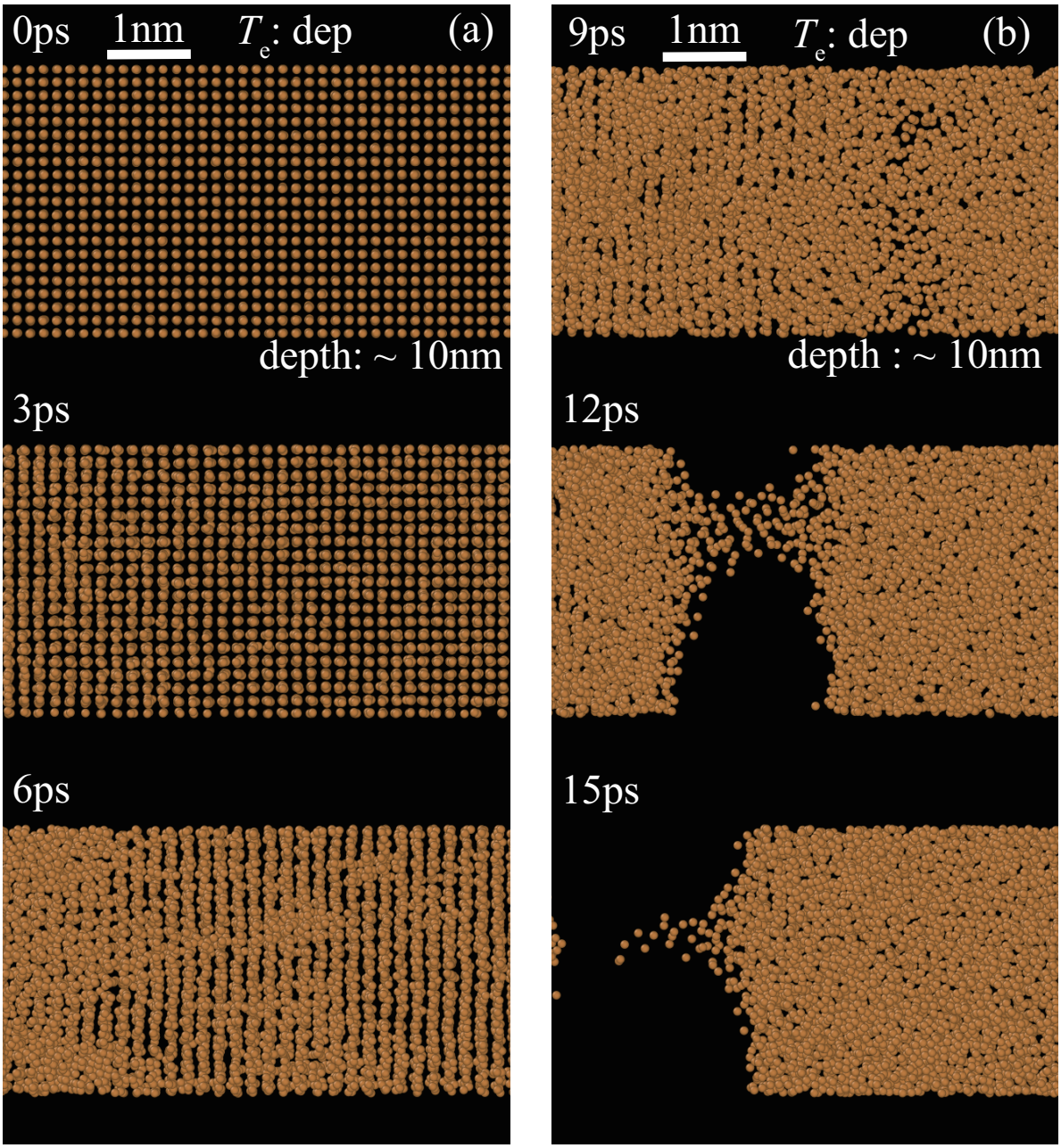

Figure 4.29: Part of the snapshots (depth: $\sim 10\,\mathrm{nm}$) of Fig. 4.28.

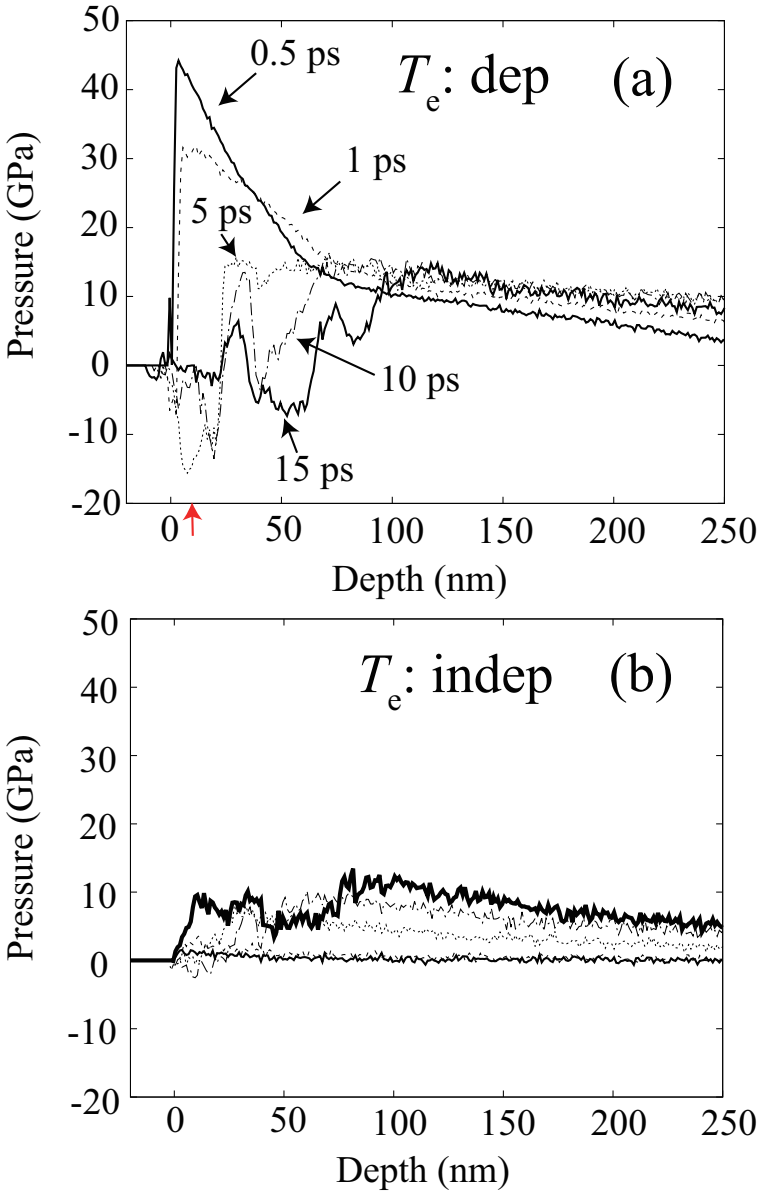

Figure 4.30: Space distribution of the local pressure along the z-direction of simulations using (a) the T_e-dependent IAP and (b) the T_e-independent IAP. Solid, dashed, dotted, chained, and bold lines represent the results at $t = 0.5$, 1.0, 5.0, 10.0, and 15.0 ps, respectively. Red arrow in (a) represents the point where the spallation is caused.

4.4.3 Ablation a little higher than the ablation threshold: phase explosion

Here, we exhibit results of a simulation, in which a fluence of the applied laser is $J_0 = 1.0\,\mathrm{J\,cm^{-2}}$.

Figure 4.31 shows the snapshots of the simulation. The ablation depth of this simulation is 37.8 nm, which is estimated from the number of emitted atoms within 50 ps. Figure 4.31(a) shows that the homogeneous evaporation are observed near the laser irradiated surface, which is called the phase explosion. This results represents that as a laser fluence becomes larger, the ablation process is changing from the spallation process to the phase explosion process. This result is qualitatively consistent with the previous MD simulation [28] in which T_e-independent IAP is used.

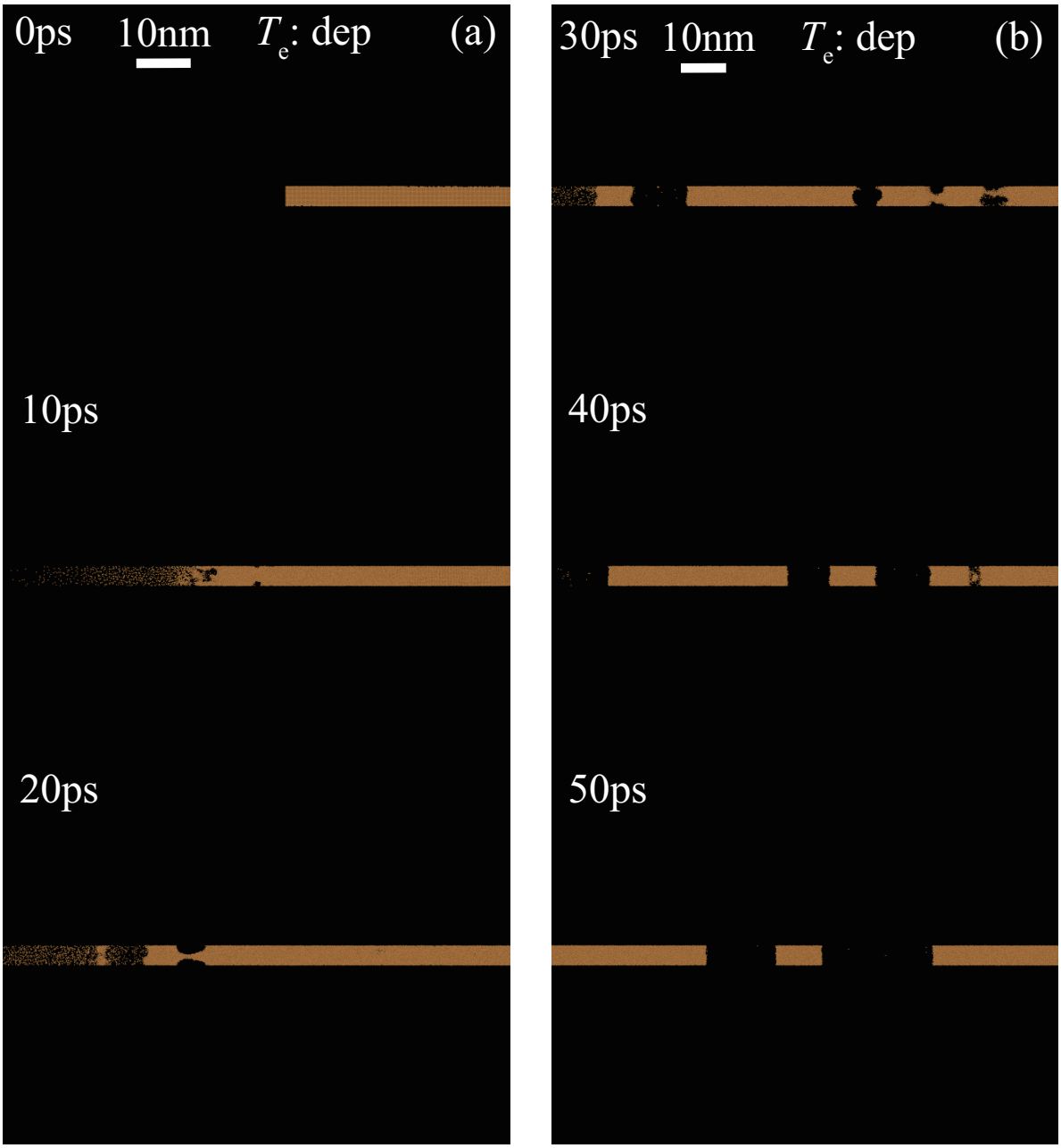

Figure 4.31: Snapshots of MD simulations after laser irradiation with $J_0 = 1.0\,\mathrm{J\,cm^{-2}}$. This simulation was carried out using the T_e-dependent IAP.

4.4.4 Ablation depth

Here, we show the simulation results of the ablation depth and compare them with the CM simulation (Chap. 3) and the experimental results [58, 59]. The ablation depth is estimated from the number of the ejected atoms within 50 ps. Our calculation results of the ablation depth are represented in Figs. 4.32 and 4.33, which is an enlarged view of the low fluence region of Fig. 4.32. Dotted line represents the results of our CM calculation in Chap. 3, and cross marks represent the results of the TTM-MD simulations. Triangle and square marks represent experimental results [58, 59].

As shown in Fig. 4.33, our TTM-MD simulation can reproduce the CM simulation results and the experimental results, quantitatively. Figure 4.33 shows that the ablation depth significantly change at $J_0 = 0.60\,\mathrm{J\,cm^{-2}}$, at which ablation process is changed to the spallation process. Ablation depth at $J_0 = 0.55$ and $0.57\,\mathrm{J\,cm^{-2}}$ in the TTM-MD simulation are 0.001 and 0.030 nm, respectively. Therefore, the ablation depth changes by more than two orders of magnitude around $J_0 = 0.60\,\mathrm{Jcm^{-2}}$. A previous experiment [7, 46] reported that similar large change of the ablation depth. Also from this perspective, our simulation is consistent with experiment.

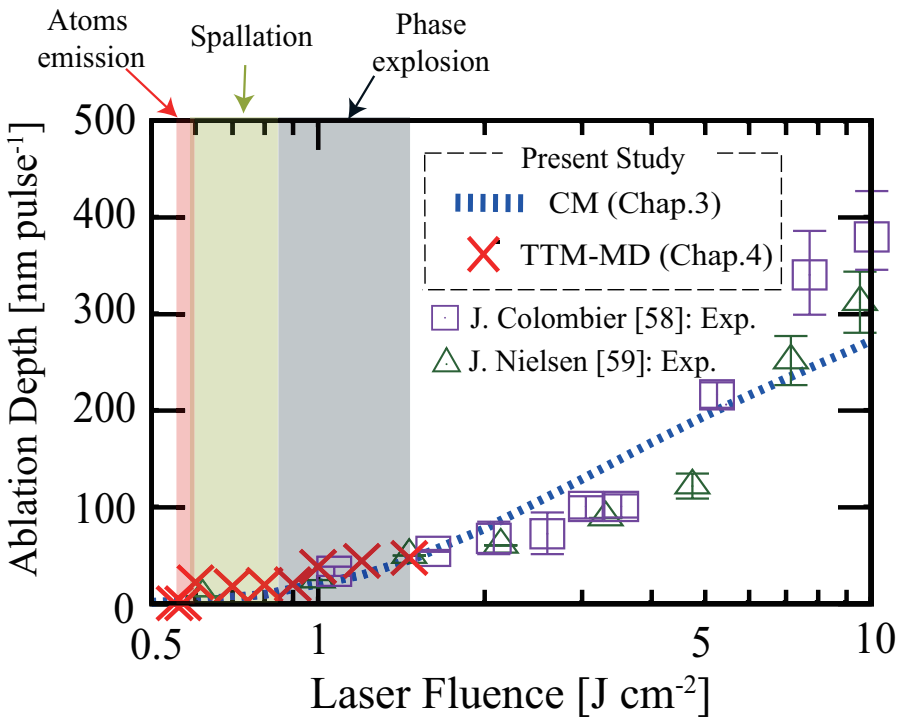

Figure 4.32: Results of the ablation depth calculations. Dotted line represents the results of our CM calculation (Chap. 3) and cross marks represent the results of the TTM-MD simulations. Triangle and square marks represent experimental results [58, 59].

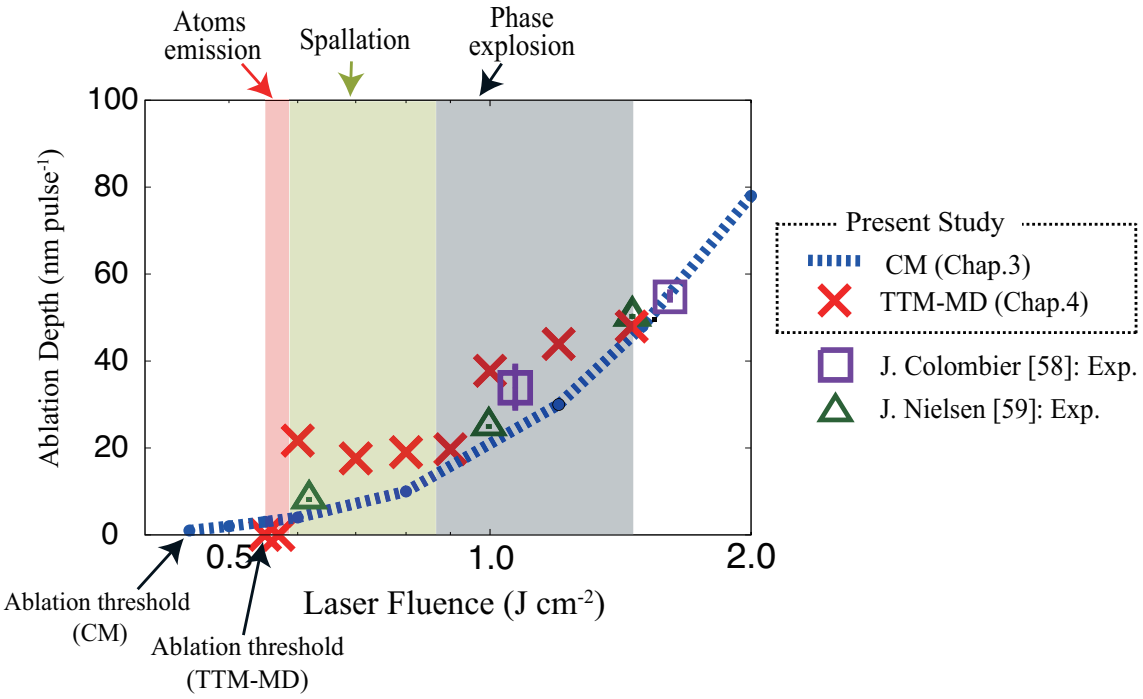

Figure 4.33: Enlarged view of the low fluence region of Fig. 4.32. Ablation thresholds of the CM calculation and its TTM-MD calculation are $J_0 = 0.47$ and $0.55\,\mathrm{J\,cm^{-2}}$, respectively. Ablation depth of $J_0 = 0.55$ and $0.57\,\mathrm{J\,cm^{-2}}$ in TTM-MD simulation are 0.001 and 0.030 nm, respectively.

4.4.5 Pulse-width dependence

Here, we investigate the pulse-width dependence of the ablation threshold. A previous study [125] has reported that the ablation threshold fluence of ultrashort pulse laser is lower than that of the ps-laser. We investigate whether our simulation can qualitatively reproduce this experimental result.

Figure 4.34 represents that the space distributions of T_e and T_l. Duration time of the laser pulse is 200 ps and its fluence is $J_0 = 0.70\,\mathrm{J\,cm^{-2}}$. The fluence peak of the laser reaches the surface at $t = 200$ ps. As shown in Fig. 4.34, the difference between T_e and T_l is smaller compared with the simulation of the ultrashort pulse laser irradiation. In this simulation, ablation does not occur at least within 300 ps. In the case of the ultrashort pulse laser irradiation with the same fluence, ablation is caused (see: Fig. 4.26). Here, we show that our simulation can qualitatively reproduce experimental results of the pulse-width dependence of the ablation threshold.

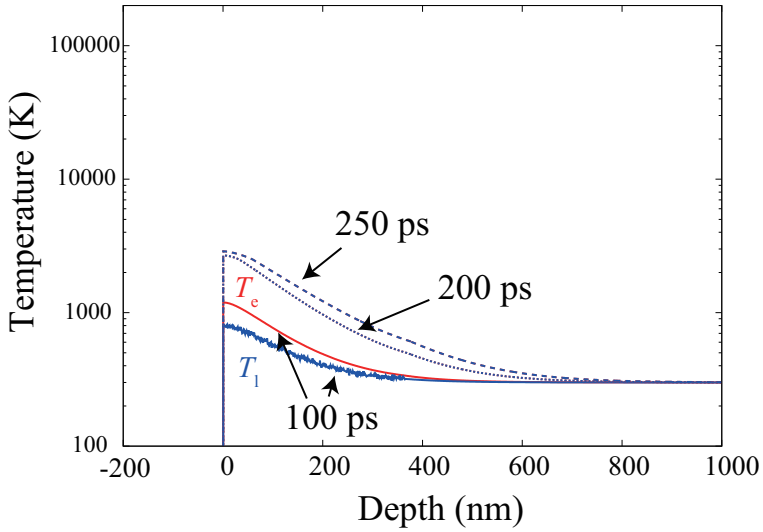

Figure 4.34: Results of T_e(red line) and T_l(blue line) space distribution. Duration time of the laser pulse is 200 ps and its fluence is $J_0 = 0.70\,\mathrm{J\,cm^{-2}}$. The fluence peak reaches the surface at $t = 200$ ps. Solids, dashed and dotted lines represent the results at $t = 100$, 200, and 250 ps, respectively. The dashed and the dotted lines are completely overlapped.

4.5 Summary

Here, we showed the TTM-MD simulation results of the ablation process and analyzed them.

First, we investigated the physical mechanism of the ablation near the ablation threshold fluence. Based on the result of the TTM-MD simulation, we observed that the high-energy atoms emission is caused near the ablation threshold. Moreover, we elucidated that the electronic

entropy effect is the dominant factor to cause it. In addition, we show that the spallation process and the phase explosion process are also strongly affected by the electronic entropy effect. Moreover, we compared the TTM-MD calculation results of ablation depth with the CM calculation results and the experimental data. As a result, our TTM-MD simulations are well consistent with these results, quantitatively. Also, we showed that our simulation can qualitatively reproduce experimental results, such as the large change of the ablation depth near the ablation threshold [46] and the pulse-width dependence of the ablation threshold [125].

5. Material Dependence of Ablation Threshold

In this chapter, based on the results of the CM simulations (Chap. 3) and the TTM-MD simulations (Chap. 4), we develop a simple model to calculate the ablation threshold fluence J_{thr} of several materials [chromium (Cr), tungsten (W), molybdenum (Mo), nickel (Ni), platinum (Pt), aluminum (Al), silver (Ag), copper (Cu), and gold (Au)].

First, we explain the calculation model and parameters for J_{thr} calculation. Subsequently, we discuss the versatility of the EED mechanism and dominant factors that determine J_{thr}.

5.1 Methods and assumptions

In this section, the developed method and used assumptions are explained.

To investigate the contribution of the electronic thermal conductivity and the electron-phonon scattering for J_{thr}, we carried out TTM-MD simulations without these effects. In other words, TTM-MD simulations were performed under the condition of $G^n = 0$ and $\kappa_e^n = 0$ in Eq. (4.1). Under these conditions, J_{thr} is decreased approximately 10 % in the case of Cu. Therefore, we expect that these effects can be neglected for the materials, and these effects are neglected in our simulation model.

The Beer-Lambert law is used, which assumes the exponential decay of laser absorption with depth z. Laser deposited energy density $E(z)$ at each depth can be expressed as

$$E(z) = \frac{(1-R)J}{l_p} \exp\left[-\frac{z}{l_p}\right], \tag{5.1}$$

where R is the reflectivity of the surface, J is the laser fluence at the center of the laser spot, and l_p is the penetration depth of the laser. Hence, the laser-deposited-energy density at surface E_{surf} can be represented as

$$E_{\mathrm{surf}} = \frac{(1-R)J}{l_p}. \tag{5.2}$$

From here, we derive a simple equation to calculatet J_{thr}. Based on the EED mechanism, we can consider that atoms are emitted from the surface, when the lattice temperature at the surface has sustained higher electronic temperature than ablation threshold temperature T_e^{thr}, at which the value of the activation barrier for dissociation $F_{\mathrm{dis}}(T_e)$ is 0 (see Fig. 3.2). According

to the TTM-MD simulation (Chap. 4), a part of E_{surf} is used for the absorption by the electronic entropy term so that corresponding energy is necessary to sustain higher T_e than T_e^{thr}. This energy is considered to be the cohesive energy E_{coh} at low T_e. Based on these assumptions, ablation is expected to occur when the following equation is satisfied:

$$E_{\mathrm{surf}} \geq \int_0^{T_e^{\mathrm{thr}}} C_e(T_e) dT_e + E_{\mathrm{coh}}. \tag{5.3}$$

Here, the definition of T_e^{thr} is $F_{\mathrm{dis}}(T_e^{\mathrm{thr}}) = 0$ (see Fig. 3.2), and $C_e(T_e)$ is the electronic heat capacity. Using Eqs. (5.2) and (5.3), J_{thr} can be written as

$$J_{\mathrm{thr}} = \frac{\int_0^{T_e^{\mathrm{thr}}} C_e(T_e) dT_e + E_{\mathrm{coh}}}{1 - R} l_p. \tag{5.4}$$

Except for Cr, the value of $C_e(T_e)$ are obtained from previous studies [89, 126, 127], where FTDFT calculations were performed with the GGA exchange-correlation functional. Since $C_e(T_e)$ of Cr is not found, we calculated it using the VASP code [112–114] with the same exchange-correlation functional as the previous studies. Values of the other parameters in Eq. (5.4) are obtained from previous experimental results [51, 89, 104, 117, 126–131]. We summarized these parameters in Table 5.1. There are two different R and l_{p} for Al since these values represent results of different wavelength $\lambda = 800$ and 1028 nm laser irradiation.

Table 5.1: Values of parameters that is used to calculate J_{thr}.

	Cr	W	Mo	Ni	Pt	Al	Ag	Cu	Au
R	0.41 [128]	0.48 [129]	0.554 [130]	0.56 [130]	0.70 [131]	0.88 [130], 0.94 [131]	0.92 [51]	0.94 [131]	0.952 [130]
l_p (nm)	12 [130]	23 [130]	19 [130]	16 [130]	7.7 [130]	7.5 [130], 8.1 [130]	12 [130]	13 [130]	12 [130]
E_{coh} (eV/atom)	4.10 [104]	8.90 [104]	6.82 [104]	4.44 [104]	5.84 [104,117]	3.39 [104,117]	2.95 [104,117]	3.49 [104,117]	3.8 [104]
$C_e(T_e)$	Our calc.	[89]	[127]	[126]	[89]	[89]	[89]	[89]	[89]

Table 5.2: Details of experiments [59,127,128,131–134] for J_{thr} calculations.

	Cr [128]	W [59]	W [132]	Mo [127]	Ni [127]	Pt [127]	Pt [133]	Al [134]	Ag [133]	Al [127]	Cu [131]	Au [127]
λ (nm)	800	800	790	1028	1028	1028	1030	800	1030	1028	800	1028
Duration (fs)	30	200	100	200	200	200	500	100	500	200	130	200
Surface	MP	MP		PD	PD	PD		PD	PD			PD

MP: Mechanical polished, PD: Pulsed-laser deposition

5.2 Results

In this section, we show the results of $T_e^{\rm thr}$ and $J_{\rm thr}$. We compare the calculated $J_{\rm thr}$ with the results of experiments [59, 127, 128, 131–134]. Experimental data and references are summarized in Table 5.2.

5.2.1 Ablation threshold temperature: $T_e^{\rm thr}$

To calculate $J_{\rm thr}$, FTDFT calculations were performed using the xTAPP [78] code with the PBE exchange-correlation functional and the ultra-soft pseudo potential. The plane-wave basis and the Brillouin-zone k-point sampling of a Monkhorst-Pack mesh were used. Each calculation detail is summarized in Table 5.3.

Fig. 5.1 represents our calculation results of the activation barriers for dissociation $F_{\rm dis}(T_e)$, which are calculated to estimate $T_e^{\rm thr}$. Square, circle, and triangle marks represent calculation results for transition metals, noble metals, and a poor metal, respectively. By linear interpolation of these calculation results, $T_e^{\rm thr}$ of several materials were obtained. The values of $T_e^{\rm thr}$ are summarized in Table 5.4

As mentioned in Chap. 2, the electronic entropy effect decreases the value of $F_{\rm dis}(T_e)$ due to the narrow band width at large volume. Generally, transition metals have higher DOS due to d-band near chemical potential than that of the noble metal and the poor metals. Hence, the electronic entropy effect of the transition metal would be larger than that of the noble and the poor metal metals. From only the viewpoint of the electronic entropy effect, $T_e^{\rm thr}$ of the transition metal (Cr, W, Mo, and Ni) would be smaller than that of the noble metal (Au, Ag, Cu, and Pt) and the poor metal (Al). Table 5.4 represents that this consideration can be applied to almost all materials except W, whose $T_e^{\rm thr}$ value is largest though it is classified in the transition metal. We consider that the reason for this is attributed to the large cohesive energy of W. Table 5.1 shows that the cohesive energy of W, of which the value is 8.90 eV, is largest in the materials in Table 5.4. On the other hand, the cohesive energy of Cr, of which $T_e^{\rm thr}$-value is the smallest, is smaller than other transition metals (Mo, Ni, and W). Based on these consideration, we conclude that $T_e^{\rm thr}$ is not only strongly dependent on its DOS, but also on other properties, such as the cohesive energy.

Table 5.3: Calculation details of our FTDFT calculations.

	Cr	W	Mo	Ni	Pt	Al	Ag	Cu	Au
Structure	bcc	bcc	bcc	fcc	fcc	fcc	fcc	fcc	fcc
Valence electrons	$3d^5 4s^1$	$5d^4 6s^2$	$4d^5 5s^1$	$3d^8 4s^2$	$5d^9 6s^1$	$3s^2 3p^1$	$5d^{10} 6s^1$	$3d^{10} 4s^1$	$4d^{10} 5s^1$
Cutoff energy (eV)	1400	1400	1400	1600	1000	600	1200	1200	1200
Number of k-points	12^3	12^3	12^3	20^3	20^3	12^3	12^3	12^3	12^3

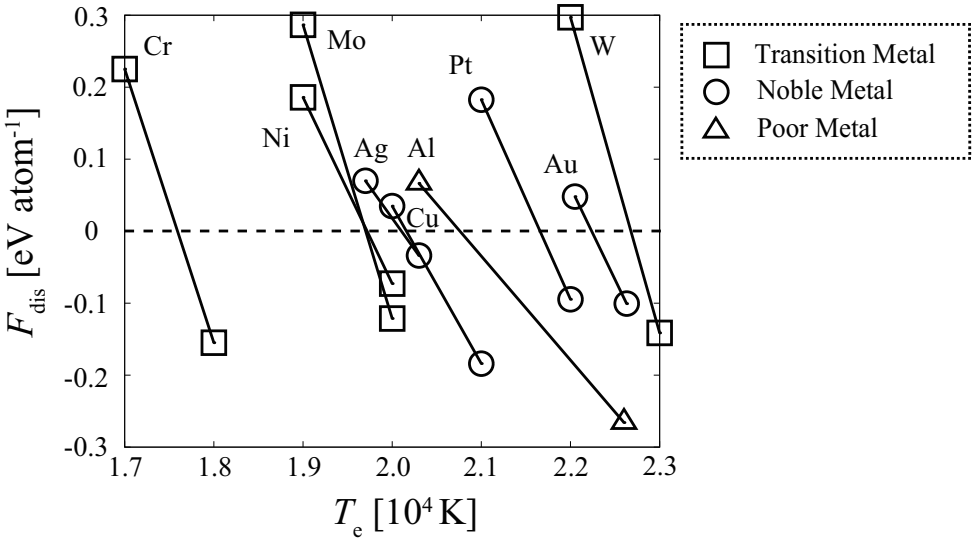

Figure 5.1: Calculation results of $F_{\rm dis}(T_e)$ and the linear interpolation of them. Square, circle, and triangle marks represent calculation results of $F_{\rm dis}(T_e)$ of the transition metals, the noble metals, and the poor metal, respectively. From the definition of $F_{\rm dis}(T_e^{\rm thr}) = 0$, x values of nodes between the interpolation lines and the dotted line ($y = 0$) represent $T_e^{\rm thr}$ of each material.

Table 5.4: Calculation results of $T_e^{\rm thr}$ and classification of metals.

	Cr	W	Mo	Ni	Pt	Al	Ag	Cu	Au
$T_e^{\rm thr}$ (10^4 K)	1.76	2.27	1.97	1.97	2.16	2.08	2.01	2.02	2.23
Classification	Trans.	Trans.	Trans.	Trans.	Noble	Poor	Noble	Noble	Noble

Trans.: Transition metal, Noble: Noble metal, Poor: Poor metal

5.2.2 Ablation threshold fluence: $J_{\mathbf{thr}}$

Using Eq. (5.4), the parameters in the Table 5.1, and T_e^{thr} in Table 5.4, we can calculate J_{thr} of the several metals (Cr, W, Mo, Ni, Pt, Al, Ag, Cu, and Au). Calculation results of J_{thr} are shown in Fig. 5.2, in which labels of x axis are listed in the ascending order of the reflectivity of the metals. Boxes and bars represent calculation results and experimental results [59, 127, 128, 131–134] with errors, respectively. All experimental data are "single pulse" ablation threshold because the ablation threshold fluence changes during many pulse irradiation [48, 51, 59, 131–133, 135, 136]. This phenomenon is called an incubation effect. It has been found that the incubation effect is attributed to the surface modification due to laser irradiation. To avoid considering the incubation effect, we compare our calculation results with experimental results of the single pulse ablation.

Figure 5.2 shows that our calculation results reproduce experimental results of the low reflectivity materials (in the left side of Fig. 5.2: Cr, W, Mo, Ni, and Pt). On the other hand, there are large disagreements in large reflectivity materials (Cu and Au). We considered that the reason is coming from the sensitivity of J_{thr} to R. A previous experiment for Cu [100] showed that R of little above ablation threshold fluence is 0.86, which is 11 % smaller than that of low laser fluence. However, in our simulation, R is assumed to be independent from J in our calculation. Therefore, we speculate that the disagreement of J_{thr} with respect to the high reflectivity materials (Cu and Au) is coming from the T_e-dependence of R.

5.3 Summary

In this chapter, we developed a simple calculation model to calculate the ablation threshold fluence J_{thr}. This calculation model was constructed based on the results of the CM and the TTM-MD simulations. To calculate J_{thr} based on the developed model, we estimated the ablation threshold electronic temperature T_e^{thr}. On the basis of the calculation results, we considered that T_e^{thr} is strongly dependent on not only the DOS, but also on other properties, such as the cohesive energy. Moreover, our calculation results of J_{thr} showed that the developed model can reproduce experimental results of the low reflectivity materials (Cr, W, Mo, Ni, and Pt). On the other hand, there are large disagreements in the large reflectivity materials (Cu and Au). We considered that these discrepancies of the high reflectivity materials (Cu, and Au) are coming from T_e-dependence of R.

Here, we showed the versatility of the EED mechanism and discussed the dominant factors that determine J_{thr}.

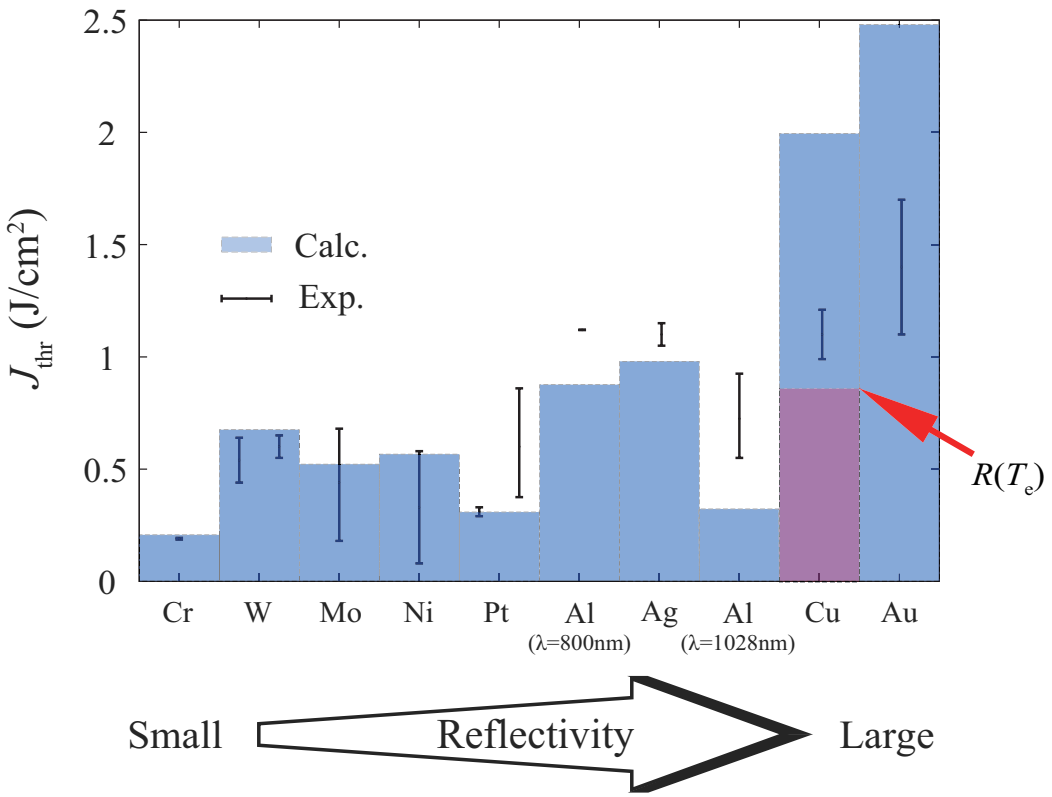

Figure 5.2: Calculation results of the material dependence of J_{thr}. Labels of x axis are listed in the ascending order of the reflectivity. Boxes represent results based on the calculation model. Bars represent experimental results [59, 127, 128, 131–134] with error. Red box represents a results using $R(T_e)$ that is a reflectivity of a Cu film irradiated with a laser whose fluence is little above ablation threshold [100].

6. Concluding Remarks

6.1 Summary of this thesis

In this thesis, we investigated the physical mechanism of metal ablation caused by irradiation with an ultrashort pulse laser. Aims of our study are following two. The first one is elucidating the physical mechanism of the non-thermal ablation of metals. The other is developing calculation methods to simulate the ultrashort laser-irradiated metals.

Throughout our study, we used the well-known two-temperature model (TTM) to describe metals irradiated with an ultrashort laser pulse. Our finite-temperature density functional theory (FTDFT) calculations showed that the electronic entropy effect leads to the instability of condensed copper (Cu) at high electronic temperature (T_e). Based on the result, we proposed the electronic entropy-driven (EED) mechanism to describe the non-thermal ablation of metals. Subsequently, to investigate the physical mechanism of the non-thermal ablation and the validity of the EED mechanism, we extended calculation models and developed codes of the continuum model (CM) simulation and the TTM molecular dynamics (TTM-MD) simulation. As a result of calculations, we found that the origin of the driving force of the high energy atom emission is attributed to the electronic entropy effect. This finding bridges the discrepancy between experiments and previous theoretical simulations. In addition, we constructed a simple calculation model for estimating the ablation threshold fluence based on our CM and TTM-MD simulation results, and applied the method to several materials (Cr, W, Mo, Ni, Pt, Al, Ag, Cu, and Au). Consequently, we showed that the versatility of the EED mechanism.

In Chap. 2, our FTDFT calculations showed that Cu becomes instable at high T_e ($\sim 25000\,\mathrm{K}$) due to the contribution of the electronic entropy term $-ST_e$. Based on the electronic density of state (DOS) and the band calculations, we considered that the high DOS at large volume brings about the large benefit of the electronic entropy, and it leads the instability. On the basis of this consideration, we proposed the electronic entropy-driven (EED) mechanism to describe the physical mechanism of the non-thermal ablation of metals. One advantage of this mechanism is that it does not require the neutrality breakdown by electron emission, which is denied by the experimental result in the case of metal ablation. Moreover, the EED mechanism is expected to be applied not only for ablation of Cu but also for all metals, furthermore for some narrow gap semiconductors.

In Chap. 3, we developed a calculation model in the continuum scheme to include the electronic entropy effect, and calculated the ablation depth using it. In the calculation model, we assumed

that, to cause ablation, the kinetic energy of atoms need to overcome the activation barrier for dissociation, which is decreased at high T_e due to the electronic entropy effect. Our calculation results showed that our developed model agrees with experimental results in the low-laser-fluence region, where the contribution of the non-thermal ablation has been known to be large. Moreover, we found that the effect of the electronic entropy has dominant effect in the region. These results supported the EED mechanism and our suggestion that the electronic entropy effect is dominant for the non-thermal ablation of metals.

In Chap. 4, we carried out large-scale atomistic simulations with the hybrid calculation model, in which the CM and the classical MD methods are combined. This calculation model is called TTM-MD model. We extended the TTM-MD simulation model to satisfy the law of conservation of energy. To express the change of the electronic states in the laser-excited solids, we developed a function form of the T_e-dependent interatomic potential (IAP) and made the IAP. From the comparison with the FTDFT simulations, we found that the calculation results using the IAP are well consistent with results of FTDFT simulations. After we certify that our simulations satisfy the law of conservation of energy, we carried out simulations of the ablation. These calculation results showed that atoms are emitted near the ablation threshold fluence. This result bridges the discrepancy between experiments and previous theoretical simulations. Also, we found that the electronic entropy effect is essential not only for the atom emission but also for the spallation process and the phase explosion process. Moreover, we compared the TTM-MD calculation results of ablation depth with the CM calculation results and the experimental data. As a result, our TTM-MD simulations are well consistent with these results, quantitatively. In addition, we found that our calculation results can qualitatively reproduce experimental results, such as the large change of the ablation depth near the ablation threshold [46] and the pulse-width dependence of the ablation threshold [125].

In Chap. 5, we developed a simple calculation model to estimate the ablation threshold fluence. This calculation model were constructed based on the results of the CM simulation (Chap. 3) and the TTM-MD simulation (Chap. 4). From the calculation of the ablation threshold electronic temperature, we found that the cohesive energy and the DOS near the chemical surface play an important role in determining the ablation threshold fluence. Our calculation results reproduced experimental results of the low reflectivity materials (Cr, W, Mo, Ni, and Pt). On the other hand, there are large disagreements in the large reflectivity materials (Cu and Au). We considered that this discrepancy comes from T_e-dependence of R. Our calculation results here suggested the versatility of the EED mechanism.

Through this thesis, using extended mathematical models and developed codes, we elucidated that the electronic entropy effect plays an important role in the non-thermal ablation of metals.

6.2 Future issues

Here, we mention future view of our study.

The origin of the driving force causing the non-thermal ablation of metals is one of the most attractive questions in the laser processing field. One of the reason is that the understanding of the non-thermal ablation is equivalent to that of the precision processing. We expect that our findings will greatly affect the industrial field and promote further understanding of the physical mechanism of the non-thermal ablation. For example, we think that our findings contribute to the development of a laser processing simulator. At present, optimization conditions for laser processing have been estimated by experiments, so that highly efficient and cost are wasted. This simulator would enable us to predict the optimization conditions without making experiment. Moreover, the condition of the higher precision processing would be predicted from the simulator. In other words, the simulation results would indicate the direction of the laser light source development. We believe that it will lead to the atomic scale laser processing, of which a potential is shown in our TTM-MD simulation (Chap. 4).

However, there are many problem to realize this simulator. Our TTM-MD simulation scheme is too complex to be used in the industrial field. Although more simple schemes are needed, such as the CM (Chap. 3), it is obvious that the more detail understanding is necessary to construct them. In other words, understanding of the non-thermal ablation has been lacking yet. Therefore, further analyses and extended calculation schemes are necessary.

Although we show the importance of the electronic entropy effect, detail analysis has not been carried out. In this thesis, we insist that, as the applied laser fluence increases, the physical mechanisms of the non-thermal ablation changes from the atom emission, to the spallation mechanism and to the phase explosion. However, the reason of these changes have not been analyzed, quantitatively. We will investigate the T_e, T_l, and pressure dependence of the stability of solids.

It is also important to investigate the accuracy of our TTM-MD simulation by comparing the experimental results, quantitatively. We would like to investigate whether our simulation model can reproduce the experimental results, such as the velocity distribution of the emitted atoms.

Expression of the laser-matter interaction is one of the most difficult problems. In our simulation, we carried out simulation with the reflectivity of the experiment, which should depend on the laser fluence and the wavelength. Therefore, to carry out the simulation for different wavelength, we must to obtain the value of the reflectivity by making experiment. We would like to combine our TTM-MD simulation with time-dependent DFT (TDDFT [137, 138]) to broaden the application range of our simulation.

Although we investigated the laser ablation of metals in this study, our study would be also related to the ablation of semiconductors. In the case of the semiconductor such as GeTe, whose band gap is $\sim 0.6\,\mathrm{eV}$, the condensed state becomes instable at high T_e due to the electronic entropy effect in the same way as metals. The electronic entropy effect of semiconductors would be smaller than that of metals because electronic states do not exist near the electronic chemical potential in semiconductors. We expect that the electronic entropy effect makes a contribution to the ablation of semiconductors, but it would compete with the coulomb explosion

mechanism. We think that it is worth while investigating the competition between the coulomb explosion process and the EED mechanism for further understanding of the non-thermal ablation of semiconductors.

Besides, we are sure that our finding and developed code are associated with not only the ablation issues but also other ultrafast phenomena as followings:

- Ultrafast phase transition (the bcc-fcc transition of W [79], the ultrafast non-melting crystalline to amorphous transition of $Ge_2Sb_2Te_5$ [55])
- Ultrafast melting of Au [4]
- Warm dense matter or initial process of plasma generation.
- Formation of laser induced periodic surface structure (LIPSS) [56, 57].

A previous study [79] showed that structural stability between the body-centered cubic (bcc) structure and face-centered cubic (fcc) structure of W changes at high T_e. However, their MD simulation suggested that the bcc-fcc transition can not be realized in W since solid is melted before structure change is accomplished. On the other hands, we expect that this conclusion might change by our extended TTM-MD calculation method because the electronic entropy effect absorbs the energy that becomes the kinetic energy of atoms in the previous simulation model. We expect that our simulation becomes a trigger of reconsidering previous studies.

We are sure that our findings include fundamentally important knowledge not only for the ablation issue but also for the other related fields. In addition, our extended calculation models and developed codes will continue to promote the further understanding of the ablation process and provide new and essential insight into these fields.

APPENDIX A Parameter Dependence of Calculation Rsults

To analyze the G dependence of the ablation depth, we calculated the ablation depth using $G(T_e)$ of Lin *et al*. [89], which are used in many previous TTM simulations. Fig. A.1 represents the calculation results, and blue and green lines represent calculation results using G of Migdal *et al*. [97] and using $G(T_e)$ of Lin *et al*., respectively. This figure shows that G dependence is not small in the high-laser-fluence region but our considerations in Sec. 3.4 do not change even $G(T_e)$ of Lin *et al*.

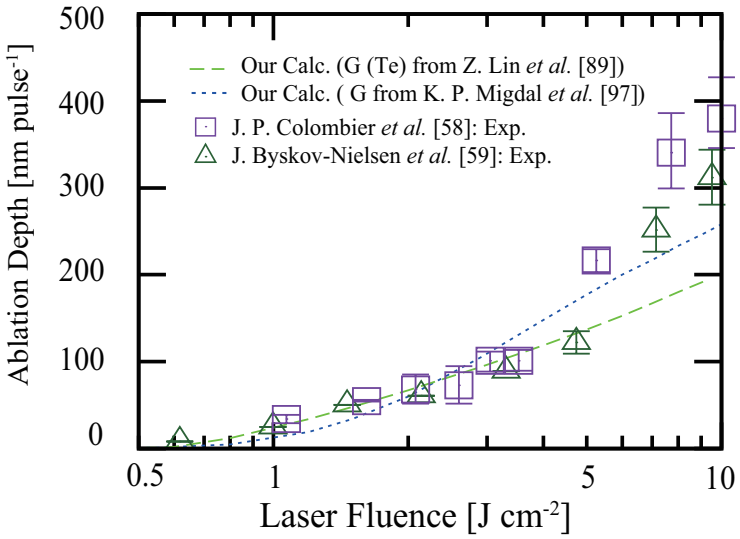

Figure A.1: G dependence of the ablation depth. Blue and green lines represent calculation results using G of Migdal *et al*. and $G(T_e)$ of Lin *et al*. [89], respectively.

APPENDIX B Pulse Number Dependence of the Reflectivity

Here, a method of the determination of the local reflectivities $R_n^{\mathrm{L}}(J)$ as a function of laser fluence J is explained. In a previous experiment [100], total reflectivity $R_n^{\mathrm{T}}(J_0)$ was observed by irradiation with a laser whose peak fluence is J_0. $R_n^{\mathrm{T}}(J_0)$ is calculated with $R_n^{\mathrm{L}}(J)$ and the space distribution of the laser fluence $J(r)$:

$$R_n^{\mathrm{T}}(J_0) = \frac{\int_0^{2\pi}\int_0^{\infty} J(r) R_n^{\mathrm{L}}(J(r)) r d\theta dr}{\int_0^{2\pi}\int_0^{\infty} J(r) r d\theta dr} \tag{s1}$$

Here r is the distance from the center of the laser spot. To obtain $R_n^{\mathrm{L}}(J)$ from $R_n^{\mathrm{T}}(J_0)$, we make assumptions that the space distribution of laser fluence is the Gaussian distribution and $R_n^{\mathrm{L}}(J)$ can be described as:

$$R_n^{\mathrm{L}}(J) = a_n \ln J + b_n, \tag{s2}$$

where a_n and b_n are constant parameters. The latter assumption is justified around or somewhat above ablation threshold by a previous model calculation [103]. From Eqs. (s1) and (s2),

$$R_n^{\mathrm{T}}(J_0) = a_n \ln J_0 + a_n \left(\frac{1}{2} \ln \frac{\beta}{\pi} - 1 \right) + b_n \tag{s3}$$

can be derived. By fitting the experimental [100] reflectivities $R_n^{\mathrm{T}}(J_0)$ with Eq. (s3), a_n and b_n are obtained. As a result, $R_n^{\mathrm{L}}(J_0)$ is determined, of which the root mean square errors were less than 0.02. These values are summarized on Table B.1. Besides, Fig. B.1 represents fitting experimental data [100] and obtained $R_n^{\mathrm{T}}(J)$ and $R_n^{\mathrm{L}}(J)$. In our simulations, these a_n and b_n were used to simulate the ablation depth.

Table B.1: Values of a_n and b_n.

n	10	50	100
a_n	−0.107139	−0.0836277	−0.0851366
b_n	0.760746	0.675221	0.633524

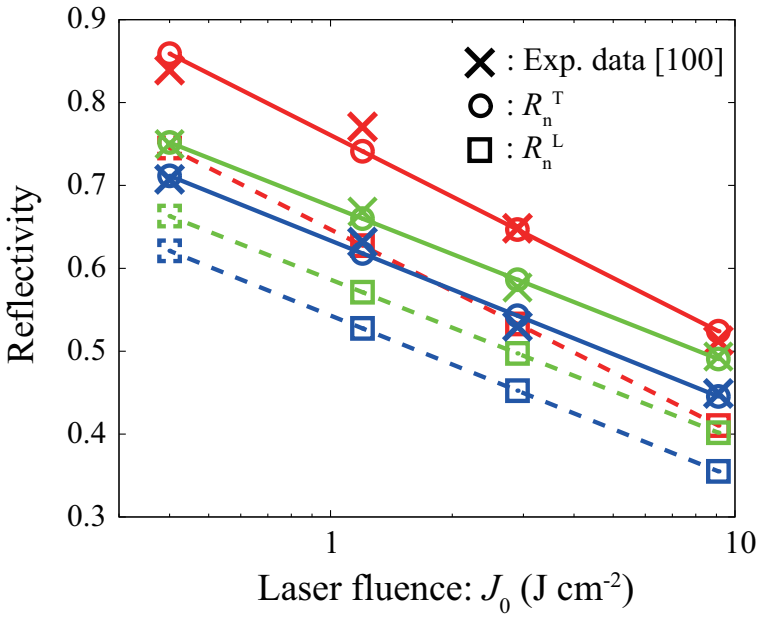

Figure B.1: Values of J dependent reflectivity. Cross, circle, and square marks represent the experimental data [100], $R_n^{\mathrm{T}}(J)$, and $R_n^{\mathrm{L}}(J)$, respectively. $R_n^{\mathrm{T}}(J)$ are fitted by the linear function to the experimental data.

BIBLIOGRAPHY

[1] J. Kanasaki, E. Inami, K. Tanimura, H. Ohnishi, and K. Nasu, Phys. Rev. Lett. **102**, 087402 (2009).

[2] H. Ohnishi and K. Nasu, Phys. Rev. B **79**, 054111 (2009).

[3] D. M. Fritz, D. A. Reis, B. Adams, R. A. Akre, J. Arthur, C. Blome, P. H. Bucksbaum, A. L. Cavalieri, S. Engemann, S. Fahy, R. W. Falcone, P. H. Fuoss, K. J. Gaffney, M. J. George, J. Hajdu, M. P. Hertlein, P. B. Hillyard, M. Horn-von Hoegen, M. Kammler, J. Kaspar, R. Kienberger, P. Krejcik, S. H. Lee, A. M. Lindenberg, B. McFarland, D. Meyer, T. Montagne, É. D. Murray, A. J. Nelson, M. Nicoul, R. Pahl, J. Rudati, H. Schlarb, D. P. Siddons, K. Sokolowski-Tinten, T. Tschentscher, D. von der Linde, and J. B. Hastings, Science **315**, 633 (2007).

[4] S. L. Daraszewicz, Y. Giret, N. Naruse, Y. Murooka, J. Yang, D. M. Duffy, A. L. Shluger, and K. Tanimura, Phys. Rev. B **88**, 184101 (2013).

[5] M. Hase, Y. Miyamoto, and J. Tominaga, Phys. Rev. B **79**, 174112 (2009).

[6] Y. Miyasaka, M. Hashida, Y. Ikuta, K. Otani, S. Tokita, and S. Sakabe, Phys. Rev. B **86**, 075431 (2012).

[7] M. Hashida, S. Namba, K. Okamuro, S. Tokita, and S. Sakabe, Phys. Rev. B **81**, 115442 (2010).

[8] H. Dachraoui and W. Husinsky, Appl. Phys. Lett. **89**, 104102 (2006).

[9] H. Dachraoui, W. Husinsky, and G. Betz, Appl. Phys. A **83**, 333 (2006).

[10] S. I. Anisimov, B. L. Kapeliovich, and T. L. Perel'man, Sov. Phys. -JETP **39**, 375 (1974).

[11] B. Y. Mueller and B. Rethfeld, Phys. Rev. B **87**, 035139 (2013).

[12] A. M. Brown, R. Sundararaman, P. Narang, W. A. Goddard, and H. A. Atwater, ACS Nano **10**, 957 (2016).

[13] R. W. Schoenlein, W. Z. Lin, J. G. Fujimoto, and G. L. Eesley, Phys. Rev. Lett. **58**, 1680 (1987).

[14] H. E. Elsayed-Ali, T. B. Norris, M. A. Pessot, and G. A. Mourou, Phys. Rev. Lett. **58**, 1212 (1987).

[15] H. E. Elsayed-Ali, T. Juhasz, G. O. Smith, and W. E. Bron, Phys. Rev. B **43**, 4488 (1991).

[16] J. Hohlfeld, S.-S. Wellershoff, J. Güdde, U. Conrad, V. Jähnke, and E. Matthias, Chem. Phys. **251**, 237 (2000).

[17] R. Ernstorfer, M. Harb, C. T. Hebeisen, G. Sciaini, T. Dartigalongue, and R. J. Dwayne Miller, Science **323**, 1033 (2009).

[18] Y. Giret, A. Gellé, and B. Arnaud, Phys. Rev. Lett. **106**, 155503 (2011).

[19] G. E. Norman, S. V. Starikov, and V. V. Stegailov, J. Exp. Theor. Phys. **114**, 792 (2012).

[20] G. E. Norman, S. V. Starikov, V. V. Stegailov, I. Saitov, and P. A. Zhilyaev, Contrib. Plasma Phys. **53**, 129 (2013).

[21] V. Recoules, J. Clérouin, G. Zérah, P. M. Anglade, and S. Mazevet, Phys. Rev. Lett. **96**, 055503 (2006).

[22] N. A. Inogamov, Y. V. Petrov, V. V. Zhakhovsky, V. A. Khokhlov, B. J. Demaske, S. I. Ashitkov, K. Khishchenko, K. P. Migdal, M. B. Agranat, S. I. Anisimov, V. E. Fortov, and I. I. Oleynik, AIP Conf. Proc. **1464**, 593 (2012).

[23] X. Wang, A. A. Kuchmizhak, X. Li, S. Juodkazis, O. B. Vitrik, Y. N. Kulchin, V. V. Zhakhovsky, P. A. Danilov, A. A. Ionin, S. I. Kudryashov, A. A. Rudenko, and N. A. Inogamov, Phys. Rev. Appl. **8**, 044016 (2017).

[24] N. Watanabe, N. Takahashi, and K. Tsushima, Mater, Chem. Phys. **54**, 173 (1998).

[25] T. Yoshitake, T. Nagamoto, and K. Nagayama, Mater, Sci. Eng. B **72**, 124 (2000).

[26] A. Fojtik and A. Henglein, Phys. Chem. **97**, 252 (1993).

[27] J. Neddersen, G. Chumanov, and T. M. Cotton, Appl. Spectrosc. **47**, 1959 (1993).

[28] C. Wu and L. Zhigilei, Appl. Phys. A **114**, 11 (2013).

[29] P. Ji and Y. Zhang, Appl. Phys. A **123**, 671 (2017).

[30] A. A. Foumani and A. R. Niknam, J. Appl. Phys. **123**, 043106 (2018).

[31] C. Schüler, H. M. Urbaseek, and L. Zhigilei, Phys. Rev. B **66**, 115404 (2002).

[32] D. S. Ivanov and L. V. Zhigilei, Phys. Rev. B **68**, 064114 (2003).

[33] C. M. Rouleau, C.-Y. Shih, C. Wu, L. V. Zhigilei, A. A. Puretzky, and D. B. Geohegan, Appl. Phys. Lett. **104**, 193106 (2014).

[34] D. von der Linde, K. Sokolowski-Tinten, and J. Bialkowski, Appl. Surf. Sci. **109-110**, 1 (1997).

[35] K. Sokolowski-Tinten, J. Bialkowski, A. Cavalleri, M. Boring, H. Schüler, and D. von der Linde, Proc. SPIE **3343**, 46 (1998).

[36] A. C. K. Sokolowski-Tinten, J. Bialkowski and D. von der Linde, Phys. Rev. Lett. **81**, 224 (1998).

[37] K. Sokolowski-Tinten and D. von der Linde, Appl. Surf. Sci. **154-155**, 1 (2000).

[38] A. Miotello and R. Kelly, Appl. Phys. A **69**, S67 (1999).

[39] N. Bulgakova and A. Bulgakov, Appl. Phys. A **73**, 199 (2001).

[40] E. Leveugle, L. V. Zhigilei, A. Sellinger, and J. M. Fitz-Gerald, Appl. Surf. Sci. **253**, 6456 (2007).

[41] M. D. Perry, B. C. Stuart, P. S. Banks, M. D. Feit, V. Yanovsky, and A. M. Rubenchik, J. Appl. Phys. **85**, 6803 (1999).

[42] M. Shaheen, J. Gagnon, and B. Fryer, J. Appl. Phys. **114**, 083110 (2013).

[43] S. Nolte, C. Momma, H. Jacobs, A. Tünnermann, B. N. Chichkov, B. Welleegehausen, and H. Welling, J. Opt. Soc. Am. B **14**, 2716 (1997).

[44] B. N. Chichkov, C. Momma, S. Nolte, F. von Alvensleben, and A. Tünnermann, Appl. Phys. A **63**, 109 (1996).

[45] C. Momma, B. N. Chichkov, S. Nolte, F. von Alvensleben, A. Tünnermann, H. Welling, and B. Wellegehausen, Opt. Commun. **129**, 134 (1996).

[46] M. Hashida, A. Semerok, O. Gobert, G. Petite, and J. F. Qgner, Proc. SPIE **4423**, 178 (1999).

[47] X. Zhao and Y. C. Shin, J. Phys. D: Appl. Phys. **46**, 335501 (2013).

[48] R. Stoian, D. Ashkenasi, A. Rosenfeld, M. Wittmann, R. Kelly, and E. E. B. Campbell, Nucl. Instrum. Methods Phys. Res. B **166**, 682 (2000).

[49] R. Stoian, D. Ashkenasi, A. Rosenfeld, and E. E. B. Campbell, Phys. Rev. B **62**, 13167 (2000).

[50] T. Sato, T. Okino, K. Yamanouchi, A. Yagishita, F. Kannari, K. Yamakawa, K. Midorikawa, H. Nakano, M. Yabashi, M. Nagasono, and T. Ishikawa, Appl. Phys. Lett. **92**, 154103 (2008).

[51] J. Li, X. Wang, Z. Chen, J. Zhou, S. S. Mao, and J. Cao, Appl. Phys. Lett. **98**, 011501 (2011).

[52] N. Bulgakova, R. Stoian, A. Rosenfeld, I. Hertel, W. Marine, and E. Campbell, J. Appl. Phys. **81**, 345 (2005).

[53] V. Stegailov and P. Zhilyaev, Contrib. Plasma Phys. **55**, 164 (2015).

[54] V. Stegailov and P. Zhilyaev, Mol. Phys. **114**, 509 (2016).

[55] P. Fons, H. Osawa, A. V. Kolobov, T. Fukaya, M. Suzuki, T. Uruga, N. Kawamura, H. Tanida, and J. Tominaga, Phys. Rev. B **82**, 041203(R) (2010).

[56] M. Birnbaum, J. Appl. Phys. **36**, 3688 (1965).

[57] D. Bäuerle, *Electronic structure of Materials* (Springer, Berlin, 2000), 3rd ed.

[58] J. P. Colombier, P. Combis, F. Bonneau, R. Le Harzic, and E. Audouard, Phys. Rev. B **71**, 165406 (2005).

[59] J. Byskov-Nielsen, J. M. Savolainen, M. S. Christensen, and P. Balling, Appl. Phys. A **101**, 97 (2010).

[60] D. N. Mermin, Phys. Rev. **137**, A1441 (1965).

[61] P. Hohenberg and W. Kohn, Phys. Rev. **136**, B864 (1964).

[62] W. Kohn and L. J. Sham, Phys. Rev. A **140**, 1133 (1965).

[63] J. P. Perdew, K. Burke, and M. Ernzerhof, Phys. Rev. Lett. **77**, 3865 (1996).

[64] J. P. Perdew, K. Burke, and M. Ernzerhof, Phys. Rev. Lett. **78**, 1396 (1997).

[65] J. P. Perdew, A. Ruzsinszky, G. I. Csonka, O. A. Vydrov, G. E. Scuseria, L. Constantin, X. Zhou, and K. Burke, Phys. Rev. Lett. **100**, 136406 (2008).

[66] J. P. Perdew, A. Ruzsinszky, G. I. Csonka, O. A. Vydrov, G. E. Scuseria, L. Constantin, X. Zhou, and K. Burke, Phys. Rev. Lett. **102**, 039902 (2009).

[67] R. G. Dandrea and N. W. Ashcroft, Phys. Rev. B **34**, 2097 (1986).

[68] S. Pittalis, C. R. Proetto, A. Floris, A. Sanna, C. Bersier, K. Burke, and E. K. U. Gross, Phys. Rev. Lett. **107**, 163001 (2011).

[69] H. Eschrig, Phys. Rev. B **82**, 205120 (2010).

[70] T. Sjostrom and J. Daligault, Phys. Rev. B **90**, 155109 (2014).

[71] V. V. Karasiev, T. Sjostrom, J. Dufty, and S. B. Trickey, Phys. Rev. Lett. **112**, 076403 (2014).

[72] V. V. Karasiev, L. Calderín, and S. B. Trickey, Phys. Rev. E **93**, 063207 (2016).

[73] T. Dornheim, S. Groth, T. Sjostrom, F. D. Malone, W. M. C. Foulkes, and M. Bonitz, Phys. Rev. Lett. **117**, 156403 (2016).

[74] K. Burke, J. C. Smith, P. E. Grabowski, and A. Pribram-Jones, Phys. Rev. B **93**, 195132 (2016).

[75] J. P. Perdew and A. Zunger, Phys. Rev. B **23**, 5048 (1981).

[76] W. B. Pearson, *A Handbook of Lattice Spacings and Structures of Metals and Alloys* (Pergamon, Oxford, 1958).

[77] Y. Tanaka and S. Tsuneyuki, Appl. Phys. Exp. **11**, 046701 (2018).

[78] "xtapp," http://ma.cms-initiative.jp/en/application-list/xtapp.

[79] S. T. Murphy, S. L. Daraszewicz, Y. Giret, M. Watkins, A. L. Shluger, K. Tanimura, and D. M. Duffy, Phys. Rev. B **92**, 134110 (2015).

[80] S. Murphy, Y. Giret, S. Daraszewicz, A. Lim, A. Shluger, K. Tanimura, and D. Duffy, Phys. Rev. B **93**, 104105 (2016).

[81] S. Khakshouri, D. Alfè, and D. M. Duffy, Phys. Rev. B **78**, 224304 (2008).

[82] H. Zhang, C. Li, E. Bevillon, G. Cheng, J. P. Colombier, and R. Stoian, Phys. Rev. B **94**, 224103 (2016).

[83] D. K. Il'nitsky, V. A. Khokhlov, V. V. Zhakhovsky, Y. V. Petrov, K. P. Migdal, and N. A. Inogamov, J. Phys. Conf. Ser. **774**, 012101 (2016).

[84] R. Stoian, A. Rosenfeld, D. Ashkenasi, I. Hertel, N. Bulgakova, and E. Campbell, Phys. Rev. Lett. **88**, 097603 (2002).

[85] P. B. Johnson and R. W. Christy, Phys. Rev. B **6**, 4370 (1972).

[86] N. W. Ashcroft and N. D. Mermin, *Solid State Physics* (Saunders College, Philadelphia, 2011).

[87] T. F. Chan, SIAM J. Numer. Anal. **21**, 272 (1984).

[88] E. Bévillon, J. P. Colombier, V. Recoules, and R. Stoian, Appl. Surf. Sci. **336**, 79 (2015).

[89] Z. Lin, L. V. Zhigilei, and V. Celli, Phys. Rev. B **77**, 075133 (2008).

[90] M. E. Straumanis and L. S. Yu, Acta Crystallogr. A **25**, 676 (1969).

[91] D. A. Papaconstantopoulos, L. L. Boyer, B. M. Klein, A. R. Williams, V. L. Morruzzi, and J. F. Janak, Phys. Rev. B **15**, 4221 (1977).

[92] X. Y. Wang, D. M. Riffe, Y.-S. Lee, and M. C. Downer, Phys. Rev. B **50**, 8016 (1994).

[93] M. Kaveh and N. Wiser, Adv. Phys. **33**, 257 (1984).

[94] M. J. Laubitz, Can. J. Phys. **45**, 3677 (1967).

[95] A. M. Brown, R. Sundararaman, P. Narang, W. A. Goddard, and H. A. Atwater, Phys. Rev. B **94**, 075120 (2016).

[96] P. B. Allen, Phys. Rev. B **59**, 1460 (1987).

[97] K. P. Migdal, Y. V. Petrov, D. K. Il'nitsky, V. V. Zhakhovsky, N. A. Inogamov, K. V. Khishchenko, D. V. Knyazev, and P. R. Levashov, Appl. Phys. A **122**, 408 (2016).

[98] Y. Petrov, N. Inogamov, and K. Migdal, JETP. Lett. **97**, 20 (2013).

[99] K. P. Migdal, V. V. Il'nitsky, Y. V. Petrov, and K. V. Inogamov, J. Phys. Conf. Ser. **653**, 012086 (2015).

[100] A. Y. Vorobyev and C. Guo, J. Appl. Phys. **110**, 043102 (2011).

[101] P. G. Etchegoin, E. C. Le Ru, and M. Meyer, J. Chem. Phys. **125**, 164705 (2006).

[102] P. G. Etchegoin, E. C. Le Ru, and M. Meyer, J. Chem. Phys. **127**, 189901 (2007).

[103] Y. P. Ren, J. K. Chen, and Y. W. Zhang, J. Appl. Phys. **110**, 113102 (2011).

[104] C. Kittle, *Introduction to Solid State Physics* (John Wiley and Sons, New York, 2004), 8th ed.

[105] D. R. Linde, *CRC Handbook of Chemistry and Physics* (SCRC Press, Florida, 2003-2004), 84th ed.

[106] W. G. Hoover, Phys. Rev. A **31**, 1695 (1985).

[107] M. S. Daw and M. I. Baskes, Phys. Rev. Lett. **25**, 45 (1985).

[108] M. W. Finnis and J. E. Sinclair, Phil. Mag. A **50**, 45 (1984).

[109] A. P. Sutton, *Electronic Structure of Materials* (Clarendon Press, New York, 1993).

[110] X. D. Dai, Y. Kong, J. H. Li, and B. X. Liu, J. Phys.: Condens. Matter **18**, 4527 (2006).

[111] S. S. Harial, N. Farid, A. Hassanein, and V. M. Kozhevin, J. Appl. Phys **114**, 203302 (2013).

[112] G. Kresse and J. Furthmüller, Comp. Mat. Sci. **6**, 15 (1996).

[113] G. Kresse and J. Furthmüller, Phys. Rev. B **54**, 11169 (1996).

[114] G. Kresse and J. Hafner, Phys. Rev. B **47**, 558 (1993).

[115] P. E. Blöchl, Phys. Rev. B **50**, 17953 (1994).

[116] G. Kresse and D. Joubert, Phys. Rev. B **59**, 1758 (1999).

[117] E. Kaxiras, *Atomic and Electronic Structure of Solids* (Cambridge University Press, Cambridge, 2003).

[118] W. Humphrey, A. Dalke, and K. Schulten, J. Mol. Graph. Model **14**, 33 (1996).

[119] J. P. Poirier, *Introduction to the Physics of the Earth's Interior* (Cambridge University Press, New York, 2000), 2nd ed.

[120] T. Tadano, "Alamode," http://sourceforge.net/projects/alamode.

[121] T. Tadano, Y. Gohda, and S. Tsuneyuki, J. Phys.: Condens. Matter **26**, 225402 (2014).

[122] G. Simmons and H. Wang, *Single Crystal Elastic Constants and Calculated Aggregate Properties: A Handbook* (M. I. T. Press, Cambridge, 1971), 2nd ed.

[123] A. Stukowski, Model. Simul. Mater. Sci. Eng. **18**, 015012 (2010).

[124] Z. S. Basinski, M. S. Duesbery, and R. Taylor, Can. J. Phys. **49**, 2160 (1971).

[125] M. Hashida, A. Semerok, O. Gobert, G. Petite, Y. Izawa, and J. F. Qgner, Appl. Surf. Sci. **197**, 862 (2002).

[126] E. Bévillon, J. P. Colombier, V. Recoules, and R. Stoian, Phys. Rev. B **89**, 115117 (2014).

[127] M. Olbrich, E. Punzel, P. Lickschat, S. Weißmantel, and A. Horn, Phys. Procedia **83**, 93 (2016).

[128] T. M. Saghebfar, M. K. Tehrani, S. M. R. Darbani, and A. E. Majd, Appl. Phys. A **123**, 28 (2017).

[129] A. Y. Vorobyev, V. S. Makin, and C. Guo, Phys. Rev. Lett. **102**, 234301 (2009).

[130] M. N. Polyanskiy, "Refractive index database," https://refractiveindex.info.

[131] S. E. Kirkwood, A. C. van Porta, Y. Y. Tsui, and R. Fedosejevs, Appl. Phys. A **81**, 729 (2005).

[132] L. Urech, T. Lippert, A. Wokam, S. Martin, H. Mädebach, and J. Krüger, Appl. Surf. Sci. **252**, 4754 (2006).

[133] L. Gallais, E. Bergeret, B. Wang, M. Guerin, and E. Bènevent, Appl. Phys. A **115**, 177 (2017).

[134] Q. Li, H. Lao, J. Lin, Y. Chen, and X. Chen, Appl. Phys. A **105**, 125 (2011).

[135] A. Sun, M. Lenzner, and W. Rudolph, J. Appl. Phys. **117**, 073102 (2015).

[136] Y. Jee, M. F. Becker, and R. M. Walser, J. Opt. Soc. Am. B **5**, 648 (1998).

[137] E. Runge and E. K. U. Gross, Phys. Rev. Lett. **52**, 997 (1984).

[138] S. Yamada, M. Noda, K. Nobusada, and K. Yabana, Phys. Rev. B **98**, 245147 (2018).